The Dissertation Committee for Minglei Xiao
certifies that this is the approved version of the following dissertation:

Topics in Higgs Phenomenology and Holographic Complexity

Committee:

Willy Fischler, Supervisor

Jacques Distler

Vadim Kaplunovsky

Can Kilic

Paul Shapiro

Topics in Higgs Phenomenology and Holographic Complexity

by

Minglei Xiao

DISSERTATION

Presented to the Faculty of the Graduate School of

The University of Texas at Austin

in Partial Fulfillment

of the Requirements

for the Degree of

DOCTOR OF PHILOSOPHY

THE UNIVERSITY OF TEXAS AT AUSTIN

May 2018

Dedicated to my grandmother

Acknowledgments

First, I want to express my regret for not being able to see the last moment of my grandmother, who passed away in my last year for PhD.

I have been supported by many people throughout my graduate years, to whom I would like to acknowledge my sincere gratitute. I want to start by thanking my supervisor Willy Fischler, who not only guided me in research, but also showed me a philosophy of physicist which benefits my understanding and taste for physics. He was always patient and enthusiastic while discussing with me and came up with insightful thoughts to help me through the confusions.

Next, I would like to thank all the faculties in the theory group for creating an environment that encourages critical thinking and communications between different project groups. I have been learning a lot from the seminars and from all the other collegues in the group, which greatly broadened my view of physics. I am also grateful for all the advanced courses provided in the field of high energy theory, including a thourough and systematic demonstration to various aspects of quantum field theory by Vadim Kaplunovsky, an insightful and practical introduction of string theory by Jacques Distler and a series of rather pedagogical lectures on particle phenomenology by Can Kilic.

In the early years at UT, I was devoted to the study of Higgs field,

which was greatly helped by my collaborator Jianghao Yu. I should give him my special thanks because he continued supporting my pursue for physics till now. After switching gear to holography, when I had a hard time without products, I feel sorry for the collaborators in those projects, and thank them for their understandings. I want to also express my gratitute to Elena Caceres for her thoughtful discussions and collaborations, and for her effort to hold the holography journal club that benefits me a lot. I would like to thank all the fellow students here, especially whom I collaborated with or had fruitful discussions with, Aditya Aravind, Siva Swaminathan, Juan Pedreza, Brandon Dinunno, Stefan Eccles, Josiah Coach, Anderson Misobuchi and others.

In addition, I am thankful for Jan Duffy, our administrative assistant, for her unfailing support and also relaxing chat. I would also like to thank many Chinese fellow students in the physics department, Bangguo Xiong, Meng Li, Fei Xue and many more, with whom I had a lot of colorful and entertaining academic and non-academic activities.

Last, I want to thank my family, especially my wife Crystal who supported me without reservation. I may also thank my son Jerry, despite all the troubles he made, for bringing a lot of happiness to my life.

The material is based on work supported by the National Science Foundation under Grant Number PHY1620610.

Topics in Higgs Phenomenology and Holographic Complexity

Publication No. _____

Minglei Xiao, Ph.D.
The University of Texas at Austin, 2018

Supervisor: Willy Fischler

This dissertation presents four sample work which are divided into two very distinct categories. The first category is particle phenomenology, for which I show a series of study on the Higgs potential effects. One effect is its vacuum stability, controlled by the renormalization group running of the Higgs self coupling. The other is the impact on baryogenesis from the electroweak phase transition. A scalar-assisted vector-like fermion model is used to study the two effects, and experimental constraints are found for this model. The second category is holography, or specifically the holographic complexity. Both the time dependence and the UV divergence structure for holographic complexity are investigated. The former is done for a class of finite temperature non-commutative field theory, where both late time behavior and finite time behavior are analysed. For the UV divergence structure study, we choose the 3D kink subregion on the boundary, which is the simplest subregion with singular surface. Properties of subregion complexity are examined.

Table of Contents

List of Tables

List of Figures

Chapter 1

Introduction

The frontier of fundamental physics has two main branches: 1) to understand the quantum theories of particles and interactions without gravity, also known as particle physics or particle phenomenology, and 2) to incorporate gravity into the quantum theory, generally referred to as quantum gravity. In this dissertation, I will present my works along both of them in my very distinct projects.

1.1 Effects of Higgs Potential

Supported by some of the greatest experiments human beings have ever done, a great achievement has been made in the branch of particle phenomenology, namely the triumph of the Standard Model of particles (SM). However, since the discovery of the last building block of SM, the Higgs particle, few experimental breakthrough has been made to extend our knowledge beyond SM (BSM), which is currently the most important tasks in this field in the near future. Among the possible probes of BSM, a new probe inspired by the Higgs discovery is the effect of the Higgs potential, which will be explored by future experiments on precision Higgs measurements.

Currently, our knowledge of the Higgs potential is still far from enough. The Higgs mass, measured as 126 GeV, and the vacuum expectation value (VEV), well known as 246 GeV, are only part of the local properties of its potential at the current minimum. Based on the UV renormalizability, the SM implies a Higgs potential of the form

$$V = \mu^2 H^\dagger H + \lambda (H^\dagger H)^2 \tag{1.1}$$

which only have two parameters that are completely fixed by the two experimental data. It is plausible to keep this assumption as long as we are not going to very high energy regime, but as I will explain soon, this model already get into trouble fairly below the Planck energy, and will not stand as a valid theory all the way through the regime that phenomenologists are reasonably interested. Therefore, BSM modifications must exist for the Higgs potential. The motivation of studying Higgs potential is then to see what could modifying Higgs potential affect the known physical results.

In my view, the effects of Higgs potential on the known physical results or effects that can be detected in near future have three aspects:

1. Modifying the stability of the current Higgs vacuum and the self-interaction couplings. These are the most direct effects on the current universe. The stability determines whether the universe can exist as it is, which is a strong guarantee of the real world. The self-interaction couplings are hopefully measurable in the near future, so that the models can be tested.

2. Implying the details of electroweak phase transition. This is beyond the scope of local properties, and hence is hard to detect in a collider. But the phase transition in early universe may leave some footprints that we have access to in cosmological studies, which in turn provides a test of the models.

3. Playing a role in inflationary physics. Inflation is a very early stage of the universe when the initial conditions for inflaton-like scalars are not restricted to minima of the potential. They can often start on a slope of the potential and roll as the universe inflates. Hence inflationary physics can in principle probe scalar potential far from its minima, and Higgs as a possible fundamental scalar may play a role in such an era.

I studied all the three aspects in a series of papers [1–3]. In the first paper [1], as presented in chapter 2, I will study what kind of modifications could improve the stability of the current Higgs vacuum. The SM prediction alone shows that the current vacuum is metastable [4, 5], meaning that its lifetime before decaying to a true minimum would be longer than the current age of the universe, and hence we are temporarily safe. It is not a good news, because as shown in Fig. 1.1, the narrow band of metastability indicates that this result is very sensitive to new physics or even the precision of our current measurements. Specifically, if we are interested in BSM that contains extra fermions, like a top partner, the Higgs vacuum will definitely be unstable. In the kind of minimal extension to the SM, we use a singlet scalar to stabilize

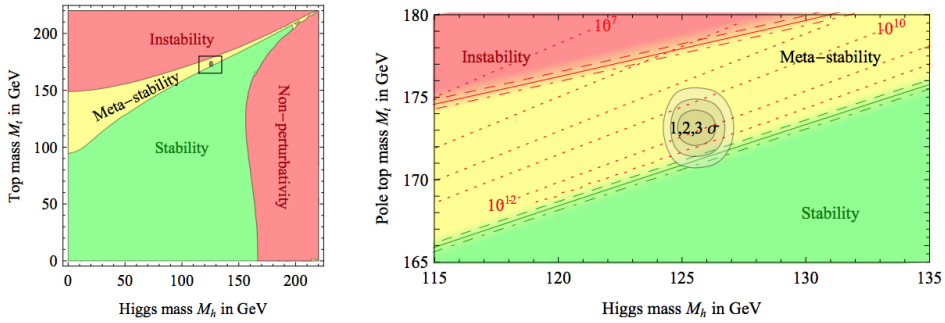

Figure 1.1: xxx

the potential. This was already proposed in [6, 7], but using scalar alone has the risk of getting into strong dynamics as the self interaction of the new scalar becomes non-perturbative at high energy. I will combine the top partner and the new scalar and show that together we have a valid model up to very high energy. I will also study the constraints on the model parameters to see the survivability of this toy model.

In the second paper in the series [2], which is explained in chapter 3, I will switch to the electroweak phase transition property of a similar toy model. Due to the existance of a new fermion and hence the new CP violation introduced by the extended CKM matrix, we expect the Sakharov's conditions for Baryogenesis to be satisfied during electroweak phase transition in this model. Baryogenesis is a necessary process in the early universe that produced enough matter-antimatter observed today, which is

$$\frac{n_b}{n_\gamma} \sim 10^{-10}. \tag{1.2}$$

The so-called Sakharov's conditions consist of three aspects: 1) there should

be a Baryon number violation interaction, which is realized by Sphaleron in electroweak baryogenesis; 2) there should be enough CP violation to break the time-reversal symmetry so that Baryon number can steadily change in one direction; 3) there should be a first order phase transition during which the bubble nucleation could freeze the net Baryon number generated during the CP violating process. Assuming enough CP violation from the extended CKM matrix, which through Dirac equation could generate net Baryon number in the phase transition bubble wall, the missing piece is hence a strong enough first order electroweak phase transition (FOPT). We scan through the parameter space of the scalar potential numerically, and find regions of parameters that allow FOPT, and hence potentially provides enough baryogenesis. Patterns of phase transitions are also classified for this kind of two-scalar field space.

I also studied inflation and dark matter in the last paper of the series [3], where we explored the possible role Higgs can play in the inflationary era. Not only do we introduce a multi-dimensional scalar space, we also assume non-minimal gravitational coupling for the scalar sector. In this setup, both the Higgs and the singlet scalar can be the inflaton, and thus we have two different inflation scenarios. What is more we set the new vector-like fermion to be SM singlet, which interacts with SM particle only through Higgs portal. Therefore, we studied the possibility that this fermion could play the role of dark matter. Various constraints from inflation, dark matter relics and particle physics are examined to give the allowed parameter range for both both scenarios.

1.2 Holographic Principle and Quantum Complexity

The idea of incorporating gravity into the quantum theory of matters has a history dating back to the establishment of the general relativity. In quantum theory, energy momentum tensor is an observable described by a Hermition operator, while the other side of the Einstein equation, the Einstein tensor, is a purely geometrical quantity. A naive way to make sense of it is to quantize the perturbation of geometry on top of a classical background, which provides an effective description of gravity in the classical and weak field limit. However, due to the non-renormalizability, it is far from a complete quantum gravity theory.

More subtleties arise when people study the behavior of a black hole. It turns out that a mathematically consistent UV cutoff scheme is not only more difficult to find, but also less natural than the physical cutoff provided by the creation of black holes, which indicates that a microscopic description of quantum gravity is closely related to the black hole physics. On the other hand, the black hole entropy found in the study of black hole thermodynamics [8, 9] implies an area law entropy, which drastically reduce the number of degrees of freedom in the quantum field theory coupled to gravity. The idea of constructing quantum theory of gravity from a lower dimensional space, as being similar to idea of hologram, is thus called holographic principle of quantum gravity [10].

As the most rigorous realization of the holographic principle, the AdS/CFT correspondence [11] provides a powerful tool to study the properties of quan-

tum gravity. Recently, in constructing the dictionary between the boundary CFT data and the bulk gravity data, it was realized that the region behind the black hole horizon is hard to probe from boundary point of view. In particular, the Einstein-Rosen Bridge (ERB) continues growing in size for time much longer than the scrambling time of the black hole [12, 13], while no familiar boundary quantities have such behavior due to the thermal equilibrium. This leads to the idea of corresponding the size of ERB to a new concept called "complexity" of the boundary quantum state, i.e. the holographic complexity [14].

In the hope of studying holographic complexity in a more concrete case, and testing the idea in a broader class of geometries, we tried to compute the holographic complexity of a non-commutative field theory [15], as shown in chapter 4. The proposal we used for this holographic dual is called "complexity = action" (CA). The gravitational action in the Wheeler-DeWitt patch is computed for the $AdS_5 \times S^5$ bulk geometry, with non-zero NS-NS 2-form field $B_{\mu\nu}$ turned on in two of the transvers directions. It will induce non-commutativity in the two directions for the world-sheet theory on the D3 branes, which makes it a non-commutative SU(N) Super Yang-Mills theory. In the bulk, there are non-trivial dilaton field, B field, R-R 2-form gauge field C_2 and the self-dual 5-form F_5. The action in type IIB supergravity is used to compute the boundary complexity holographically. The privilege of using this geometry is that the thermodynamic quantities are shown to be independent of the non-commutativity parameter. We showed, however, that the rate of

change for holographic complexity depends on this parameter, which reveals its ability to resolve better than thermodynamics. A toy quantum mechanics model is used to demonstrate this dependence. Similar computations are made for an extension of the theory to higher dimensions.

When the rate of change for holographic complexity is computed, its UV divergence is not relevant because it is usually time independent. Inspired by the fruitful studies on UV divergence structure of entanglement entropy, we investigate the UV divergence of holographic complexity in chapter 5. The UV divergence turns out to be simple for pure holographic states, thus it is natural to look at the subregion complexity. General subregion with smooth surface has been studied in [16], but we hope that interesting universal terms would appear for subregions with singular surface, similar to the case of entanglement entropy. Thus we focus on subregion complexity of the simplest subregion with singular surface: 3D kink. A systematic technique for subregion CA computation is proposed, and we find new divergence structure due to the kink feature on the subregion surface. We point out potential connection between subregion complexity and entanglement entropy according to observations of the results. There are also hints for setting values for a long-standing ambiguous parameter in the CA method.

Chapter 2

Stabilizing the Higgs vacuum

The discovery of the Higgs-like scalar boson at the Large Hadron Collider (LHC) is the great triumph of the standard model (SM) of particle physics. The Higgs boson mass, was measured at the ATLAS and CMS with reasonable accuracy: $m_h = 125.9 \pm 0.4$ GeV [17]. Now that all the parameters of the SM are determined by experimental data, the completion of the SM evoked our interest in its high energy behavior such as Higgs vacuum stability. The measured value of the Higgs boson mass leads to a very intriguing situation. The most accurate analysis of the electroweak vacuum stability in the SM was performed in [4, 5], showing that the theory sits near the boundary between stable phase and unstable phase of the vacuum structure (see Fig 2.1).

The starting point of our research [1] was a kind of BSM extensions which includes new fermions that couple to the Higgs field. Due to experimental constraints on the 4th generation chiral quarks [18, 19], and to avoid the gauge anomaly problem, we focus on the vector-like fermion models, where

This chapter is based on my previous work [1] with J. -H. Yu, in which we had equal contributions.

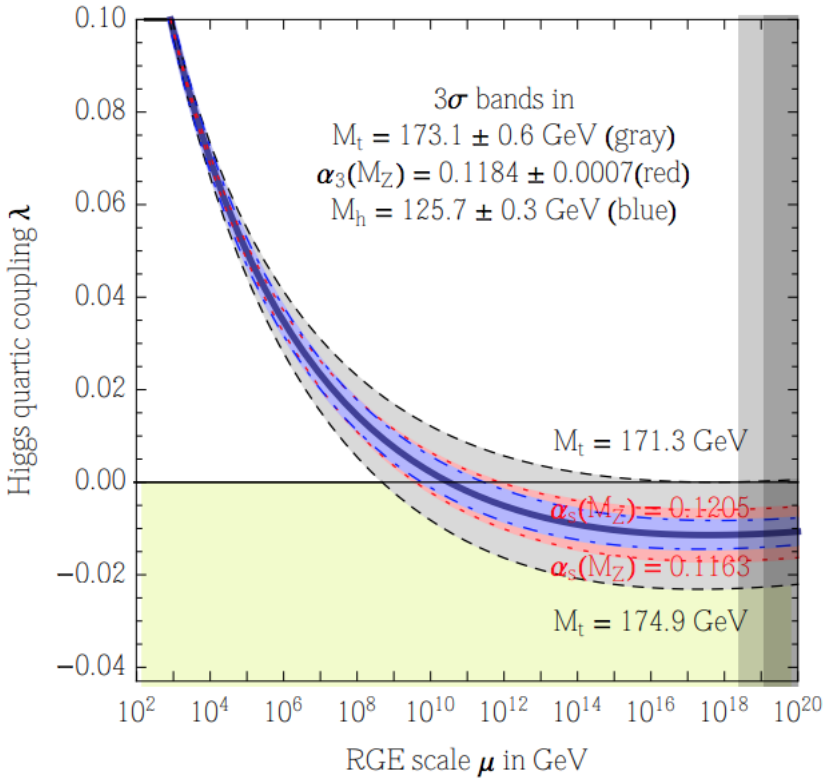

Figure 2.1: This figure shows the renormalization group running of the Higgs quartic coupling λ with slight variation of the most important model parameters. As will be explained in section 2.2, the region $\lambda < 0$ implies vacuum instability, thus we can see from this figure how different parameters influence the vacuum stability. Specifically, larger top mass (or top Yukawa coupling) leads to instability at lower energy scale.

the new fermion $\psi_{L,R}$ is singlet under the weak SU(2) gauge group, and predominantly coupled to the SM top quark [20–23]. We demand the new fermion to be a top partner, i.e. to have the same quantum number as top quark except for SU(2), so that it has tree level coupling

$$\mathcal{L}_{\text{yuk}} \supset -y_T \phi \bar{u}_{3L} \psi_R \tag{2.1}$$

to the Higgs scalar ϕ which presumably strongly affects the Higgs potential.

Similar to the top Yukawa y_t, the new coupling y_T makes the vacuum instability worse. We proposed that it can be solved if we assume that the Dirac mass term of the new fermion comes totally from the VEV of a new singlet scalar S[1], hence

$$\mathcal{L}_{\text{yuk}} \supset -\frac{y_M}{\sqrt{2}} S \bar{\psi}_L \psi_R. \tag{2.2}$$

This can be easily guaranteed by assigning +1 charge for both S and ψ_L under a global U(1) symmetry.

Therefore, the extensions of this model are in the top Yukawa sector and the scalar potential sector, characterized by the following terms:

$$\mathcal{L}_{\text{yuk}} \supset -\bar{Q}_L \tilde{H}(y_t u_{3R} + y_T \psi_R) - \frac{y_M}{\sqrt{2}} S \bar{\psi}_L \psi_R, \tag{2.3}$$

$$V(H,S) = \mu_H^2 H^\dagger H + \lambda_H (H^\dagger H)^2 + \frac{\mu_S^2}{2} S^2 + \frac{\lambda_S}{4} S^4 + \frac{\lambda_{SH}}{4} S^2 H^\dagger H. \tag{2.4}$$

where as in convention $Q_L = \begin{pmatrix} u_3 \\ d_3 \end{pmatrix}$, $H = \begin{pmatrix} \pi^\pm \\ (\phi + i\pi^0)/\sqrt{2} \end{pmatrix}$. Before we move on, there are a few things here to comment:

- We didn't write a term like $S\bar{\psi}_L u_{3R}$ in the Yukawa terms, because we can always redefine the degenerate doublet (u_{3R}, ψ_R) by a rotation so that this term vanishes.

[1] We used the letter S for the singlet scalar in the paper. For consistancy with the other works presented here, notations in this dissertation may be different from the published work.

- Using the bound-from-below condition of the potential, we have the constraints

$$\lambda_S > 0, \qquad \lambda_H > 0, \qquad 4\lambda_s\lambda_H > \lambda_{SH}^2, \tag{2.5}$$

which are imposed in the parameter scan.

- With the mixing coupling λ_{SH}, we are not restricted to negative μ_H^2 and μ_S^2. Demanding both $\langle H\rangle = (0, v/\sqrt{2})^T$ and $\langle S\rangle = u$ be non-vanishing, we have the relations

$$\mu_H^2 = -\lambda_H v^2 - \frac{\lambda_{SH}}{2}u^2, \qquad \mu_S^2 = -\lambda_S u^2 - \frac{\lambda_{SH}}{2}v^2. \tag{2.6}$$

Obviously, it's not hard to make one of them positive. Letting $\lambda_{SH} = -2\sqrt{\lambda_s\lambda_H}$ takes its lower bound, we also find that

$$\begin{aligned} \mu_H^2 &\leq -\sqrt{\lambda_H}(\sqrt{\lambda_H}v^2 - \sqrt{\lambda_s}u^2), \\ \mu_S^2 &\leq \sqrt{\lambda_s}(\sqrt{\lambda_H}v^2 - \sqrt{\lambda_s}u^2), \end{aligned} \tag{2.7}$$

indicating that either of them are upper bounded by a negative number, therefore at most one of them can be positive for spontaneous symmetry breaking.

This model will be referred to as "Scalar-Assisted Vector-like Fermion" (SAVF) model, which I studied in a series of papers [1–3]. A little difference exist between the models used in these papers. In particular, the model used here [1] has $\mathbb{Z}_2$ symmetric scalar and top partner fermion. In the next chapter, which presents [2], we loosened the $\mathbb{Z}_2$ symmetry to allow richer structure in the potential. Finally in [3] we studied a singlet new fermion, while there are additional non-minimal gravitational coupling for the scalars.

2.1 Spectrum and Mixing Angles

From the new model Eq(2.3) and the non-zero VEV (v, u), we can derive the spectrum from the quadratic terms

$$\begin{aligned} \mathcal{L}_{\text{yuk}} &\supset -\begin{pmatrix} \bar{u}_{3L} & \bar{\psi}_L \end{pmatrix} \mathcal{M}_F \begin{pmatrix} u_{3R} \\ \psi_R \end{pmatrix}, \\ V(H,S) &\supset \frac{1}{2} \begin{pmatrix} \phi & S \end{pmatrix} \mathcal{M}_S^2 \begin{pmatrix} \phi \\ S \end{pmatrix}, \end{aligned} \tag{2.8}$$

where

$$\mathcal{M}_F = \frac{1}{\sqrt{2}} \begin{pmatrix} y_t v & y_T v \\ 0 & y_M u \end{pmatrix}, \qquad \mathcal{M}_S^2 = \begin{pmatrix} 2\lambda_H v^2 & \lambda_{SH} v u \\ \lambda_{SH} v u & 2\lambda_S u^2 \end{pmatrix}. \tag{2.9}$$

These mass matrices can be diagonalized by SO(2) rotations as

$$\mathcal{M}_F = \mathcal{U}_L^\dagger \begin{pmatrix} m_t & 0 \\ 0 & m_T \end{pmatrix} \mathcal{U}_R, \qquad \mathcal{M}_S^2 = \mathcal{U}_S^\dagger \begin{pmatrix} m_h^2 & 0 \\ 0 & m_s^2 \end{pmatrix} \mathcal{U}_S. \tag{2.10}$$

where

$$\begin{pmatrix} t_L \\ T_L \end{pmatrix} = \mathcal{U}_L \begin{pmatrix} u_{3L} \\ \psi_L \end{pmatrix}, \quad \begin{pmatrix} t_R \\ T_R \end{pmatrix} = \mathcal{U}_R \begin{pmatrix} u_{3R} \\ \psi_R \end{pmatrix}, \quad \begin{pmatrix} h \\ s \end{pmatrix} = \mathcal{U}_S \begin{pmatrix} \phi \\ S \end{pmatrix} \tag{2.11}$$

are the mass eigenbasis of the mass matrices. The rotation angles therein are defined as

$$\mathcal{U}_L = \begin{pmatrix} \cos\theta_L & -\sin\theta_L \\ \sin\theta_L & \cos\theta_L \end{pmatrix}, \quad \mathcal{U}_R = \begin{pmatrix} \cos\theta_R & -\sin\theta_R \\ \sin\theta_R & \cos\theta_R \end{pmatrix}, \quad \mathcal{U}_S = \begin{pmatrix} \cos\varphi & -\sin\varphi \\ \sin\varphi & \cos\varphi \end{pmatrix}, \tag{2.12}$$

which are true physical parameters characterizing the mixing angles between the mass eigenbasis and the coupling eigenbasis. Note that the requirement of the vanishing $S\bar{\psi}_L u_{3R}$ coupling induces a constraint between θ_L and θ_R as

$$m_t \tan\theta_L = m_T \tan\theta_R, \tag{2.13}$$

the independent mixing angles are only φ and θ_L. For convenience, we introduce the shorthand notations:

$$\begin{aligned} s_\varphi &= \sin\varphi, \qquad c_\varphi = \cos\varphi, \\ s_L &= \sin\theta_L, \qquad c_L = \cos\theta_L. \end{aligned} \tag{2.14}$$

Now we can express the Lagrangian parameters in terms of the physical ones as

$$\begin{aligned} \lambda_H &= \frac{m_h^2 c_\varphi^2 + m_s^2 s_\varphi^2}{2v^2}, \qquad & y_t &= \frac{\sqrt{2} m_t m_T}{v\sqrt{m_T^2 c_L^2 + m_t^2 s_L^2}}, \\ \lambda_S &= \frac{m_h^2 s_\varphi^2 + m_s^2 c_\varphi^2}{2u^2}, \qquad & y_T &= \frac{\sqrt{2}(m_T^2 - m_t^2) s_L c_L}{v\sqrt{m_T^2 c_L^2 + m_t^2 s_L^2}}, \\ \lambda_{SH} &= \frac{(m_s^2 - m_h^2) s_\varphi c_\varphi}{uv}, & y_M &= \frac{\sqrt{2}}{u}\sqrt{m_T^2 c_L^2 + m_t^2 s_L^2}. \end{aligned} \tag{2.15}$$

To summarize this model, it introduces both a new vector-like fermion that mixes with top quark, described by its mass m_T and the mixing angle θ_L, and a singlet scalar that mixes with the Higgs boson, described by its mass m_s and the mixing angle φ. Both masses are generated predominantly by the new physics scale u, which is assumed to be at TeV scale. Regarding our motivation, both the scalar s and the fermion T have direct coupling with the Higgs, leading to deformation of the Higgs potential. We will study their influence on the potential explicitly in the next section.

2.2 Vacuum Stability from RG Improved Higgs Potential

In order to find out the true vacuum and investigate its stability, we should study the effective scalar potential which includes the radiative loop

corrections and RG-improved parameters. At the one-loop order, the effective scalar potential is [24], in the Landau gauge,

$$V_{\text{eff}}(H,S) = V(H,S;\mu) + \mathbf{STr}\frac{\mathcal{M}_i^4(H^2,S^2)}{64\pi^2}\left[\log\frac{\mathcal{M}_i^2(H^2,S^2)}{\mu^2} - c_i\right], \quad (2.16)$$

where $\mathcal{M}_i^2(H^2,S^2)$ are the field dependent mass-squared, and the index i runs over all the fields in the model, as long as the field has a mass matrix that depends on the scalars. The tree-level potential $V(H,S;\mu)$ depends on the scale μ through the running couplings, while the whole effective potential V_{eff} is supposed to be independent of μ, due to the Callan-Symanzik equation. The super-trace operator **STr** provides correct signs and degeneracies of all the field multiplets. c_i are constants that depend on the renormalization scheme. We choose the $\overline{\text{MS}}$ scheme, with $c_i = 3/2$ for scalars and fermions, and $c_i = 5/6$ for vector bosons.

The effective scalar potential V_{eff} must develop a realistic minimum at the electroweak scale v, corresponding to the SM VEV. The stability condition on the Higgs vacuum is dependent on the behavior of V_{eff} in the large-field limit $\phi \gg v = 246$ GeV. This condition is essentially equivalent to the requirement [4] that the Higgs quartic coupling $\lambda_H(\mu)$ never becomes negative up to the Planck scale. This is because at large field, we can choose $\mu \sim \phi, S$ so that $\mathcal{M}_i \sim \mu$ for most of the relevant fields and the log term in the loop correction is suppressed. Therefore it is sufficient to study the RGE running behavior of the quartic couplings $\lambda(\mu)$ in the $\overline{\text{MS}}$ scheme.

This requires us to work in the effective field theory framework, by

integrating heavy particles out at their mass thresholds and matching all the running couplings between effective theories at different scales. At the scale of the scalar pole mass M_s, we can integrate out the scalar singlet in the tree level potential $V(H, S)$ using its equation of motion:

$$S^2 = u^2 - \frac{\lambda_{SH}}{\lambda_S}(H^\dagger H - v^2/2). \tag{2.17}$$

Inserting the above equation back to $V(H, S)$, we obtain the tree-level effective Higgs potential below the heavy mass threshold:

$$V(H) = \lambda^{\rm SM}(H^\dagger H - v^2/2)^2, \tag{2.18}$$

where

$$\lambda^{\rm SM} = \lambda_H - \frac{\lambda_{SH}^2}{4\lambda_S}. \tag{2.19}$$

This shows that there is a tree-level shift when we match the Higgs quartic coupling λ_H in the model to the Higgs quartic coupling $\lambda^{\rm SM}$ in the low energy effective theory. This is consistent with the expression of the Higgs boson mass in the limit of $v \ll u$:

$$m_h^2 = 2v^2 \left(\lambda_H - \frac{\lambda_{SH}^2}{4\lambda_S} + \mathcal{O}(v^2/u^2) \right). \tag{2.20}$$

The same argument should in principle go through for the heavy fermion: at the scale of the heavy fermion pole mass M_T, we also integrate out the heavy fermion using its equation of motion. However, tree-level matching between the model and the low energy effective theory shows $y_t^{\rm SM} = y_t$. It stems from our redefinition that turns off the $S\bar{\psi}_L u_{3R}$ coupling.

Depending on different particle content in effective theories, there are different RGE running behaviors in different energy regions.

- Region I: scale $\mu < M_T, M_S$.

  In this region, after integrating out all the heavy particles, we recover the SM as the low energy theory. The SM one-loop RGE for the Higgs quartic coupling is

$$\begin{aligned}\frac{d\lambda}{d\log\mu^2} = \beta_\lambda^{\rm SM} = \frac{\lambda}{(4\pi)^2}\left[12\lambda + 6y_t^2 - \frac{9g_1^2}{10} - \frac{9g_2^2}{2}\right] \\ + \frac{1}{(4\pi)^2}\left[-3y_t^4 + \frac{9g_2^4}{16} + \frac{27g_1^4}{400} + \frac{9g_2^2g_1^2}{40}\right],\end{aligned} \tag{2.21}$$

  where $g_1 = \sqrt{5/3}g_Y$ is the hypercharge gauge coupling in GUT normalisation, and g_2 the weak $SU(2)_L$ gauge coupling. Note that for a light Higgs, the running behavior is mainly controlled by the top quark Yukawa coupling, which drives λ towards more negative values. If there is no new particle integrated in at high energies, λ would eventually become negative at energy scale around 10^{10} GeV, as indicated by the SM vacuum stability studies [4, 5].

  In order to determine the boundary condition for the running of $\lambda(\mu)$, one need to know how the $\overline{\rm MS}$ renormalized Higgs quartic coupling $\lambda(\mu)$ relates to the SM input parameters. Here the SM input parameters are taken to be the SM pole masses M_h, M_t, M_W, M_Z and Fermi constant G_F, $\alpha_s(M_Z)$. The relation that connects $\lambda(\mu)$ to the SM input parameters

can be written as

$$\lambda^{\rm SM}(\mu) = \frac{G_F M_h^2}{\sqrt{2}} \left[1 + \Delta_h(\mu)\right], \tag{2.22}$$

where $\Delta_h(\mu)$ represents electroweak one loop radiative corrections at the scale μ [25]. Similarly, the boundary condition for y_t can be determined from the relation between the pole mass and its running mass:

$$y_t^{\rm SM}(\mu) = (\sqrt{2}G_F)^{\frac{1}{2}} M_t \left[1 + \Delta_t(\mu)\right], \tag{2.23}$$

where $\Delta_t(\mu)$ denotes the electroweak radiative corrections [26]. In the RGE running, we start from the scale of the top pole mass M_t. The boundary conditions of the couplings at the M_t scale are taken from the two-loop matched values presented in Ref. [5].

- Region II (a): scale $\mu \geq M_T$ and $\mu < M_S$.

  There are two cases in the intermediate region since the model could have either $M_T < M_S$ or $M_T > M_S$. Let us first discuss the case (a): $M_T < M_S$. As explained earlier, there is no threshold effect at $\mu = m_T$, we only need to know the new RGE equation. Above the scale m_T, the heavy fermion T contributes to the one-loop running of the gauge couplings, Yukawa couplings, and Higgs quartic coupling λ_H. The RGE for the Higgs quartic coupling becomes

$$\frac{d\lambda}{d\log\mu^2} = \beta_\lambda^{\rm SM} + \frac{1}{(4\pi)^2}\left[6\lambda y_T^2 - 3y_T^4 - 6y_T^2 y_t^2\right]. \tag{2.24}$$

Due to the negative contributions from the additional terms in the above RGE, we expect the scale, at which the Higgs quartic coupling becomes negative, to be lower than that in the SM. Therefore, in the pure vector-like fermion model, the Higgs vacuum instability problem is worse than that in the SM.

- Region II (b): scale $\mu \geq M_S$ and $\mu < M_T$. This is the case when $M_T > M_S$. According to Eq. 2.19, the Higgs quartic coupling receives a positive shift at the M_S threshold

$$\lambda_H = \lambda^{\rm SM} + \frac{\lambda_{SH}^2}{4\lambda_S}, \tag{2.25}$$

which sets the initial condition of the RGE running in this region. The heavy scalar also changes the RGE running behavior of the Higgs quartic coupling, which becomes

$$\frac{d\lambda_H}{d\log\mu^2} = \beta_\lambda^{\rm SM} + \frac{1}{(4\pi)^2}\frac{1}{4}\lambda_{SH}^2. \tag{2.26}$$

The new positive contribution from the last term in the Eq. 2.26 delays the occurrence of the vacuum instability at high energies. Therefore, the above two effects on the RGE running could potentially avoid the vacuum instability.

However, we have to worry about the perturbativity bounds on the scalar quartic coupling λ_S. The RGE running of the scalar coupling is

$$\frac{d\lambda_S}{d\log\mu^2} = \frac{1}{(4\pi)^2}\left[9\lambda_S^2 + \lambda_{SH}^2\right]. \tag{2.27}$$

If there is no new heavy fermion coupled to the heavy scalar, it is very likely that the scalar coupling λ_S blows up at some energy scale, and thus violate the pertubativity bounds.

- Region III: scale $\mu \geq M_T, M_S$. In this region, both the heavy fermion and the heavy scalar are involved in the RGE running. The threshold effect, if any, would be the same as explained above. The full RGE running of the Higgs quartic coupling in this region is

$$\frac{d\lambda_H}{d\log\mu^2} = \beta_\lambda^{\rm SM} + \frac{1}{(4\pi)^2}\left[6\lambda_H y_T^2 + \frac{1}{4}\lambda_{SH}^2 - 3y_T^4 - 6y_t^2 y_T^2\right]. \tag{2.28}$$

Now the negative effect from y_T and the positive effect from λ_{SH} are both present, so whether the instability will be weakened or even avoided depends on the comparison between the two couplings.

On the other hand, we need to take care of the perturbativity bounds on the scalar coupling. The RGE running of the scalar coupling λ_S is

$$\frac{d\lambda_S}{d\log\mu^2} = \frac{1}{(4\pi)^2}\left[9\lambda_S^2 + \lambda_{SH}^2 + 6y_M^2\lambda_S - 3y_M^4\right]. \tag{2.29}$$

Without the y_M^4 term in the above equation, like in Region II(b), λ_S could blow up and reach the Landau pole at some scale below the Planck scale. The presence of new Yukawa coupling thus plays a role to avoid this trouble.

The complete RGE in three regions are listed in the Appendix 2.5. To illustrate, we show the RGE running of the Yukawa and scalar couplings

in Fig. 2.2 for a typical parameter point: $m_s = 1$ TeV, $m_T = 800$ GeV, $\sin\varphi = 0.1$, $\sin\theta_L = 0.08$ and $u = 2$ TeV .

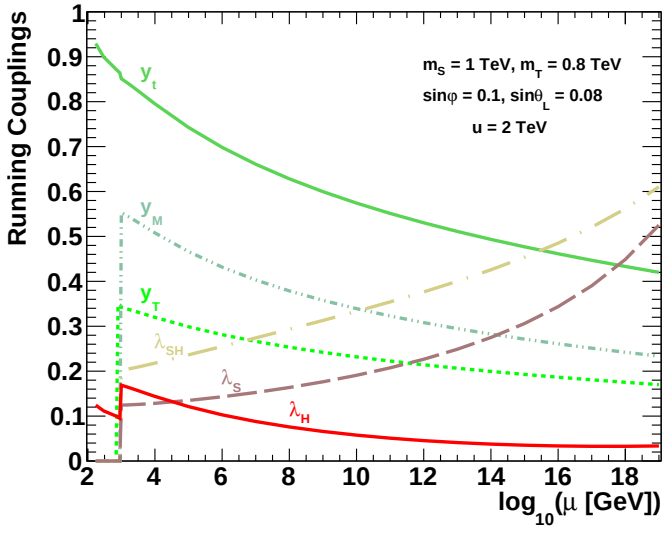

Figure 2.2: The RGE running of the Yukawa and scalar couplings in the model. All parameters are defined in the $\overline{\text{MS}}$ scheme. The starting point of the running is $m_t(M_t)$. The benchmark point: $m_s = 1$ TeV, $m_T = 800$ GeV, $\sin\varphi = 0.1$, $\sin\theta_L = 0.08$ and $u = 2$ TeV, is taken.

We could put constraints on the parameter space in the model by requiring stability of the potential and perturbativity of all the couplings. Thus we perform a numerical scan over a large range of the parameter space for all parameters: the masses m_s, m_T, the mixing angles s_φ, s_L, and the scale u.

Fig. 2.3 and Fig. 2.4 show the allowed parameter space satisfying the stability and the perturbativity conditions. As expected, in Fig. 2.3 we notice there is a small region at small s_φ excluded. It is because if the mixing angle φ

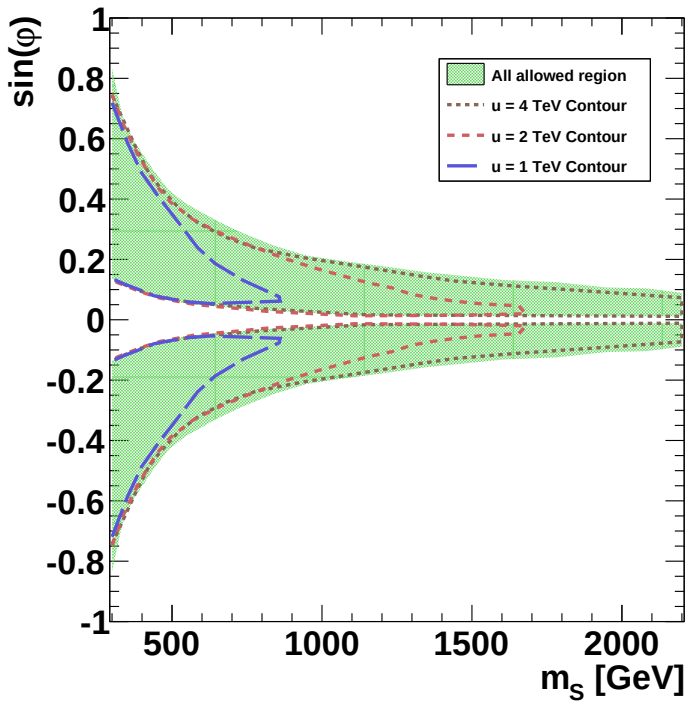

Figure 2.3: The allowed parameter region of the scalar mass and mixing angle (m_s, s_φ) satisfying the vacuum stability of the Higgs potential and perturbativity of all the running couplings. The dashed lines are the allowed contours (m_s, s_φ) for different fixed scale u.

is too small, the scalar can not give enough lift on the Higgs quartic coupling. It will still become negative, suggesting that the current vacuum is instable or metastable. Hence this excluded region correspond to stability constraint. On the other hand, the parameter region where the scalar and the Higgs have a large mixing is disfavored, especially when the scalar is heavy. The reason for this is that the scalar quartic couplings will increase as evoluting to the high

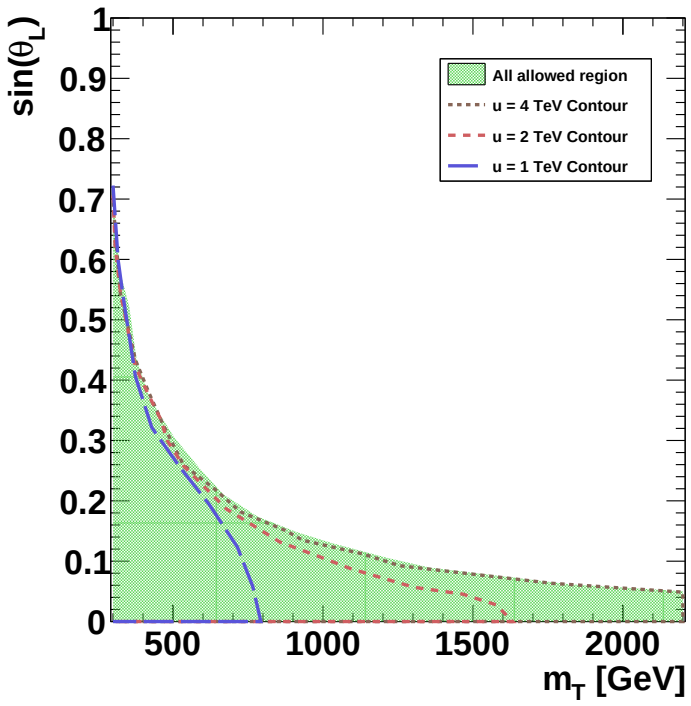

Figure 2.4: The allowed parameter region of the vector-like fermion mass and mixing angle (m_T, s_L) satisfying the vacuum stability of the Higgs potential and perturbativity of all the running couplings. The dashed lines are the allowed contours (m_T, s_L) for different fixed scale u.

energy scale, and eventually become nonperturbative. Indeed, Fig. 2.3 shows the region with large mixing angle s_φ is excluded. If we fix the scale u (dashed contours in Fig. 2.3), there is a strict bound on the mass of the scalar from the perturbativity limit on the scalar coupling strength λ_S.

Regarding to the parameter space for the heavy fermion, we expect that small s_L is favored, since the small mixing angle usually gives rise to

small Yukawa couplings y_T and less tendency of instability. As also shown in Fig. 2.4, if we fix the scale u (dashed contours), the mass of the vector-like fermion also has an upper bound since small Yukawa coupling y_M is favored.

2.3 Various Other Constraints

Now that we find the constraint on the parameter space of our model from vacuum stability, we want also to see if there are other constraints. We are going to consider the constraints from perturbative unitarity, the precision electroweak measurements and the Higgs coupling measurements.

2.3.1 Perturbative Unitarity

Although there is no bad s-dependent high energy behavior in the model, the tree-level perturbative unitarity could put constraints on the masses and couplings of the heavy particles. In the partial wave treatment [27], given the tree-level scattering amplitude $\mathcal{M}(s,\theta)$ of all possible $2 \to 2$ scattering processes, the partial wave amplitude with angular momentum l is written as

$$a_l = \frac{1}{32\pi}\int_{-1}^{1} d\cos\theta\, P_l(\cos\theta)\mathcal{M}(s,\theta), \tag{2.30}$$

where s and θ are the total energy squared, and the scattering polar angle in the center of mass frame, respectively. $P_l(\cos\theta)$ is the Legendre Polynomial. The unitarity requires the following condition [27–29]

$$|\mathrm{Re}(a_l)| \leq \frac{1}{2}. \tag{2.31}$$

In the high energy limit, following the equivalence theorem [30–33], the unitarity condition could be obtained by calculating the partial wave amplitudes of the coupled channels in the scalar sector. It has been shown [34] that the dominant contribution in the coupled channels is the process $SS \to SS$. In the high energy limit, tree level amplitude of the $SS \to SS$ is

$$\begin{aligned}\mathcal{M}(\frac{1}{\sqrt{2}}SS \to \frac{1}{\sqrt{2}}SS) = \frac{1}{64v^2u^2}\Big[&6(m_H^2+5m_s^2)(v^2+u^2)\\ &+3(m_H^2+15m_s^2)(v^2-u^2)\cos(2\varphi)\\ &-6(m_H^2-3m_s^2)(v^2+u^2)\cos(4\varphi)\\ &-3(m_H^2-m_s^2)(v^2-u^2)\cos(6\varphi)\\ &-12(m_H^2-m_s^2)2vu\sin^3(2\varphi)\Big].\end{aligned} \tag{2.32}$$

Put it back to the unitarity condition Eq. 2.31, we obtain the constraints on the parameter space. In the limit of no mixing between the Higgs and the scalar, it gives a constraint on m_s against u:

$$m_s < \sqrt{\frac{4\pi}{3}}u. \tag{2.33}$$

On the other hand, the heavy fermion also has an upper bound on its mass and coupling s_L from the requirement of the perturbative unitarity through the fermion anti-fermion scattering process. At high energy $\sqrt{s} \gg m_T$, the tree level amplitude of the process $T\bar{T} \to T\bar{T}$ is

$$\mathcal{M}(T\bar{T} \to T\bar{T})_{\lambda_i\lambda_f} = m_T^2(u^{-2}c_L^4 + v^{-2}s_L^4)\begin{pmatrix}1&0&0&0\\0&0&-1&0\\0&-1&0&0\\0&0&0&1\end{pmatrix} \tag{2.34}$$

where λ_i and λ_f are the helicity states of the initial and final states. λ_i and λ_f are taken to be one of the following helicity states $\{++, +-, -+, --\}$. Diagonalizing it and taking the largest s wave component, we have the unitarity condition

$$a_0^{max} = \frac{1}{16\pi}\left[m_T^2(u^{-2}c_L^4 + v^{-2}s_L^4)\right] < \frac{1}{2}. \tag{2.35}$$

Similarly, if there is no mixing between the vector-like fermion and the top quark, it gives a constraint on m_T against u:

$$m_T < \sqrt{8\pi}u. \tag{2.36}$$

2.3.2 Precision Electroweak Measurements

The presence of the new scalar S and the vector-like fermion T renders both modified SM couplings and new electroweak couplings. These new couplings have impact on the electroweak observables that were precisely measured at the LEP and SLC.

The dominant NP (New Physics) effects on the electroweak observables appearing in the gauge boson vaccuum polarization correlations, named oblique corrections [35], are parametrized by three independent parameters S, T and U:

$$\alpha S \equiv 4e^2\left[\Pi'_{33}(0) - \Pi'_{3Q}(0)\right], \tag{2.37}$$

$$\alpha T \equiv \frac{e^2}{s_W^2 c_W^2 m_Z^2}\left[\Pi_{11}(0) - \Pi_{33}(0)\right], \tag{2.38}$$

$$\alpha U \equiv 4e^2\left[\Pi'_{11}(0) - \Pi'_{33}(0)\right]. \tag{2.39}$$

where the notation Π_{XY} with $X, Y = 1, 3, Q$ denotes the vacuum polarization amplitudes and $\Pi'_{XY}(q^2) = \frac{d}{dq^2}\Pi_{XY}(q^2)$. From the global fit of the electroweak precision data, the constraints on the S, T and U parameters can be obtained. The following fit results are determined from the GFitter fit [36] for the reference SM parameters $m_t = 173$ GeV and $m_h = 126$ GeV. In the NP model, the contribution of the U parameter is usually very small and can be neglected. Fixing $U = 0$, the GFitter global fit results in

$$\begin{aligned} \Delta S &= S^{\rm NP} - S^{\rm SM} = 0.05 \pm 0.09 \\ \Delta T &= T^{\rm NP} - T^{\rm SM} = 0.08 \pm 0.07. \end{aligned} \tag{2.40}$$

and the correlation coefficient is taken to be 0.91.

We split the calculation on the oblique parameters into boson-loop contributions $T_S,\ S_S$ and fermion-loop contributions $T_F,\ S_F$, and consider them separately. For the boson-loop contributions, the NP effect is only involved in the vacuum polarization amplitudes where the Higgs or the heavy scalar are in the loop. This is shown by Feynman diagrams in Fig. 2.5. Using the vector boson self-energy Π_{VV} defined in the Appendix 2.6, we obtain

$$\begin{aligned} \Delta T_S &= s_\varphi^2 \Big[T_s(m_s^2) - T_s(m_h^2) \Big], \\ \Delta S_S &= s_\varphi^2 \Big[S_s(m_s^2) - S_s(m_h^2) \Big], \end{aligned} \tag{2.41}$$

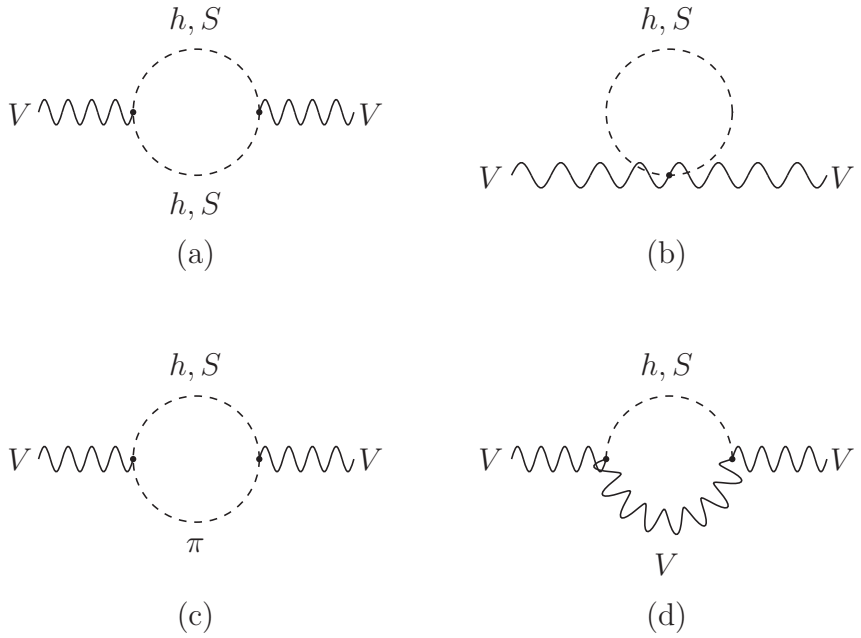

Figure 2.5: The one-loop Feynman diagrams of the vector boson self-energy Π_{VV} due to the scalars in the loop.

where the functions are defined as

$$
\begin{aligned}
T_s(m) = &-\frac{3}{16\pi c_W^2}\Bigg[\frac{1}{(m^2-m_Z^2)(m^2-m_W^2)} \\
&\times\Big(m^4\ln m^2 - s_W^{-2}(m^2-m_W^2)m_Z^2\ln m_Z^2 \\
&+ s_W^{-2}c_W^2(m^2-m_Z^2)m_W^2\ln m_W^2\Big) - \frac{5}{6}\Bigg], \\
S_s(m) = &\frac{1}{12\pi}\Bigg[\ln m^2 - \frac{(4m^2+6m_Z^2)m_Z^2}{(m^2-m_Z^2)^2} \\
&+ \frac{(9m^2+m_Z^2)m_Z^4}{(m^2-m_Z^2)^3}\ln\frac{m^2}{m_Z^2} - \frac{5}{6}\Bigg].
\end{aligned}
$$

Similarly, it is straightforward to calculate the oblique corrections due to the top quark and the vector-like fermion shown in Fig. 2.6. Subtracting

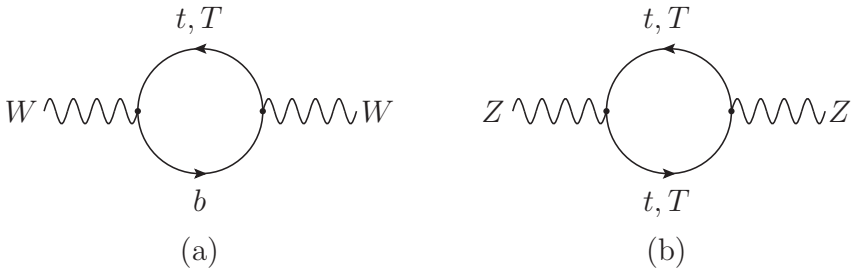

Figure 2.6: The one-loop Feynman diagrams of the vector boson self-energy Π_{VV} due to heavy fermions in the loop.

the SM contributions due to the third generation quarks

$$\begin{aligned} T_F^{\rm SM} &= \frac{3m_t^2}{4\pi e^2 v^2}, \\ S_F^{\rm SM} &= \frac{1}{2\pi}\left(1-\frac{1}{3}\log\frac{m_t^2}{m_b^2}\right), \end{aligned} \tag{2.42}$$

we arrive at the final expressions

$$\begin{aligned} \Delta T_F &= T^{\rm SM} s_L^2\Big[-(1+c_L^2)+s_L^2\frac{m_T^2}{m_t^2} \\ &\quad + c_L^2\frac{2m_T^2}{m_T^2-m_t^2}\ln\frac{m_T^2}{m_t^2}\Big], \\ \Delta S_F &= -\frac{s_L^2}{6\pi}\Big[(1-3c_L^2)\ln\frac{m_T^2}{m_t^2}+5c_L^2 \\ &\quad - \frac{6c_L^2 m_t^4}{(m_T^2-m_t^2)^2}\Big(\frac{2m_T^2}{m_t^2}-\frac{3m_T^2-m_t^2}{m_T^2-m_t^2}\ln\frac{m_T^2}{m_t^2}\Big)\Big], \end{aligned} \tag{2.43}$$

which agree with the results in Ref. [20].

The only important non-oblique correction comes from the vertex correction of the $Zb\bar{b}$ coupling. In general, the effective $Zb\bar{b}$ vertex can be parametrized as

$$\frac{g_2}{c_W}\bar{b}\gamma^\mu\left[g_L\frac{1-\gamma_5}{2}+g_R\frac{1+\gamma_5}{2}\right]bZ_\mu, \tag{2.44}$$

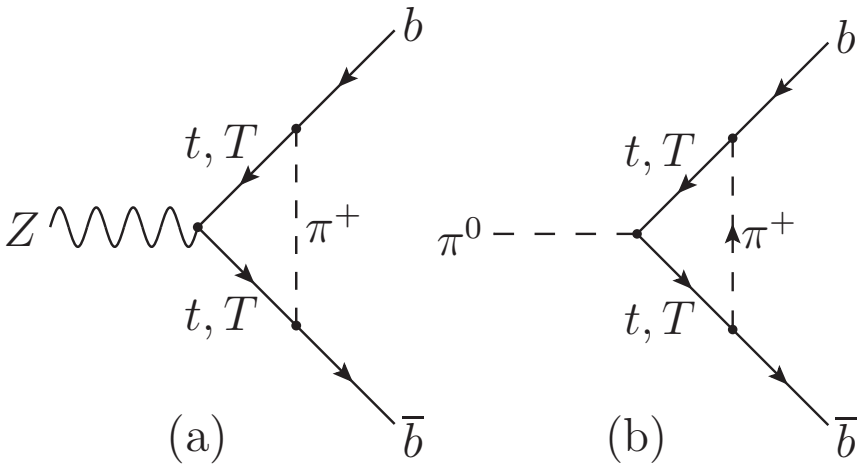

Figure 2.7: (a) the dominant one-loop Feynman diagrams in the t'Hooft-Feynman gauge; (b) the only Feynman diagrams after the gaugeless limit is taken in the model.

where

$$\begin{aligned} g_L &= g_L^{\rm SM} + \delta g_L^{\rm NP}, \\ g_R &= g_R^{\rm SM} + \delta g_R^{\rm NP}. \end{aligned} \tag{2.45}$$

Here $g^{\rm SM}$ denotes the SM coupling with radiative correction included, and $\delta g^{\rm NP}$ represents the correction purely from the NP model. In the SM, taking the leading m_t-dependent radiative corrections into account, the SM couplings are

$$\begin{aligned} g_L^{\rm SM} &= -\frac{1}{2} + \frac{1}{3}s_W^2 + \frac{m_t^2}{16\pi^2 v^2}, \\ g_R^{\rm SM} &= \frac{1}{3}s_W^2. \end{aligned} \tag{2.46}$$

In our model, there is no tree-level correction to the $Zb\bar{b}$ coupling. However, at one-loop, flavor-dependent vertex corrections arise, and contribute to the $Zb_L\bar{b}_L$ coupling. Fig. 2.7(a) shows the dominant one-loop Feynman diagram

in the t'Hooft-Feynman gauge, in which the vector-like fermion and the top quark appear in the loop. The presence of vertex corrections gives rise to non-zero $\delta g_L^{\rm NP}$. To extract out the leading m_T-dependent terms explicitly, we perform the loop calculation in the "gaugeless" limit [37–40], in which the Z boson is treated as a non-propagating external field coupled to the current $J^\mu = \bar{b}_L \gamma^\mu b_L$. Using the Wald identity [37, 38], the leading contribution to the $Z b_L \bar{b}_L$ coupling can be obtained via the calculation of the higher dimensional operator $\frac{\partial_\mu \pi^0}{m_Z} \bar{b}_L \gamma^\mu b_L$, where π^0 is the Goldstone boson eaten by the Z boson. The relevant Feynman diagram is shown in Fig. 2.7(b). The one-loop effective Lagrangian that is generated by the Feynman diagram is

$$\mathcal{L}_{\pi b \bar{b}} = \epsilon_b \frac{2}{v} \bar{b}_L \gamma^\mu b_L \partial_\mu \pi^0, \tag{2.47}$$

where

$$\begin{aligned} \epsilon_b = -\frac{1}{16\pi^2 v^2} \Big[& m_t^4 c_L^4 C_0(m_t^2, m_t^2, 0) + m_T^4 s_L^4 C_0(m_T^2, m_T^2, 0) \\ & + 2 m_t^2 m_T^2 c_L^2 s_L^2 C_0(m_t^2, m_T^2, 0) \Big], \end{aligned} \tag{2.48}$$

Here $C_0(m_1^2, m_2^2, m_3^2)$ is the three-point Passarino-Veltman (PV) function [41] in the zero external momentum limit, where m_i are the masses of the particles in the triangle loop. In the limit of the massless Goldstone boson, the three-point PV function reduces to

$$C_0(m_1^2, m_2^2, 0) = \begin{cases} -\dfrac{1}{m_1^2 - m_2^2} \ln \dfrac{m_1^2}{m_2^2} & \text{if } m_1 \neq m_2 \\ -\dfrac{1}{m_1^2} & \text{if } m_1 = m_2. \end{cases} \tag{2.49}$$

In the decoupling limit, taking $s_L \to 0$ in Eq. 2.48 one recovers the leading m_t-dependent contribution in the SM:

$$\epsilon_b^{\rm SM} = \frac{m_t^2}{16\pi^2 v^2}. \tag{2.50}$$

Based on the Ward identity in Ref. [37, 38], we recognize the coefficient ϵ_b in Eq. 2.47 is proportional to the quantity we are interested in

$$\delta g_L^{\rm NP} = \epsilon_b - \epsilon_b^{\rm SM}. \tag{2.51}$$

So we obtain the expression for the NP correction $\delta g_L^{\rm NP}$:

$$\begin{aligned}\delta g_L^{\rm NP} = \frac{m_t^2 s_L^2}{16\pi^2 v^2}\Big[&-(1+c_L^2) \\ &+ s_L^2 \frac{m_T^2}{m_t^2} + c_L^2 \frac{2m_T^2}{m_T^2 - m_t^2} \ln \frac{m_T^2}{m_t^2}\Big].\end{aligned} \tag{2.52}$$

Note that the terms inside the bracket are the same as in Eq. 2.43.

Among all electroweak observables, three of them are related to the $Z\bar{b}b$ couplings: $\mathcal{A}_b$, $A_{FB}^{0,b}$, and R_b. It is known that the asymmetries $\mathcal{A}_b$ and $A_{FB}^{0,b}$ are mainly sensitive to $\delta g_R^{\rm NP}$, while the R_b mainly sets constraint on $\delta g_L^{\rm NP}$. Due to the dominant corrections on the $\delta g_L^{\rm NP}$, we will make use of the observable R_b to constrain the parameter space. The shift in R_b due to new physics is

$$\delta R_b = 2R_b(1-R_b)\frac{g_L \delta g_L^{\rm NP} + g_R \delta g_R^{\rm NP}}{g_L^2 + g_R^2}. \tag{2.53}$$

The experimental value and SM theoretical value (including two loop corrections) [17] is

$$\begin{aligned} R_b^{\rm exp} &= 0.21629 \pm 0.00066 \\ R_b^{\rm th} &= 0.21575 \pm 0.00003. \end{aligned} \tag{2.54}$$

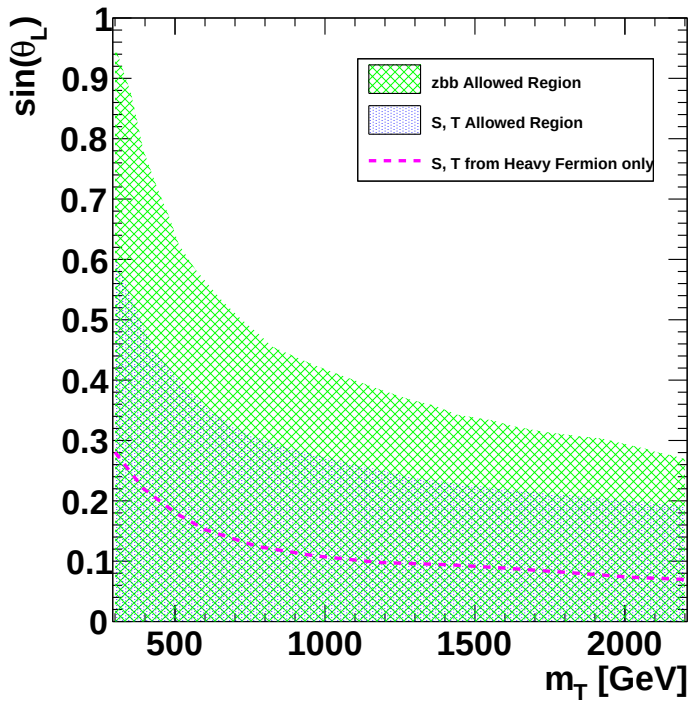

Figure 2.8: The allowed region from the oblique corrections S, T, and $Z\bar{b}_L b_L$ at the 95% confidence level. Below the pink dash line is the allowed region from the S, T parameters in the pure vector-like fermion model.

Following the Ref. [42], $\delta g_L^{\rm NP}$ is determined to be $\delta g_L = 0.0028 \pm 0.0014$.

The experimental constraints on the oblique parameters and the $Z\bar{b}b$ couplings set limits on the parameter space in the model. We scan over a large range of the parameter space, and obtain the allowed paramter region at the 95% confidence level (CL). We find that all the parameter space on the (m_s, s_φ) in the scalar sector are allowed. This means the constraint from the

electroweak precision data on the scalar sector is quite weak. However, only part of the parameter space on the (m_T, s_L) in the top sector is allowed, as is shown in Fig. 2.8. Since all the NP corrections are proportional to s_L^2, there is a upper limit on the s_L. Fig. 2.8 shows the decoupling nature of the vector-like fermion: as the fermion becomes heavier, there are less allowed region of the mixing angle. The constraint from the non-universal correction to the $Zb\bar{b}$ coupling is weaker than the one from the universal oblique corrections. The tightest constraint comes from the T parameter, since the vector-like fermion is in the singlet representation of the electroweak group, which contributes to the custodial symmetry breaking in the model at the loop level. The dashed line in the Fig. 2.8 shows tighter constraints in the pure vector-like fermion model than in our model. The relaxed constraint on T parameter in our model is due to the opposite correction from the boson loops with respect to the fermion contribution. Therefore, the existence of the heavy scalar leads to larger allowed parameter space.

2.3.3 Constraints from Higgs Measurements and Direct Search

There can in principle be constraint from Higgs coupling measurements, due to the mixing angle

$$g_{h;i}^{\mathrm{NP}} = g_{h;i}^{\mathrm{SM}} c_\varphi \tag{2.55}$$

wehre $g_{h;i}$ is some coupling involving the higgs field. It is obvious that the constraint on the scalar mass m_s will be weak. On the other hand, for couplings also involving the top quark like g_{htt}, the mixing angle θ_L could also be

constrained. However, as top does not appear in the decay channel, we can only expect its contributions to loop process like $g_{h\gamma\gamma}$ or g_{hgg} may constrain the fermion sector:

$$\begin{aligned} g_{hgg}^{\rm SM} &= \frac{g_s^2}{16\pi^2}\sum_f \frac{g_{hff}^{\rm SM}}{m_f} A_{1/2}(\tau_f), \\ g_{h\gamma\gamma}^{\rm SM} &= \frac{e^2}{16\pi^2}\left[\frac{g_{\rm hWW}^{\rm SM}}{m_W^2}A_1(\tau_W) + \sum_f 2N_c^f Q_f^2 \frac{g_{hff}^{\rm SM}}{m_f}A_{1/2}(\tau_f)\right], \end{aligned} \tag{2.56}$$

where the sum over f runs over t, b, s, c quarks, and $\tau_i = \frac{4m_i^2}{m_h^2}$. Here the loop function $A_1(\tau)$ and $A_{1/2}(\tau)$ are

$$\begin{aligned} A_{1/2}(\tau) &= 2\,\tau\left[1 + (1-\tau)f(\tau)\right], \\ A_1(\tau) &= -2 - 3\tau\left[1 + (2-\tau)f(\tau)\right]. \end{aligned} \tag{2.57}$$

with

$$f(x) = \begin{cases} \arcsin^2[1/\sqrt{x}]\ , & \text{for } x \geq 1\ , \\ -\frac{1}{4}\left[\ln\frac{1+\sqrt{1-x}}{1-\sqrt{1-x}} - i\pi\right]^2\ , & \text{for } x < 1. \end{cases} \tag{2.58}$$

Due to Eq 2.55, the NP couplings take the form

$$\begin{aligned} g_{hgg}^{\rm NP} &= \frac{g_s^2}{16\pi^2}\left(\sum_f \frac{g_{hff}}{m_f}A_{1/2}(\tau_f) + \frac{g_{hTT}}{m_T}A_{1/2}(\tau_T)\right), \\ g_{h\gamma\gamma}^{\rm NP} &= \frac{e^2}{16\pi^2}\left[\frac{g_{\rm hWW}}{m_W^2}A_1(\tau_W) + \sum_f 2N_c^f Q_f^2\frac{g_{hff}}{m_f}A_{1/2}(\tau_f)\right. \\ &\quad \left. + \frac{8}{3}\frac{g_{hTT}}{m_T}A_{1/2}(\tau_T)\right]. \end{aligned} \tag{2.59}$$

Due to the saturated behavior of the function $A_{1/2}(\tau_T)$ for a heavy m_T, the constraint on the m_T is weak. Finally the constraint is mainly on the $\varphi - \theta_L$ subspace of the parameters, shown in the Fig 2.9.

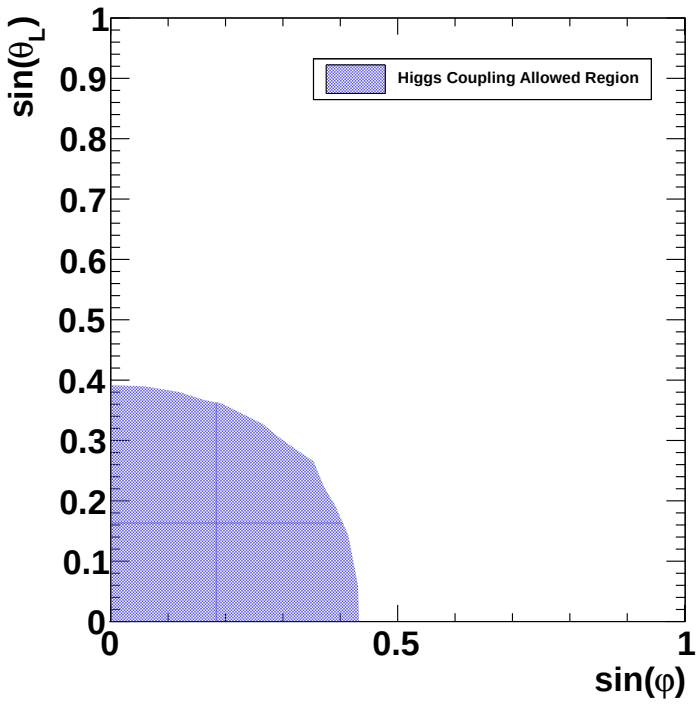

Figure 2.9: The allowed parameter region for the parameters (s_φ, s_L) in the model at the 95% CL.

There are many direct searches on the vector-like quarks which couple predominantly to the third-generation quarks at the Tevatron and the LHC. At the LHC, the vector-like quark could be produced in pair through QCD production $pp \to T\bar{T}$, or be singly produced via electroweak process $pp \to T\bar{b}$. For a light vector-like fermion, the pair production cross section is larger than the one in the single production, while for a heavy vector-like fermion the single production is more efficient. The main decay channels of the heavy

vector-like fermion are

$$T \to tZ, \quad T \to bW, \quad T \to th, \tag{2.60}$$

and $T \to tS$ only if the scalar is much lighter than the vector-like fermion. In the model, the tree-level partial decay widths are given by

$$\begin{aligned}
\Gamma_{T\to bW} &= \frac{s_L^2 m_T^3}{32\pi v^2}\left(1+\mathcal{O}(\frac{m_W^2}{m_T^2})\right), \\
\Gamma_{T\to tZ} &= \frac{s_L^2 m_T^3}{64\pi v^2}\left((1-\frac{m_t^2}{m_T^2})^3+\mathcal{O}(\frac{m_Z^2}{m_T^2})\right), \\
\Gamma_{T\to th} &= \frac{s_L^2 c_L^2 c_\varphi^2 m_T^3}{64\pi v^2}\left(1+\frac{5m_t^2}{m_T^2}+\mathcal{O}(\frac{m_h^2}{m_T^2},\frac{m_t^4}{m_T^4},\frac{v^2}{u^2})\right).
\end{aligned} \tag{2.61}$$

Taking the limit $m_T \gg m_t, m_h$, the partial decay widths have the following pattern:

$$\Gamma_{T\to bW} : \Gamma_{T\to tZ} : \Gamma_{T\to th} \simeq 2:1:1. \tag{2.62}$$

This can be understood using Goldstone equivalence theorem [31–33].

In a recent CMS analysis [43], using the 8 TeV data collected up to integrated luminosity of 19.5 fb^{-1}, the up-to-dated lower limits on the mass of the heavy fermion are set to be around $687-782$ GeV depending on different patterns of the vector-like quark decay branching ratios. Setting the pattern of the branching ratio as $2:1:1$, we could put a limit on the vector-like fermion mass: 696 GeV.

Regarding the direct search of the new scalar, because the heavy scalar in this model is CP-even, the same as the SM Higgs boson, the search limits

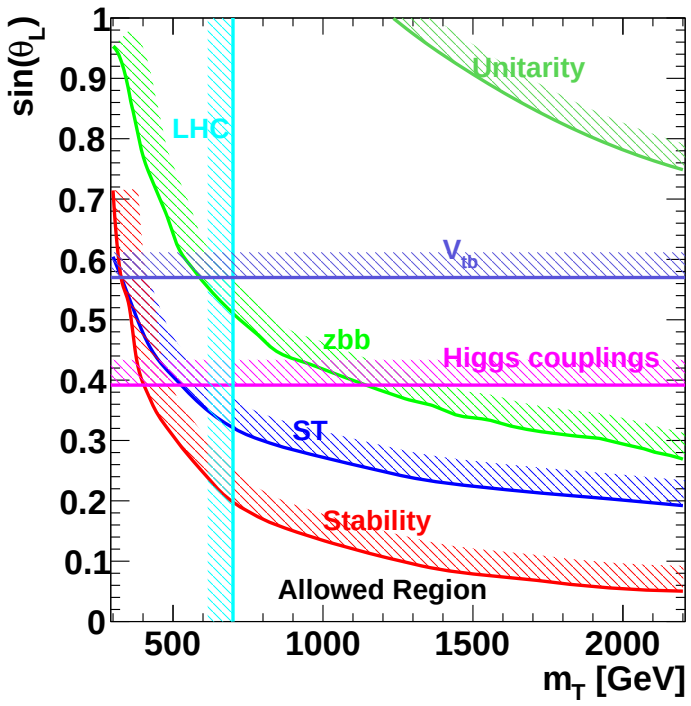

Figure 2.10: Exclusion plot on the parameters $m_T - \sin\theta_L$ with all current constraints included. The exclusion zones are on the shadow side of each line. The allowed region is shown as the zone delimited by the tightest constraints from the Stability and the LHC.

on the high mass Higgs boson at the Tevatron and the LHC could be used to set constraints on the mass and couplings of the heavy scalar. The production mechanism is similar to the Higgs boson, dominanted by the gluon fusion with the production cross section $\sigma_{gg\to S}$. The decay channels of the heavy scalar

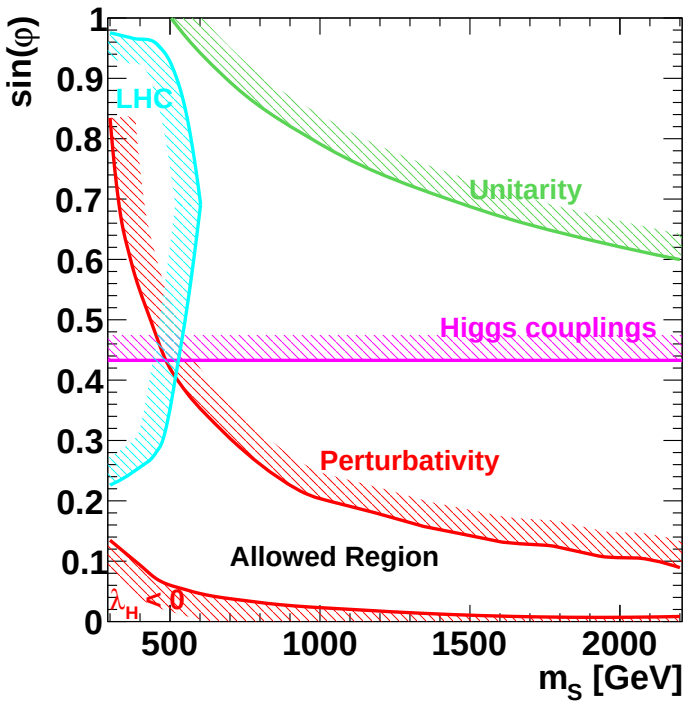

Figure 2.11: Exclusion plot on the parameters $m_s - \sin\varphi$ with all current constraints included. The exclusion zones are on the shadow side of each line. The allowed region is shown as the zone delimited by the tightest constraints from the Perturbativity, the Stability ($\lambda_H < 0$), and the LHC.

are

$$S \to WW, \quad S \to ZZ, \quad S \to hh, \quad S \to t\bar{t}, \tag{2.63}$$

and $S \to tT$ only if the vector-like fermion is much lighter than the scalar. Other decay channels, such as $S \to \gamma\gamma/gg$, $S \to f\bar{f}$, where f is the fermion other than the top quark, are negligible. Similar to the vector-like fermion

case, by Goldstone equivalence theorem we have the partial widths of decay modes as $\Gamma_{S\to WW} : \Gamma_{S\to ZZ} : \Gamma_{S\to hh} \simeq 2 : 1 : 1$.

In an up-to-dated analysis from the CMS [44], the searches in $S \to WW$ and $S \to ZZ$ decay channels are studied in the mass range between 145 GeV and 1000 GeV. If the high mass Higgs boson has the same coupling as the SM, the mass range between 145 GeV and 710 GeV are excluded at the 95% CL. We convert this constraint into the limit on the heavy scalar in the model. After calculating the production cross section and the decay branching ratios of the heavy scalar, we perform a scan over the whole range of the parameter space, which is shown in Fig. 2.11. It is shown that a range of the parameter space with light scalar mass and moderate mixing angle is ruled out.

2.4 Summary of the Model

We investigated a vector-like fermion coupled to a new singlet scalar and the third generation quarks. The singlet scalar extended the Higgs sector, through the mixing with the Higgs boson. In our setup, the mass of the vector-like fermion is purely generated from symmetry breaking of the singlet scalar. We carefully examined the electroweak vacuum stability and scalar perturbativity via the renormalization group evolution of the Higgs quartic coupling, and the scalar quartic couplings. The matching condition when integrating out heavy particles, and the relation between the running and physical parameters, were considered. Although the vector-like fermion provides negative contributions to the running of the Higgs quartic coupling, the new

scalar contributes positively. In the matching of the renormalization group, the Higgs quartic coupling obtains a positive threshod shift at the scale of the scalar mass. We performed a scan over the parameter space, and studied the constraints from vacuum stability, perturbativity and perturbed unitarity, together with experimental constraints from the precision electroweak observables, Higgs coupling precision measurements and the LHC direct searches. In Fig. 2.10, and Fig. 2.11, we summarized current constraints on the parameter space of the top sector $(m_T, \sin\theta_L)$ and the scalar sector $(m_s, \sin\varphi)$. We observed that the instability only happens in a very small region close to the zero mixing angle in the scalar sector, which means that the model is very powerful in stabilizing the Higgs vacuum.

2.5 Appendix I: Renormalization Group Equations in SAVF model

In this section, we list the one-loop RGEs in different effective field theories appearing in the Scalar-Assisted Vector-like-Fermion model, as used in Chapter 2. This model includes a new vector-like fermion which has the same quantum number as top quark except for the weak SU(2) group. The additional scalar singlet has a $\mathbb{Z}_2$ symmetry, and hence only has new quartic couplings λ_{SH} and λ_S.

At the scale $\mu > M_S, M_T$, both the heavy scalar and the vector-like fermion are involved in the RGE running. The gauge coupling RGEs are

$$\begin{aligned}
\frac{dg_1^2}{d\ln\mu^2} &= \frac{g_1^4}{(4\pi)^2}\left[\frac{41}{10}+\frac{16}{15}\right], \\
\frac{dg_2^2}{d\ln\mu^2} &= \frac{g_2^4}{(4\pi)^2}\left[-\frac{19}{6}\right], \\
\frac{dg_3^2}{d\ln\mu^2} &= \frac{g_3^4}{(4\pi)^2}\left[-7+\frac{2}{3}\right],
\end{aligned} \tag{2.64}$$

where $g_1^2 = 5g_Y^2/3$ is the hypercharge gauge coupling in GUT normalisation. The second part in the bracket is due to the presence of the top partner, which is zero for $SU(2)_L$ because it's a singlet under this group.

The Yukawa coupling RGEs are

$$\begin{aligned}
\frac{dy_t^2}{d\ln\mu^2} &= \frac{y_t^2}{(4\pi)^2}\left[\frac{9y_T^2}{2}+\frac{9y_t^2}{2}+\frac{3y_b^2}{2}+y_\tau^2-\frac{17g_1^2}{20}-\frac{9g_2^2}{4}-8g_3^2\right],\\
\frac{dy_b^2}{d\ln\mu^2} &= \frac{y_S^2}{(4\pi)^2}\left[\frac{3y_t^2}{2}+\frac{9y_b^2}{2}+\frac{3y_T^2}{2}+y_\tau^2-\frac{g_1^2}{4}-\frac{9g_2^2}{4}-8g_3^2\right],\\
\frac{dy_\tau^2}{d\ln\mu^2} &= \frac{y_\tau^2}{(4\pi)^2}\left[3y_t^2+3y_b^2+3y_T^2+\frac{5y_\tau^2}{2}-\frac{9g_1^2}{4}-\frac{9g_2^2}{4}\right],\\
\frac{dy_T^2}{d\ln\mu^2} &= \frac{y_T^2}{(4\pi)^2}\left[\frac{9}{2}y_T^2+\frac{9}{2}y_t^2+\frac{3}{2}y_b^2+y_\tau^2+\frac{1}{4}y_M^2-\frac{17}{20}g_1^2-\frac{9}{4}g_2^2-8g_3^2)\right],\\
\frac{dy_M^2}{d\ln\mu^2} &= \frac{y_M^2}{(4\pi)^2}\left[y_T^2+\frac{9}{2}y_M^2-\frac{8}{5}g_1^2-8g_3^2\right].
\end{aligned} \tag{2.65}$$

If there is only the new fermion T, i.e. the region II(a), y_M is not present and should be taken as 0 in the equations for other couplings. If T is also not involved, either in region I or II(b), one only has the first three Yukawa couplings with $y_T = y_M = 0$ in the equations.

The RGEs in the Higgs sector are

$$\begin{aligned}
\frac{d\lambda_H}{d\ln\mu^2} &= \frac{1}{(4\pi)^2}\left[\lambda_H\left(12\lambda_H+6y_t^2+6y_b^2+2y_\tau^2+6y_T^2-\frac{9g_1^2}{10}-\frac{9g_2^2}{2}\right)\right.\\
&\quad\left.+\left(\frac{1}{4}\lambda_{SH}^2-3y_t^4-3y_b^4-y_\tau^4-3y_T^4-6y_t^2y_T^2+\frac{27g_1^4}{400}+\frac{9g_2^4}{16}+\frac{9g_2^2g_1^2}{40}\right)\right],\\
\frac{d\lambda_{SH}}{d\ln\mu^2} &= \frac{1}{(4\pi)^2}\left[\lambda_{SH}(2\lambda_{SH}+6\lambda_H+3\lambda_S+3y_t^2+3y_b^2+y_\tau^2+3y_T^2+3y_M^2)\right.\\
&\quad\left.-\lambda_{SH}\left(\frac{9g_1^2}{20}+\frac{9g_2^2}{4}\right)-6y_T^2y_M^2\right],\\
\frac{d\lambda_S}{d\ln\mu^2} &= \frac{1}{(4\pi)^2}\left[9\lambda_S^2+6y_M^2\lambda_S+\lambda_{SH}^2-3y_M^4\right].
\end{aligned} \tag{2.66}$$

The latter two couplings only appear when the heavy scalar S is involved. The absence of the heavy fermion will lead to $y_T = y_M = 0$ in the equations.

2.6 Appendix II: Calculation of the Oblique Parameters S, T

In this section we present the computation of the S, T parameters with Passarino-Veltman functions [41].

2.6.1 General Formulae For Gauge Boson Self-Energy

We list the general formulae for the gauge boson self-energy functions Π_{ij}, where i, j denote the gauge boson species. In the formulae, only the one-point PV function $A_0(m^2)$, and the two-point PV functions $B_0(p^2, m_1^2, m_2^2)$, $B_{00}(p^2, m_1^2, m_2^2)$ are involved. In the calculation of the oblique parameters, all the self-energy functions Π_{ij} and their derivatives $\Pi'_{ij} = \frac{d\Pi}{dp^2}$, are computed at $p^2 = 0$. Various contributions from fermion and scalar loops are summarized as follows:

- Fermion Loop Contribution

$$\begin{aligned}
\Pi_{ij}^{ff} =& -\frac{N_c}{16\pi^2}\Big[(g_{iL}g_{jL} + g_{iR}g_{jR})\Big(4B_{00}(0, m_{f1}^2, m_{f2}^2) \\
&- (m_{f1}^2 + m_{f2}^2)B_0(0, m_{f1}^2, m_{f2}^2) - A_0(m_{f1}^2) - A_0(m_{f2}^2)\Big) \\
&+ 2m_{f1}m_{f2}(g_{iL}g_{jR} + g_{iR}g_{jL})B_0(0, m_{f1}^2, m_{f2}^2)\Big], \\
\Pi_{ij}^{\prime ff} =& -\frac{N_c}{16\pi^2}\Big[(g_{iL}g_{jL} + g_{iR}g_{jR})\Big(4B'_{00}(0, m_{f1}^2, m_{f2}^2) \\
&- (m_{f1}^2 + m_{f2}^2)B'_0(m_{f1}^2, m_{f2}^2) + B_0(0, m_{f1}^2, m_{f2}^2)\Big) \\
&+ 2m_{f1}m_{f2}(g_{iL}g_{jR} + g_{iR}g_{jL})B'_0(0, m_{f1}^2, m_{f2}^2)\Big],
\end{aligned} \tag{2.67}$$

where g_{iL} and g_{iR} are the left-handed and right-handed couplings of the

gauge boson labelled i to the fermions running in the loop, from the vertex

$$\bar{f}_1 \gamma^\mu (g_{iL} P_L + g_{iR} P_R) f_2 A_\mu. \tag{2.68}$$

- Scalar Tadpole Contribution

$$\Pi^s_{ij} = -g A_0(m_s^2), \tag{2.69}$$

$$\Pi'^s_{ij} = 0, \tag{2.70}$$

where g is the coupling strength of the $s-s-V-V$ four-point coupling.

- Scalar Loop Contribution

$$\Pi^{ss}_{ij} = 4 g_i g_j B_{00}(0, m_{s1}^2, m_{s2}^2), \tag{2.71}$$

$$\Pi'^{ss}_{ij} = 4 g_i g_j B'_{00}(0, m_{s1}^2, m_{s2}^2), \tag{2.72}$$

where g_i is the coupling strength of the $s-s-V$ three-point coupling involving gauge boson labelled i.

- Scalar-Vector Loop Contribution

$$\Pi^{vs}_{ij} = -g_i g_j B_0(0, m_v^2, m_s^2), \tag{2.73}$$

$$\Pi'^{vs}_{ij} = -g_i g_j B'_0(0, m_v^2, m_s^2), \tag{2.74}$$

where g_i is the coupling strength of the $s-V-V$ three-point coupling involving gauge boson labelled i.

2.6.2 The Oblique Parameters S, T

We present the contributions to the S, T from the fermion loops and the boson loops, seperately.

2.6.3 The Fermion Loops

The T parameter is computed as

$$\alpha T \equiv \frac{e^2}{s_W^2 c_W^2 m_Z^2} \left[\Pi_{11}(0) - \Pi_{33}(0)\right] = \frac{\Pi_{WW}}{m_W^2} - \frac{\Pi_{ZZ}}{m_Z^2} - \frac{2s_W}{c_W}\frac{\Pi_{Z\gamma}}{m_Z^2}, \tag{2.75}$$

where for fermion loops the last term on the right-hand side does not contribute. In the SM, the fermion contributions mainly come from the third generation quarks:

$$\Pi_{WW}^{SM} = \Pi_{WW}^{tb,SM}, \tag{2.76}$$

$$\Pi_{ZZ}^{SM} = \Pi_{ZZ}^{tt,SM} + \Pi_{ZZ}^{bb,SM}. \tag{2.77}$$

In our model, there are new contributions from the vector-like fermion T:

$$\Pi_{WW} = \Pi_{WW}^{tb} + \Pi_{WW}^{Tb}, \tag{2.78}$$

$$\Pi_{ZZ} = \Pi_{ZZ}^{tt} + 2\Pi_{ZZ}^{tT} + \Pi_{ZZ}^{TT} + \Pi_{ZZ}^{bb,SM}. \tag{2.79}$$

Subtracting the SM contribution, the NP correction on the parameter T from the fermion loops can be obtained

$$\Delta T_F = \frac{1}{\alpha}\Big[\frac{1}{m_W^2}\left(\Pi_{WW}^{tb} + \Pi_{WW}^{Tb} - \Pi_{WW}^{tb,SM}\right) - \frac{1}{m_Z^2}\left(\Pi_{ZZ}^{tt} + 2\Pi_{ZZ}^{tT} + \Pi_{ZZ}^{TT} - \Pi_{ZZ}^{tt,SM}\right)\Big]. \tag{2.80}$$

The S parameter is defined as

$$S = 16\pi\big(\Pi'_{33} - \Pi'_{3\gamma}\big). \tag{2.81}$$

In the SM, the fermion contributions are

$$\Pi'^{SM}_{33} = \Pi'^{tt,SM}_{33} + \Pi'^{bb,SM}_{33}, \tag{2.82}$$

$$\Pi'^{SM}_{3\gamma} = \Pi'^{tt,SM}_{3\gamma} + \Pi'^{bb,SM}_{3\gamma}. \tag{2.83}$$

while the new model gives

$$\Pi'^{SM}_{33} = \Pi'^{tt}_{33} + 2\Pi'^{tT}_{33} + \Pi'^{TT}_{33} + \Pi'^{bb,SM}_{33}, \tag{2.84}$$

$$\Pi'^{SM}_{3\gamma} = \Pi'^{tt}_{3\gamma} + 2\Pi'^{tT}_{3\gamma} + \Pi'^{TT}_{3\gamma} + \Pi'^{bb,SM}_{3\gamma}. \tag{2.85}$$

Therefore the NP correction on the parameter S from the fermion loops is

$$\Delta S_F = 16\pi\left[\left(\Pi'^{tt}_{33} + 2\Pi'^{tT}_{33} + \Pi'^{TT}_{33} - \Pi'^{tt,SM}_{33}\right) - \left(\Pi'^{tt}_{3\gamma} + 2\Pi'^{tT}_{3\gamma} + \Pi'^{TT}_{3\gamma} - \Pi'^{tt,SM}_{3\gamma}\right)\right]. \tag{2.86}$$

2.6.4 The Boson Loops

To compute the boson contributions, it is convenient to split them into the gauge parts $(\widetilde{T}_v, \widetilde{S}_v)$ and the scalar parts $(\widetilde{T}_s, \widetilde{S}_s)$:

$$T_S = \widetilde{T}_v + \widetilde{T}_s, \quad S_S = \widetilde{S}_v + \widetilde{S}_s, \tag{2.87}$$

where the tilde indicates there are divergences in each part $(\widetilde{T}, \widetilde{S})$, while the total boson constributions to (T_S, S_S) are convergent. The gauge parts consist of the contributions from the W/Z loops, the ghost loops and the Goldstone

loops, which are not altered in our model. So the gauge parts will not contribute to ΔT_S and ΔS_S in our model. The scalar parts $(\widetilde{T}_s, \widetilde{S}_s)$ consist of all the loops that involve the Higgs boson, or any new real scalars that mix with the Higgs boson. In the following, we will only consider the contributions to the ΔT_S and ΔS_S from the scalar parts.

In the SM, the self-energy functions involving the Higgs boson are

$$\Pi_{WW}^{SM} = \frac{1}{2}\Pi_{WW}^{h,SM} + \Pi_{WW}^{hW,SM} + \Pi_{WW}^{h\pi^{\pm},SM}, \tag{2.88}$$

$$\Pi_{ZZ}^{SM} = \frac{1}{2}\Pi_{ZZ}^{h,SM} + \Pi_{ZZ}^{hZ,SM} + \Pi_{ZZ}^{h\pi^{0},SM}, \tag{2.89}$$

while there is no Higgs boson contribution in the two-point function $\Pi_{Z\gamma}$. Inserting the above self-energy functions back to T parameter definition, due to the cancellation between the first terms in the W and Z self-energy functions, we obtain the scalar part $\widetilde{T}_s^{SM}$

$$\widetilde{T}_s^{SM} = \frac{1}{\alpha}\Big[\frac{\Pi_{WW}^{hW,SM} + \Pi_{WW}^{h\pi^{\pm},SM}}{m_W^2} - \frac{\Pi_{ZZ}^{hZ,SM} + \Pi_{ZZ}^{h\pi^{0},SM}}{m_Z^2}\Big], \tag{2.90}$$

$$= \frac{3}{16\pi c_W^2}\Delta + T_s(m_h), \tag{2.91}$$

where Δ is the divergent term $\Delta = \frac{2}{4-d} - \gamma + \ln 4\pi\mu^2$ in the $\overline{MS}$ scheme. Here the finite part is written as a function of the scalar mass m

$$T_s(m) = -\frac{3}{16\pi c_W^2}\Bigg[-\frac{5}{6} + \frac{1}{(m^2-m_Z^2)(m^2-m_W^2)}\times \left(m^4\log m^2 - \frac{(m^2-m_W^2)m_Z^2}{s_W^2}\log m_Z^2 + \frac{c_W^2(m^2-m_Z^2)m_W^2}{s_W^2}\log m_W^2\right)\Bigg]. \tag{2.92}$$

The calculation is done in the $\overline{MS}$ scheme, without loss of generality.

In our model, the self-energy functions involving the Higgs boson and the new scalar are

$$\Pi_{WW} = \frac{1}{2}(\Pi^{h}_{WW} + \Pi^{S}_{WW}) + (\Pi^{hW}_{WW} + \Pi^{SW}_{WW}) + (\Pi^{h\pi^{\pm}}_{WW} + \Pi^{S\pi^{\pm}}_{WW}), \tag{2.93}$$

$$\Pi_{ZZ} = \frac{1}{2}(\Pi^{h}_{ZZ} + \Pi^{S}_{ZZ}) + (\Pi^{hZ}_{ZZ} + \Pi^{SZ}_{ZZ}) + (\Pi^{h\pi^{0}}_{ZZ} + \Pi^{h\pi^{0}}_{ZZ}). \tag{2.94}$$

Note that the first terms do not contribute to the T parameter, as in the SM. Similarly, we obtain the scalar part $\widetilde{T}_s$

$$\widetilde{T}_s = \frac{1}{\alpha}\Big[\frac{\Pi^{hW}_{WW} + \Pi^{h\pi^{\pm}}_{WW}}{m^2_W} - \frac{\Pi^{hZ}_{ZZ} + \Pi^{h\pi^{0}}_{ZZ}}{m^2_Z}\Big] + \frac{1}{\alpha}\Big[\frac{\Pi^{SW}_{WW} + \Pi^{S\pi^{\pm}}_{WW}}{m^2_W} - \frac{\Pi^{SZ}_{ZZ} + \Pi^{S\pi^{0}}_{ZZ}}{m^2_Z}\Big] \tag{2.95}$$

$$= c^2_{\varphi}\left(\frac{3\Delta}{16\pi c^2_W} + T_s(m_h)\right) + s^2_{\varphi}\left(\frac{3\Delta}{16\pi c^2_W} + T_s(m_S)\right) \tag{2.96}$$

$$= \frac{3\Delta}{16\pi c^2_W} + c^2_{\varphi}T_s(m_h) + s^2_{\varphi}T_s(m_S), \tag{2.97}$$

where the divergent part is the same as the SM as expected. As the new scalar only contribute to the part $\widetilde{T}_s$ via mixing with the SM Higgs, common factors s_{φ} and c_{φ} could be extracted, leaving a SM-like $\tilde{T}_s(m)$. Hence the function $T_s(m)$ can be used to obtain a concise form for the $\widetilde{T}_s$ in our model. Subtracting the SM contribution $\widetilde{T}^{SM}_s$ in Eq. 2.91, we get a finite and very concise result for ΔT_S

$$\Delta T_S = \Delta\widetilde{T}_s = s^2_{\varphi}\Big[T_s(m_S) - T_s(m_h)\Big], \tag{2.98}$$

The S parameter can be defined in an alternative way using the hyper-chage Y,

$$S \equiv -16\pi\Pi'_{3Y}, \tag{2.99}$$

which reduces a lot of work for boson contributions. The Higgs dependent part $\widetilde{S}_s$ in the SM is

$$\widetilde{S}_s^{SM} = -16\pi\Big(\Pi_{3Y}'^{hZ,SM} + \Pi_{3Y}'^{h\pi^0,SM}\Big) \tag{2.100}$$

$$= -\frac{1}{12\pi}\Delta + S_s(m_h), \tag{2.101}$$

where

$$S_s(m) = \frac{1}{12\pi}\left[\ln m^2 - \frac{5}{6} - \frac{(4m^2+6m_Z^2)m_Z^2}{(m^2-m_Z^2)^2} + \frac{(9m^2+m_Z^2)m_Z^4}{(m^2-m_Z^2)^3}\ln\frac{m^2}{m_Z^2}\right]. \tag{2.102}$$

For the same reason as in T_S calculation, when we turn to the new model, it has a very concise form

$$\widetilde{S}_s = c_\varphi^2\Big(-\frac{\Delta}{12\pi} + S_s(m_h)\Big) + s_\varphi^2\Big(-\frac{\Delta}{12\pi} + S_s(m_S)\Big) \tag{2.103}$$

$$= -\frac{\Delta}{12\pi} + c_\varphi^2 S_s(m_h) + s_\varphi^2 S_s(m_S), \tag{2.104}$$

and similarly

$$\Delta S_S = \Delta\widetilde{S}_s = s_\varphi^2\Big[S_s(m_S) - S_s(m_h)\Big]. \tag{2.105}$$

Chapter 3

Electroweak Baryogenesis

The baryonic matter that remains after the baryon-antibaryon annihilation, makes up around 5% of the total energy density of the universe. It is puzzling that the universe does not have equal amounts of matter and antimatter. We can characterize the asymmetry between matter and antimatter in terms of the baryon-to-photon ratio

$$\eta \equiv \frac{n_B}{n_\gamma}, \tag{3.1}$$

where $n_B = n_b - n_{\bar{b}}$ is the difference between the number density of baryons and antibaryons, and n_γ is the number density of photon. The n_γ is introduced to prevent the parameters η from diluting during the expansion of the universe after nucleosynthesis. The baryonic matter desity n_B at present time has been consistently measured by the big bang nucleosynthesis and the fluctuations of the cosmic microwave background. The Planck result for the cosmological density parameter [45]

$$\Omega_B h^2 = 0.02226 \pm 0.00016, \tag{3.2}$$

This chapter is based on my previous work [2] with J. -H. Yu, in which we had equal contributions.

translates to the baryon-to-photon ratio

$$\eta = (6.05 \pm 0.07) \times 10^{-10}. \tag{3.3}$$

Explaining the observed baryon asymmetry has been one of the greatest challenges of particle physics and cosmology. As the entropy production during inflation could greatly dilute and thus wash out any existing baryon asymmetry, it is reasonable to assume a zero baryon number density after the inflation. Later, the asymmetry is generated dynamically through the so-called "baryogenesis". It has been suggested by Sakharov [46] long time ago that the general baryogenesis has three necessary conditions: baryon number violation, sufficient C and CP violation, and departure from thermal equilibrium. Hence, we look forward to a mechanism in which these three conditions are satisfied and could provide the observed baryon asymmetry.

Electroweak baryogenesis [47–49] (EWBG) offers a theoretically attractive and experimentally testable mechanism to realize baryogenesis. The great attraction of this mechanism is that the baryogenesis took place at or near the electroweak scale, suggesting that it might be probed in the near future by experiments at the accelerators. The EWBG proceeds as follows (see [50–55] for reviews). At temperatures far above the electroweak scale, the electroweak symmetry is manifest, which implied a high sphaleron rate that preserves baryon symmetry in thermal equilibrium. As the universe cools down to near the electroweak phase transition scale, bubbles of the symmetry-broken vacuum began to emerge and grow. CP violating processes involving

the electroweak sector were triggered at the expanding wall of the bubbles, leaving baryons inside the bubbles and antibaryons outside. Through the rapid sphaleron transitions in the unbroken phase, the excess of antibaryons are washed out. Meanwhile, if the sphaleron rate in the broken phase could be suppressed enough, the excess of baryons inside the bubbles could survive. We can easily realize a Boltzmann suppression of the sphaleron rate, because the sphaleron has an excitation energy E_{sph} that is related to the Higgs VEV v. It has been shown [56] that the suppression is strong enough when

$$E_{sph}/T_c \geq 45, \tag{3.4}$$

which serves as the condition for a *strong first-order phase transition* in the context of electroweak baryogenesis.

The standard model (SM) contains all the necessary ingredients to realize electroweak baryogenesis: baryon number is violated by sphaleron processes; CP violation comes from the Cabbibo-Kobayashi-Maskawa (CKM) matrix; departure from equilibrium is realized by the bubble nucleation and expansion during the first-order electroweak phase transition (EWPT). However, given the observed Higgs boson mass $M_H = 125$ GeV, the EWPT is not strong enough to suppress the sphaleron rate inside the bubbles [57]. Also, the CP violation in the CKM matrix is not large enough to generate the expected asymmetry. Therefore a successful electroweak baryogenesis needs new physics beyond the Standard Model. The new physics should provide new sources of CP violation that can be manifested by the advancing bubble walls, and also

provide strong enough first order EWPT. Both conditions require the existence of new physics at around the electroweak scale that directly couples to the SM Higgs sector. A simple and economic way to realize the strong first order EWPT is to add a new scalar which couples to the Higgs boson, such as the singlet extended standard model, etc [58–66]. Moreover, if the scalar is a real singlet [62, 66], the cubic terms could exist in the potential at tree-level, and therefore the phase transition gets stronger without the need of the thermally induced barrier.

In the work [2], we use the SAVF model without $\mathbb{Z}_2$ symmetry for the scalar S to study the electroweak baryogenesis. The vector-like fermion in the model is supposed to extend the 3×3 CKM matrix to a 3×4 matrix, which provides additional sources of CP violation. Due to the coupling between Higgs and the new scalar, the phase transition occurs in an extended scalar space, which leads to more possibilities. We will discuss the scalar potential in detail, and investigate how the extended scalar sector provides us the strong first order EWPT. Furthermore, we classify the phase transition patterns and explore the parameter preferences in each pattern using the shape of the zero-derivative curves of the scalar potential.

3.1 CP Violation from Vector-like Fermion

In the SM, the CP violation is characterized by the quark-rephasing invariant quantity, the Jarlskog invariant [67]

$$J_{CP} = (m_t^2 - m_c^2)(m_t^2 - m_u^2)(m_c^2 - m_u^2)(m_b^2 - m_s^2)(m_b^2 - m_d^2)(m_s^2 - m_d^2)A, \quad (3.5)$$

where

$$A = \mathrm{Im} V_{ud} V_{cb} V_{ub}^* V_{cd}^* \tag{3.6}$$

is twice the area of the unitarity triangle of the CKM matrix. As the SM CKM matrix only has 1 independent CP phase, the three unitarity conditions give the same area, which is the only CP violating source. This quantity can also be written as [68]

$$J_{CP} = -\frac{i}{2} \det[H_u, H_d], \tag{3.7}$$

where $H_u = M_u M_u^\dagger$ and $H_d = M_d M_d^\dagger$ are the building blocks of rephasing invariants. In the picture of electroweak baryogenesis, this quantity provides a dimensionless CP violation strength $J_{CP}/T_c^{12} \sim 10^{-20}$, which is too small compared to the typical strength of Baryogenesis $\eta \sim 10^{-10}$. We observe that both the fermion masses and the unitarity triangle A suppress the CP violation. One resolution is to add more massive fermions and extend the unitarity triangle to polygon with larger area. However, the most simple extension, hence the 4th generation model, is ruled out by the experiment data [18, 19]. Our hope would be to get larger CP violation from the new vector-like fermion in our model.

Despite the tight constraints on the flavor mixing between the new vector-like fermion and the first two generations, these mixings are still essential for the new CP violation. If we consider the three families of the quarks in the SM, the Yukawa couplings y_t and y_T becomes matrix Y_{ij}^u and vector Y_i' in

the flavor space. With explicit flavor indices, the Yukawa Lagrangian becomes

$$\begin{aligned}\mathcal{L}_{\rm Yuk} = &-Y^d_{ij}\overline{Q}_{Li}\Phi\, d_{Rj} - Y^u_{ij}\overline{Q}_{Li}\tilde{\Phi}\, u_{Rj} \\ &- Y'_i\overline{Q}_{Li}\tilde{\Phi}\, U_R - y_s s\overline{U}_L U_R - M\overline{U}_L U_R + \text{h.c.}\end{aligned} \tag{3.8}$$

The mass term of the fermion sector is

$$\mathcal{L}_{\rm mass} = -\begin{pmatrix}\overline{u}_{Li} & \overline{U}_L\end{pmatrix}\begin{pmatrix}vY^u_{ij} & vY'_i \\ 0 & M + y_s u\end{pmatrix}\begin{pmatrix}u^j_R \\ U_R\end{pmatrix} - vY^d_{ij}\overline{d}_{Li}d^j_R + \text{h.c.}. \tag{3.9}$$

Hereafter we identify

$$\mathcal{M}^u_{IJ} = \begin{pmatrix}vY^u_{ij} & vY'_i \\ 0 & M + y_s u\end{pmatrix}, \quad \mathcal{M}^d_{ij} = vY^d_{ij}, \tag{3.10}$$

where I and J run over 1 to 4.

It was investigated that in the vector-like bottom partner model [69], the CP violation is characterized by 7 Jarlskog-like invariants (J-invariants). The top partner model should be similar. In the simple case of chiral limit $m_u = m_d = m_s = m_c = 0$, only one of them is independent:

$$\begin{aligned}J &= \text{Im }\mathbf{Tr}(H_d H_u h_u h_u^\dagger) \\ &= m_b^2 m_T^2 m_t^2 (m_T^2 - m_t^2) B_2,\end{aligned} \tag{3.11}$$

where B_2 is the only rephrasing invariant constructed from the new CKM matrix that is non-vanishing in this chiral limit.

To estimate the strength of CP violation in our model, we need to look at the experimental constraints on the heavy fermion mass and the extended CKM matrix elements. We will show later that the heavy fermion mass would be around TeV scale. For the latter, current experiments on flavor physics,

such as K and B decay and $B-\bar{B}$ mixing were analyzed in the literature[70, 71] by performing a global fitting on the 4×3 CKM matrix elements using 68 flavor physics observables [71]. The analysis includes the direct measurements of the CKM elements, CP violation in $K_L \to \pi\pi$, branching fraction of the decay $K^+ \to \pi^+\nu\bar{\nu}$, branching fraction of the decay $K_L \to \mu^+\mu^-$, $Z \to b\bar{b}$ decay, $B_q^0 - \bar{B}_q^0$ mixing ($q = d, s$), indirect CP violation in $B_d^0 \to J/\psi K_S$ and $B_s^0 \to J/\psi\phi$, CKM angle γ, branching ratio of $B \to X_s\ell^+\ell^-$ ($\ell = e, \mu$), branching ratio of $B \to X_s\gamma$, branching ratio of $B \to K\mu^+\mu^-$, constraints from $B \to K^*\mu^+\mu^-$, branching ratio of $B^+ \to \pi^+\mu^+\mu^-$, branching ratio of $B_q \to \mu^+\mu^-$ ($q = s, d$), branching ratio of $B \to \tau\bar{\nu}$, like-sign dimuon charge asymmetry A_{SL}^b, and finally the oblique parameters S and T. The results of the global fitting are shown in Table 5 and 6 of Ref. [71] for $m_T = 800$ GeV and 1200 GeV. The results suggest that B_2 could be as large as 10^{-6} for a TeV top partner. More importantly, the enhancement from the heavy top quark mass implies a J-invariant of order $J \leq 10^{11}\text{GeV}^8$. Assuming that the typical energy scale during the baryogenesis is the critical temperature of EW phase transition T_c, the dimensionless CP violation strength formulated as J/T_c^8 needs to be greater than the observed baryon number asymmetry.

$$\frac{J}{T_c^8} \geq \eta \sim 10^{-10}, \tag{3.12}$$

which sets an upper bound for the critical temperature $T_c \leq 420\text{TeV}$.[1]

[1]It is argued that the W mass m_W is another typical energy scale, and it should contribute several powers in the denominator in the expression of dimensionless CP violation strength. In that case, the upper bound could be pushed higher to TeV scale.

3.2 First Order Phase Transition

3.2.1 Finite Temperature Scalar Potential

To study the phase transition, we consider the scalar potential at finite temperature (see Ref. [52] for review). Starting from the zero temperature one-loop order Coleman-Weinberg potential Eq 2.16, with the field dependent masses $\mathcal{M}_i(H,S)$ defined in Appendix 3.5. Additional counter-terms are introduced to preserve the definition of input parameters in the formula

$$\frac{\partial(V_{\rm CW}+V_{\rm CT})}{\partial\phi_i}\Big|_{\phi_i=\langle\phi_i\rangle}=0, \tag{3.13}$$

$$\frac{\partial^2(V_{\rm CW}+V_{\rm CT})}{\partial\phi_i\partial\phi_j}\Big|_{\phi_i=\langle\phi_i\rangle}=\mathcal{M}^2_{ij}, \tag{3.14}$$

where $\phi_i=\phi,S$ and m^2_{ij} are elements of the non-$\mathbb{Z}_2$ extension of the tree level mass squared matrix defined in Eq. 2.9:

$$\mathcal{M}_s^2\equiv\begin{pmatrix}m^2_{\phi\phi} & m^2_{\phi S}\\ m^2_{S\phi} & m^2_{SS}\end{pmatrix}=\begin{pmatrix}2\lambda_H v^2 & \mu_{SH}v+\lambda_{SH}uv\\ \mu_{SH}v+\lambda_{SH}uv & 2\lambda_S u^2+\mu_3 u-\frac{\mu_{S\phi}v^2}{2u}\end{pmatrix}. \tag{3.15}$$

Note that the above conditions need additional care for massless fields. For example, the Goldstone boson contribution to the scalar masses in Eq. 3.14 is infrared log-divergent due to its zero pole mass. This indicates that renormalizing the scalar potential at zero external momenta is not a well-defined procedure. An alternative on-shell renormalization procedure was proposed [59, 72, 73] to cure the problem. Here we list the final expression of the zero

temperature one-loop effective potential:

$$V_{\rm CW}^{\rm on-shell}(\phi,S)=V_{\rm tree}(\phi,S)+\mathbf{STr}_{i\neq G}\left[\frac{\mathcal{M}_i^4(\phi,S)}{64\pi^2}\left(\log\frac{\mathcal{M}_i^2(\phi,S)}{\mathcal{M}_i^2(v,u)}-\frac{2}{3}\right)\right.$$
$$\left.+2\mathcal{M}_i^2(v,u)\mathcal{M}_i^2(\phi,S)\right]+\frac{3}{64\pi^2}\mathcal{M}_G^4(\phi,s)\log\frac{\mathcal{M}_G^2(v,u)}{M_h^2}. \tag{3.16}$$

The one-loop thermal corrections at temperature T is

$$V_{\rm thermal}(\phi,S,T)=\sum_i\frac{n_iT^4}{2\pi^2}J_{\rm B,F}\left(\frac{\mathcal{M}_i^2(\phi,S)}{T^2}\right), \tag{3.17}$$

where

$$J_{\rm B,F}(y)=\int_0^\infty dx x^2\log\left[1\mp e^{-\sqrt{x^2+y}}\right]. \tag{3.18}$$

with the sign $-$ for bosons and $+$ for fermions.

On the other hand, to understand the dominant contributions at the high temperature, it is also useful to expand the thermal functions $J_{\rm B,F}$ in the high temperature regime. At high temperature limit, the thermal corrections can be expanded as

$$V_{\rm thermal}(\phi,s,T)\simeq\sum_{i={\rm B,F}}\left(n_i\frac{c_i\pi^2}{90}T^4+\frac{|n_i|}{24(1+\delta_{i{\rm F}})}\mathcal{M}_i^2(\phi,s)T^2\right.$$
$$\left.-\frac{n_i}{64\pi^2}\mathcal{M}_i^4(\phi,s)\log\frac{\mathcal{M}_i^2(\phi,s)}{a_iT^2}\right) \tag{3.19}$$
$$-\sum_{j={\rm B}}\frac{n_i}{12\pi}\left[\mathcal{M}_i^2(\phi,s)\right]^{3/2}T,$$

where $\delta_{i{\rm F}}=0$ for bosons and 1 for fermions, and the coefficients $c_{\rm B}=-1$ for bosons and $c_{\rm F}=\frac{7}{8}$ for fermions, $a_{\rm B}=16\pi^2\exp(3/2-2\gamma_E)$ for bosons and $a_{\rm F}=\pi^2\exp(3/2-2\gamma_E)$ for fermions.

The finite-temperature potential needs to be corrected, due to the infrared divergences, generated by bosonic long-range fluctuations called Matsubara zero modes. The dominant contribution[2] arises from the ring diagrams, which include the quadratic divergences going like T^2. This can be solved schematically by resumming over all diagrams with bubbles attached to the big loop [74–76]. This leads to a shift of the bosonic field-dependent masses $m_i^2(\phi, s)$ to the thermal field-dependent masses

$$\mathcal{M}_i^2(\phi, s, T) \equiv \mathcal{M}_i^2(\phi, s) + \Pi_i(T), \tag{3.20}$$

where the thermal shifts Π_i are defined in Appendix 3.5. After resummation, the ring-diagram contribution to the effective potential reads

$$V_{\text{ring}} = -\frac{T}{12\pi} \sum_{i=\text{B}} n_i \left(\left[\mathcal{M}_i^2(\phi, S, T) \right]^{3/2} - \left[\mathcal{M}_i^2(\phi, S) \right]^{3/2} \right). \tag{3.21}$$

It gives the last term in Eq. 3.19 a temperature dependence which is crucial for the analysis of the phase transition in the SM.

In the SM, this cubic term is the only source to induce a thermal barrier between a symmetric minimum and a symmetry-broken minimum in the effective potential. It was because that all the other terms in SM Higgs sector are quadratic or quartic, which can't create such degenerate minima in one-dimensional space. However, in our model, as shown later, the new dimension in the scalar space greatly enriches the possibility, and hence the ring diagram contribution is much less important.

[2]There are subtleties about the sub-dominant contributions [52].

The total effective potential at finite temperature is the sum of the above terms

$$V_{\text{eff}}(\phi, S, T) = V_{\text{CW}}^{\text{on-shell}}(\phi, S) + V_{\text{thermal}}(\phi, S, T) + V_{\text{ring}}(\phi, S, T). \tag{3.22}$$

For part of the field space, the field-dependent masses of the scalars and the Goldstone bosons can be negative, and the non-convexity of the potential would induce an imagenery part that indicates a vacuum decay rate per unit volume. However, the real part can still be interpreted as the expectation value of the energy density. Therefore we only take the real part of the potential to do the analysis.

3.2.2 Approximations

Before we do numerical scan over the parameter space, we want to get a flavor of how the potential behaves when the temperature varies, and some general features of a first order phase transition.

First, we try to examine the potential using high temperature approximation. This approximation is actually not quite valid at the phase transition temperature, which is usually not very high. Using the high temperature expression Eq 3.19, we get from Eq 3.22

$$\begin{aligned} V_{\text{eff}}(\phi, s, T) \simeq V_{\text{tree}} &+ \frac{T}{12\pi} \sum_{i=\text{B}} n_i \left[\mathcal{M}_i^2(\phi, S, T)\right]^{3/2} + \sum_{i=\text{B,F}} \frac{|n_i|}{24(1+\delta_{i\text{F}})} \mathcal{M}_i^2(\phi, S) T^2 \\ &- \sum_{i=\text{B,F}} \frac{n_i}{64\pi^2} \left(\mathcal{M}_i^4(\phi, S) \log \frac{\mathcal{M}_i^2(v, u)}{a_i' T^2} - 2\mathcal{M}_i^2(v, u) \mathcal{M}_i^2(\phi, S) \right). \end{aligned} \tag{3.23}$$

The second line with loop factor can be neglected as further approximation, while the $\log T$ dependence can be absorbed into the running couplings which also don't have large effect within the energy range of interest. The T^2 term is the main effect from thermal correction, and the $|n_i|$ factor means that both bosonic and fermionic fields contribute positively to the mass squared functions. The subleading $T^{3/2}$ term is hard to deal with, because it's the only place where cubic term can appear in the SM, so naive expansion in high temperature would hide the phase transition feature of the potential.

We argue that with non-$\mathbb{Z}_2$ extended field space $\{\phi, S\}$, since we have tree level cubic term, the cubic term from ring diagram will be subleading in general. Thus further approximation can be taken to expand the ring diagram term in high temperature, and the leading feature of first order phase transition could still be studied. Hence after the expansion we get

$$V_{\text{eff}}(\phi, S, T) \simeq V_0 + \sum_{i=\text{B}} \frac{n_i c_i}{8\pi} m_i^2(\phi, S) T^2 + \sum_{i=\text{B,F}} \frac{|n_i|}{24(1+\delta_{i\text{F}})} m_i^2(\phi, S) T^2 + \delta(T), \tag{3.24}$$

where V_0 is the zero-temperature potential, $\delta(T)$ is the T^4 order vacuum-independent energy density term. c_i are coefficients in the thermal masses Π_i. Assuming $c_i \sim 1$, we see that the ring contribution is roughly at the same order as the original T^2 contribution. Finally we get the approximated finite-temperature potential

$$V_{\text{eff}}(\phi, S, T) \simeq V_0 + T^2 \left[AS + B\phi^2 + CS^2 \right], \tag{3.25}$$

where

$$
\begin{aligned}
A &= \frac{1}{12}\left[4\mu_{S\phi} + 2\mu_3\right], \\
B &= \frac{1}{12}\left[(6\lambda_H + \lambda_{SH}/2) + \frac{1}{4}(3g_2^2 + g_1^2) + \frac{2}{3}(y_t^2 + y_T^2)),\right], \\
C &= \frac{1}{12}\left[(3\lambda_S + 2\lambda_{SH}) - 3y_M^2\right].
\end{aligned}
\tag{3.26}
$$

One thing obvious from this form of potential is the high temperature field values. ϕ must be in the symmetric phase $\phi_{T\to\infty} = 0$ due to the dominant positive quadratic term, and $S_{T\to\infty} \sim -\frac{A}{2C}$ in terms of high temperature values of the couplings.

Note that there is no leading order modifications of the cubic potential term. If we neglect subleading corrections, we can roughly estimate the first order phase transition in the polar coordinate in the field space at the transition temperature T_c

$$
\rho = \sqrt{\phi^2 + (s - u_s)^2}, \quad \tan\alpha = \frac{s - u_s}{\phi}, \tag{3.27}
$$

where u_s is the VEV of S at the symmetric phase. Suppose the symmetry-broken phase is at v_c, u_b, which in polar coordinates is $(\bar{\rho}, \bar{\alpha})$, so that

$$
\tan\bar{\alpha} = \frac{u_b - u_s}{v_c} \tag{3.28}
$$

Along this direction, the potential should have degenerate minima, which takes the general form

$$
V_{\text{eff}}(\rho, T) \simeq \frac{1}{2}D(T^2 - T_0^2)\rho^2 + \mathcal{E}\rho^3 + \frac{\lambda}{4}\rho^4 = \frac{\lambda}{4}\rho^2(\rho - \bar{\rho}^2). \tag{3.29}
$$

with coefficients D, T_0, $\mathcal{E}$ and λ depending on coefficients in Eq 3.25 and the angle $\bar{\alpha}$. The broken phase is solved as

$$\bar{\rho} = -\frac{2\mathcal{E}}{\lambda}, \quad T_c^2 = T_0^2 + \frac{8\mathcal{E}^2}{\lambda D} \tag{3.30}$$

with our interesting parameter given by $v_c = \bar{\rho}\cos\bar{\alpha}$. Note that only negative $\mathcal{E}$ could lead to degenerate phases. The parameters are

$$\begin{aligned} D &= 2(B+C), \\ \mathcal{E} &= s_\alpha \left[(\mu_{SH} + \lambda_{SH} u_s) c_\alpha^2/2 + (\mu_3/3 + \lambda_S u_s) s_\alpha^2\right], \\ \lambda &= \lambda_H c_\alpha^4 + \lambda_S s_\alpha^4 + \lambda_{SH} c_\alpha^2 s_\alpha^2, \end{aligned} \tag{3.31}$$

with $s_\alpha \equiv \sin\bar{\alpha}$, $c_\alpha \equiv \cos\bar{\alpha}$. In the next section, we will use these expressions of the coefficients to analyse the parameter preferences in light of the strong first order phase transition.

3.2.3 Numerical Scan

Once we obtain the full effective potential, we could investigate how the vacuum state evolves with temperature. At each temperature, we find the true vacuum by looking for the global minimum of the potential in the (ϕ, S) field space. It is known that at zero temperature, the global minimum of the scalar potential is at (v_0, u_0), with $v_0 = 246$ GeV and u_0 as an input parameter. After we turn on and increase the temperature, we track the position of the global minimum, seeking the sign of a phase transition. In the context of effective potential, the fields are defined to be the first derivative of the free energy with respect to the corresponding particle source, and thus

acts like an order parameter of the phase transition. If the transition of the field values between the two phases is continuous, it is a second order phase transition. Otherwise, if there is a discontinuous variation of the fields, it is a first order phase transition. The first order phase transition proceeds by bubble nucleation of the broken phase at around the critical temperature. The bubbles grow and coalesce, and finally turn the whole universe into the broken phase.

As discussed in the introduction, to have successful baryogenesis, it is essential to have a strong enough first order phase transition, so that $E_{\rm sph}(T_c)/T_c \geq 45$ inside the bubbles. It has been shown in literature [61] that for a singlet extended model the sphaleron energy is approximately proportional to the ϕ vev: $E_{\rm sph}(T_c) \propto v_c$. Moreoever, the bubble expansion and wall velocity in the singlet extended model have been discussed in Ref. [77]. In our model there is a similar scalar sector. Thus the discussions about the bubble expansion and sphaleron process in literatures also applied to our model. Therefore, similar to singlet extended model, we add the following criterion to our scan to pick out the events with strong FOPT:

$$\xi \equiv \frac{v_c}{T_c} \geq 1. \tag{3.32}$$

To determine the parameter region in which the strong first order phase transition could happen, we perform a random scan over the parameter space. The procedure is the following. We have quite a few independent parameters

$$\lambda_S, \quad \lambda_{SH}, \quad \mu_3, \quad \mu_{SH}, \quad M, \quad y_T, \quad y_M, \tag{3.33}$$

in addition to the singlet vev u_0 in the zero temperature. M is the dirac mass for the vector-like fermion ψ. The parameters λ_H and y_t are determined by the Higgs mass and the top quark mass that are already known. We choose the input parameters from the ranges

$$\begin{aligned} &|\lambda_{s\phi}| \leq 1.5,\ 0 < \lambda_s \leq 2,\ |y_T| \leq 1.5,\ |y_s| \leq 1.5, \\ &|u_0| \leq 600,\ |\mu_3| \leq 800,\ |\mu_{s\phi}| \leq 1000,\ 0 \leq M \leq 1200. \end{aligned} \tag{3.34}$$

Given the input parameters, the full effective potential in the field space is calculated. Then for each temperature, we utilize the MINUIT subroutine [78] to find the global minimum of the effective potential. As the temperature increases, we track the change of the global minimum at each step in our numerical scan. Additional care should be taken: if the minimum moves to very large field values, it may indicates vacuum instability. If the global minimum becomes the symmetric one $(0, \langle s \rangle)$ at certain temperature, we perform a fine scan near the temperature until we find the critical temperature T_c and the corresponding vevs (v_c, u_b) in the broken phase. After obtaining the T_c and v_c, we use the washout condition to pick out the strong first order phase transition, eliminating the data points that has $\xi < 1$. We randomly scan 10^6 parameter points, among which 25818 parameter points pass all the requirements. Figure 3.1 shows the distribution of the successive data points in the $T_c - v_c$ plane. From the figure we notice that for the parameter region we scanned, the critical temperature is typically less than 200 GeV, while v_c is smaller than its zero-temperature value $v_c > v_0 = 246$ GeV. The higher the critical temperature is, the smaller the ϕ VEV gets to before the transition,

and this correlation is clearly shown in the figure. Furthermore, this range of critical temperature is quite safe from the bound of the CP violation strength that we discussed in Sec.3.1.

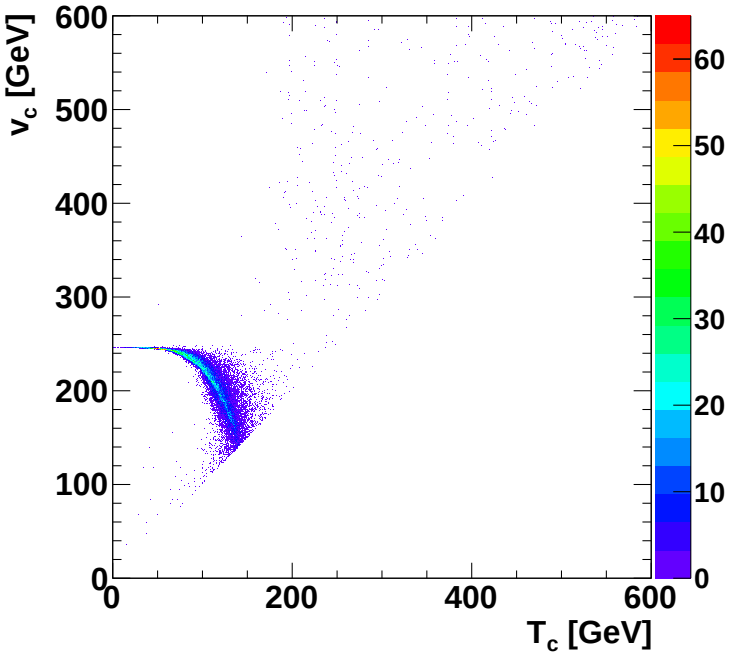

Figure 3.1: The allowed value of the critical temperature T_c versus the ϕ vev v_c at the critical temperature from a random scan over the parameter space.

3.3 Analysis of Results

I will list a few important feature from the scan results. For more detailed analysis please refer to [2].

3.3.1 Transition Pattern

We are interested in the evolution of ground states during the cooling of the universe, especially around the phase transition temperature. The easiest way to investigate this is to look at the field values at some key points, i.e. the zero-temperature values (v_0, u_0), slightly lower than critical temperature (broken phase) values (v_c, u_b) and slightly higher than critical temperature (symmetric phase) $(0, u_s)$. For field ϕ, the only unknown v_c is already shown in Fig. 3.1. Thus we show the correlation between (u_s, u_b) and (u_b, u_0) in Fig. 3.2

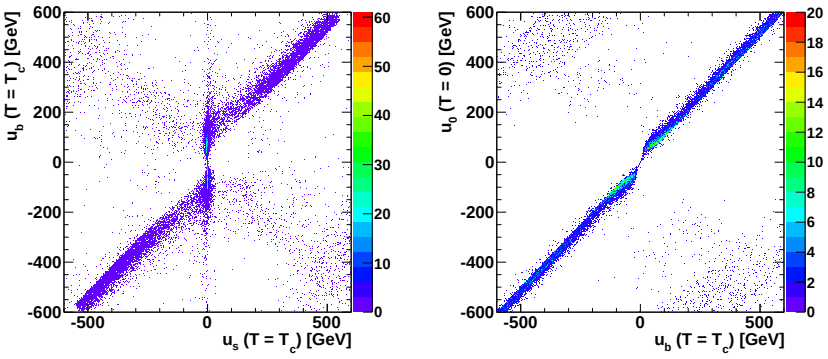

Figure 3.2: The allowed value of the contour (u_s, u_b) (left) and (u_b, u_0) (right) from a random scan over the parameter space.

From the (u_s, u_b) histogram, it is easy to distinguish several distinct patterns:

- Pattern I: $u_s \sim 0$. It corresponds to the bright greenish line-shape region at the center and its surrounding blue region. Surprisingly, although

there is no $\mathbb{Z}_2$ symmetry for the field S, it is still preferred to take 0 value right after the phase transition, even though its high temperature limit $-\frac{A}{2C}$ we found earlier is obviously nonzero. It is due to the fact that we didn't include a linear term in S in the Lagrangian, which sets the definition of S with respect to shifting. This vanishing linear term guarantees that there is one extremum for S at $S = 0$. In the case when $V_{\text{eff}}(0, S)$ only has one extremum, i.e. $S = 0$, it must be a minimum, and it is the symmetric phase in this pattern. The case when $V_{\text{eff}}(0, S)$ has three extrema will be discussed in the next pattern. If we look at the parameter $\mathcal{E}$ in this case, since $u_s \sim 0$, it has very simple form

$$\mathcal{E}_I = \frac{1}{2}\mu_{SH} s_\alpha c_\alpha^2 \tag{3.35}$$

Thus to get stronger FOPT, large μ_{SH} is prefered, and s_α would have opposite sign than μ_{SH}. This preference can be understood because μ_{SH} is a tree-level cubic term, which is essential for getting FOPT. But the key point here is that μ_3 does not matter in this pattern – from the scan, we found that μ_3 prefers small values. In Fig. 3.3 we show the histogram of the cubic couplings for $u_0 > 0$, while the case with $u_0 < 0$ should be symmetric with this distribution.

- Pattern II: $u_s \neq 0$. It is usually the case when there are three extrema for $V_{\text{eff}}(0, S)$. According to the way we scan the parameter space, it is easy to see that it is most likely to have a positive and a negative extrema besides the $S = 0$ one, and thus the $S = 0$ is a local maxi-

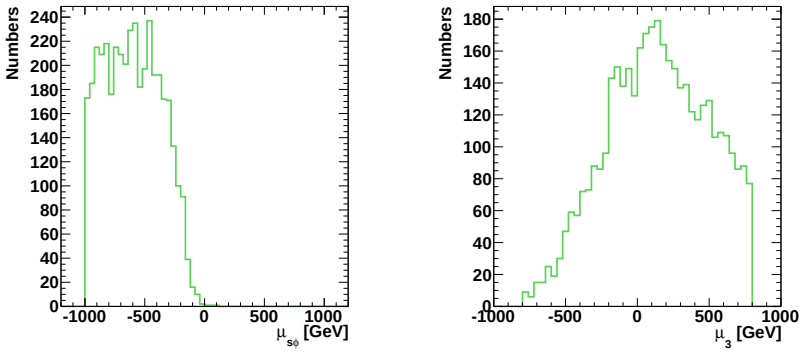

Figure 3.3: In the pattern I with $u_0 > 0$, the allowed values of the cubic couplings $\mu_{s\phi}$, μ_3 are shown.

mum. Therefore, without large changes due to temperature, we would expect the symmetric phase to appear at an extremum other than $S \sim 0$, thus distinguished from pattern I. In this pattern, there are very strong correlation between u_0, u_b and u_s, as indicated from Fig. 3.2.

Aside from the same preference of large μ_{SH} in pattern I, it turns out that a μ_3 with opposite sign than u_0 is strongly prefered. It is because u_s, being correlated with u_0 and having the same sign, is a lower minimum than the other minimum with opposite sign, which is controlled by the sign of μ_3. In Fig. 3.4 we show the histogram of the cubic couplings for $u_0 > 0$.

- Pattern III. This pattern includes all the other cases, represented by the points scattered away from the mainstream in Fig.3.1 and Fig.3.2. The number of events in this pattern is relatively few. These cases include unusual situations when transition happens between uncorrelated u val-

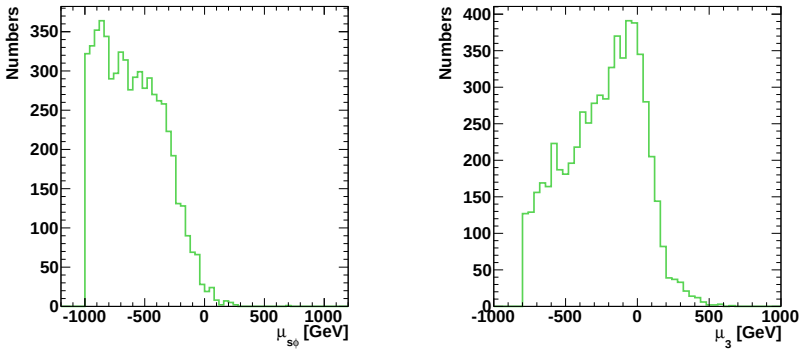

Figure 3.4: In the pattern II with $u_0 > 0$, the allowed values of the model parameters $\mu_{s\phi}$, μ_3 are shown.

ues (inter-branch transition) or there are multiple transitions processes (multi-step transitions). As they seem to have less probability, and untypical parameters may be allowed, we are not interested in them here. For more details please refer to [2].

3.3.2 Prefered Physical Parameters and Constraints

We would also like to see what region of physical parameters are prefered by the electroweak FOPT. In Figure 3.5, we present the two dimensional contours of the physical parameters (m_S, s_α) in the scalar sector, and those of $(m_T, \sin\theta)$ in the fermion sector. It is shown that the scalar with its mass around 500 - 1000 GeV and a medium mixing angle is favored. We recognized the feature that small mixing angle are disfavored, as expected from the fact that the scalar needs to couple with the Higgs boson to render strong first order phase transition. This favored region is compatible with that allowed

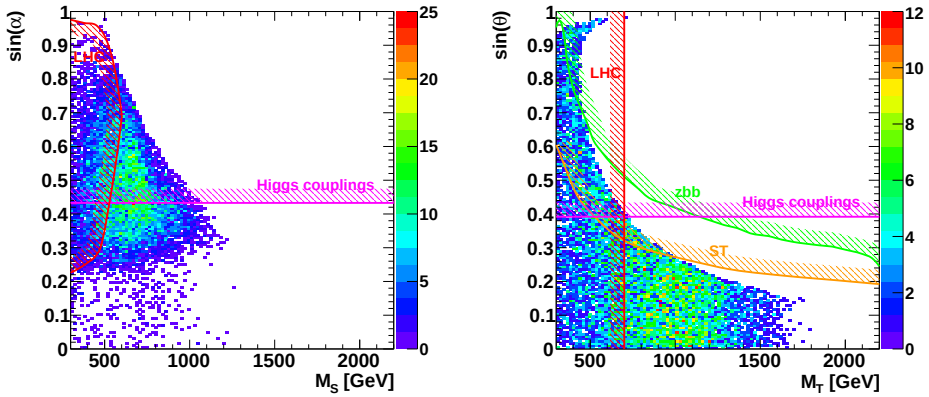

Figure 3.5: The allowed parameter contour $(m_S, \sin\varphi)$ (left) and $(m_T, \sin\theta_L)$ (right) in light of the strong first order phase transition. The constraints from the S, T parameters, Higgs coupling measurements, and direct LHC searches are shown as the exclusion lines.

by vacuum stability criteria [1]. Unlike the scalar mixing angle, the fermionic mixing angle can be very small, which indicates the decoupling between the new fermion and the phase transition criteria.

The curves with different colors represent various constraints from the experiments, as discussed in Chapter 2. We note that although the large mixing in fermion sector is completely ruled out by LHC search, the most populated region is still alive. Ths scalar sector, however, is not so lucky, as the strong preference on large mixing angle (stronger than the stability constraint studied in Chapter 2) is significantly constrained by the experiments.

3.4 Conclusions

We investigated the necessary conditions to realize the electroweak baryogenesis in a SAVF model. In the fermion sector, the extended CKM matrix provides additional sources of the CP violation effects, parametrized by Jarlskog-like invariant. We found that the CP violation rate is greatly enhanced by the heavy mass of the new fermion. With the flavor constraints on the extended 4×3 CKM matrix considered, we estimated the CP violation strength, which turns out to be adequate for the baryon number asymmetry.

We focused on the one-loop, finite-temperature effective potential in our model and its implications on the electroweak phase transition. Unlike the case of the SM, the new scalar extends the field space in which the phase transition occurs. In the two-dimensional field space, we have more possible ways of constructing barriers between minima. Specifically, the cubic term essetial for the FOPT can be generated at tree level, greatly enhancing the strength of the phase transition.

We performed a parameter scan over the 8 independent model parameters, and obtained the allowed parameter region which could have strong first order phase transition. According to the different regions in the (u_b, u_s) contour at the critical temperature, transition patterns are classified into different patterns. Large trilinear mass term $\mu_{s\phi}$ is usually favored because the width of the barrier is strongly related to it.

Finally we combine the constraints from strong first order phase transi-

tion and the experimental limits on the S, T parameters, Higgs coupling measurements, and direct LHC searches, in order to examine the allowed region for physical parameters. We found that there is still a significant amount of parameter region for the fermion mass and couplings to satisfy all the constraints, and have adequate CP violation strength to realize the baryon asymmetry at the same time. The new scalar with mass around 500 - 1100 GeV and mixing angle $\sin\varphi$ around $0.25 - 0.42$ are still allowed and favored by the strong first order phase transition.

We expect that the future Higgs data could explore the parameter region on the $(m_S, \sin\varphi)$ contour. We should also be able to explore the scalar trilinear coupling $\lambda_{s\phi}$ and λ_ϕ at the high luminosity LHC. If the trilinear couplings are enhanced compared to the SM Higgs self-coupling, the Higgs pair production cross section should be larger than the SM value. Through the Higgs pair production process $pp \to h/S \to hh$, we could extract out the trilinear couplings from the production cross section measurements.

3.5 Appendix: Details of Coleman-Weinberg Potential

In effective potential, the particles running in the loop are the particles in the model with the following degrees of freedom in the Landau gauge:

$$n_W = 6,\ n_Z = 3,\ n_\pi = 3,\ n_h = n_S = 1,\ n_t = -12,\ n_T = -12. \tag{3.36}$$

The field-dependent masses of the top quark, gauge bosons and Goldstone bosons at zero temperature are given by

$$\begin{aligned} m_W^2(\phi) &= \frac{g^2}{4}\phi^2,\ m_Z^2(\phi) = \frac{g^2+g'^2}{4}\phi^2, \\ m_\pi^2(\phi,s) &= \lambda_\phi\phi^2 - \mu_\phi^2 + \frac{1}{2}\lambda_{s\phi}s^2 + \mu_{s\phi}s. \end{aligned} \tag{3.37}$$

The field-dependent masses of the scalars h and S are obtained as

$$m_{h,S}^2(\phi,s) = \frac{1}{2}\left(m_{\phi\phi}^2(\phi,s) + m_{ss}^2(\phi,s)\right) \mp \frac{1}{2}\sqrt{\left(m_{\phi\phi}^2(\phi,s) - m_{ss}^2(\phi,s)\right)^2 + 4m_{s\phi}^4(\phi,s)}, \tag{3.38}$$

where the field-dependent quantities are

$$\begin{aligned} m_{\phi\phi}^2(\phi,s) &= 3\lambda_\phi\phi^2 - \mu_\phi^2 + \frac{\lambda_{s\phi}}{2}s^2 + \mu_{s\phi}s, \\ m_{s\phi}^2(\phi,s) &= m_{\phi s}^2(\phi,s) = (\lambda_{s\phi}s + \mu_{s\phi})\phi, \\ m_{ss}^2(\phi,s) &= 3\lambda_s s^2 + 2\mu_3 s - \mu_s^2 + \frac{\lambda_{s\phi}}{2}\phi^2. \end{aligned} \tag{3.39}$$

The field-dependent masses of the top quark and heavy vector-like top quark T are obtained as

$$m_{t,T}^2(\phi,s) = \frac{1}{2}\left(m_{tt}^2(\phi,s) + m_{TT}^2(\phi,s)\right) \mp \frac{1}{2}\sqrt{\left(m_{tt}^2(\phi,s) - m_{TT}^2(\phi,s)\right)^2 + 4m_{tT}^4(\phi,s)}, \tag{3.40}$$

where the field-dependent quantities are

$$\begin{aligned} m_{tt}^2(\phi, s) &= \frac{1}{2}(y_t^2 + y'^2)\phi^2, \\ m_{tT}^2(\phi, s) &= m_{Tt}^2(\phi, s) = \frac{1}{\sqrt{2}} y'\phi(y_s s + M), \\ m_{TT}^2(\phi, s) &= (y_s s + M)^2. \end{aligned} \tag{3.41}$$

The finite-temperature potential needs to be corrected by the thermal field-dependent masses. The thermal field-dependent masses is calculated by adding the Debye masses, calculated from the the quadratically divergent bubbles and Daisy resummation. This leads to a shift of the bosonic field-dependent masses $m_i^2(\phi, s)$ to the thermal field-dependent masses (Debye masses)

$$m_i^2(\phi, s, T) \equiv m_i^2(\phi, s) + \Pi_i(\phi, s, T), \tag{3.42}$$

where $\Pi_i(\phi, s, T)$ is the self-energy of the bosonic field i in the IR limit. In particular, the longitudinal and transversal polarizations of the gauge bosons have to be taken into account separately: only the longitudinal components get a thermal mass correction and the transversal ones will not. Since the ring diagrams will only contribute significantly at high-temperature, only the zero-mode of the Matsubara frequency behave as a massless degree of freedom and generate IR-divergences at high-temperature, while other modes lead to sub-dominant contributions. For the SM bosonic contributions, the gauge boson thermal self energy is

$$m_{\rm V}^2(h, s, T) = m_{\rm V}^2(h, s) + \Pi_{\rm V}, \tag{3.43}$$

where

$$m_{\rm V}^2 = \phi^2 \begin{pmatrix} \frac{g^2}{4} & 0 & 0 & 0 \\ 0 & \frac{g^2}{4} & 0 & 0 \\ 0 & 0 & \frac{g^2}{4} & -\frac{gg'}{4} \\ 0 & 0 & -\frac{gg'}{4} & \frac{g'^2}{4} \end{pmatrix} \tag{3.44}$$

and

$$\Pi_{\rm V} = \text{diag}\left[\frac{11}{6}g^2T^2,\ \frac{11}{6}g^2T^2,\ \frac{11}{6}g^2T^2,\ \frac{11}{6}g'^2T^2\right] \tag{3.45}$$

The Goldstone boson is

$$\Pi_\pi = \left(\frac{3}{16}g^2 + \frac{1}{16}g'^2 + \frac{\lambda_{_H}}{2} + \frac{y_t}{4} + \frac{\lambda_{_{HS}}}{3}\right)T^2 \tag{3.46}$$

For the new scalar bosons,

$$\mathcal{M}^2(\phi, s, T) = \mathcal{M}^2(\phi, s) + \begin{pmatrix} c_\phi & 0 \\ 0 & c_s \end{pmatrix} T^2, \tag{3.47}$$

where

$$\begin{aligned} c_\phi &= \frac{\lambda_\phi}{2} + \frac{\lambda_{s\phi}}{24} + \frac{3g^2 + g^{'2}}{16} + \frac{y_t^2}{4}, \\ c_s &= \frac{\lambda_s}{4} + \frac{\lambda_{s\phi}}{6}. \end{aligned} \tag{3.48}$$

After diagonalization, we obtain the Deybe squared mass $m_{h,S}(\phi, s, T)$. For the SM bosonic particles, we obtain

$$\begin{aligned} \Pi_{W_{_L}} &= \frac{11}{6}g^2T^2, \quad \Pi_{W_{_T}} = 0, \\ \Pi_{Z_{_L}} &= \frac{11}{6}(g^2 + g^{'2})T^2, \quad \Pi_{Z_{_T}} = 0, \\ \Pi_\pi &= c_\phi T^2. \end{aligned} \tag{3.49}$$

Chapter 4

Holographic Complexity in Non-commutative Field Theory

In the past several years, there has been a growing interest in the topic of "holographic complexity". This interest was originally motivated by the late time growth of the wormhole size for two-sided black holes, which seems to have no correspondence in the boundary state which is in thermal equilibrium. It was then conjectured that such a phenomenon should be related to the quantum complexity of the boundary state [13], and this conjecture was strengthened by the study of quantum chaos, namely the "switchback effect" [14, 79]. There have since been several conjectures as to the exact bulk quantity dual to the complexity on the boundary, all tied to the phenomenon of the expanding wormholes in two-sided black holes. The first proposal, "complexity = volume" (CV) [13], was that the complexity of state on a boundary time slice σ is given by

$$\mathcal{C}_V(\sigma) \sim \frac{1}{G\ell} \max\{\mathrm{Vol}(\Sigma)|\partial\Sigma = \sigma\}, \tag{4.1}$$

This chapter is based on my previous work [15] with J. Couch, *et. al.*, in which we had equal contributions.

where Σ is a bulk time slice whose boundary is exactly σ. The obvious problem with this proposal is the ambiguous scale ℓ appearing in the formula, which proves to be varied in different cases. An improved version, "complexity = action" (CA) [80, 81], was then proposed as

$$\mathcal{C}_A(\sigma) \sim I_{\text{WDW}}(\sigma), \tag{4.2}$$

where I_{WDW} is the gravitational action evaluated on the Wheeler-DeWitt (WDW) patch. WDW is defined to be the set of points in the bulk that are space-like separated from the given boundary time slice σ, which is bounded by null hypersurfaces $\mathcal{W}^{\pm}$ generated by null normal vectors on σ towards the bulk. Another closely related conjecture was later proposed in [82], namely that the complexity is dual to the space-time volume of a WDW patch.

Unfortunately, there is little that we know about the concept of quantum complexity in the boundary field theory. The basic definition involves a reference state $|\psi_0\rangle$, a set of quantum gates $G = \{g_i\}$, and a tolerance parameter ϵ. The complexity of a quantum state $|\psi\rangle$ is the minimum number of gates one needs to make up a quantum circuit $Q = \prod_{i=1}^{\mathcal{C}} g_i$ so that $d_f(Q|\psi_0\rangle, |\psi\rangle) < \epsilon$. One can also define the complexity of a unitary operator U to be the minimum number of gates one needs to make up a quantum circuit Q_U so that $||Q_U - U|| < \epsilon$. [1] The holographic complexity is supposed to be

[1] $d_f(\ ,\ )$ is the Fubini-Study metric for quantum state $d_f(\alpha, \beta) = \arccos\sqrt{\frac{|\langle\alpha|\beta\rangle|^2}{\langle\alpha|\alpha\rangle\langle\beta|\beta\rangle}}$. The norm $||A||$ for operators can be defined as the square root of the spectral radius $\rho(A^\dagger A)$, which is the supremum of the eigenvalues of $A^\dagger A$.

the state complexity, while we also use the operator complexity to analyze the characteristic behavior in section 4.2. Even with these definitions, the task of actually computing the relative complexity of two states is notoriously difficult. What is more, in the definition one has to make several choices, and where these choices appear in the holographic prescription is as of yet unclear. It is also a puzzle how one goes from the discretum of quantum circuits to a supposedly continuous quantum field theory. There has been considerable effort defining complexity in the quantum field theory [83–88], however they are weakly related to the holographic complexity at this point. Therefore, what we are interested in is to utilize our intuitions from quantum mechanics to conjecture some constraints on complexity in general. These constraints are to be tested for both the boundary theory and the holographic theory.

Among the constraints which people have considered is the Lloyd bound [89]. This bound was derived from the Margolus-Levitin theorem [90] under the assumption that each gate will evolve a generic state into an orthogonal state. It states that the time rate change of complexity[2] is constrained by the energy:

$$\dot{\mathcal{C}} \leq \frac{2M}{\pi}, \tag{4.3}$$

where M is the energy of the system. In [80, 81] it was conjectured that neutral black holes should saturate this bound, and this assumption was made

[2]We also refer to the time rate change of complexity as the "complexification" rate, which should be considered synonymous as they appear in this paper.

in order to set the constant of proportionality between complexity and action. This conjecture originated from the fast scrambling nature of black holes and the related idea that black holes are the fastest possible quantum computers. However, one finds that for neutral black holes, the Lloyd bound is saturated from above [91], which makes the conjecture somewhat suspicious. One can also argue that the Lloyd bound is not an exact bound because the assumption is based on is highly unrealistic. In fact, whether this assumption applies in the case of holographic complexity has recently been questioned in [92].

In light of these difficulties with the Lloyd bound, it is interesting to test the holographic complexity conjectures[3] against additional pieces of intuition in novel contexts. One context which might reasonably provide a testbed is the noncommutative field theories. The study of such theories has a long history and has produced many profound results, see for example [93–98]. One feature of noncommutative field theory which is suggestive of interesting behavior is that it adds a degree of non-locality, which has been shown to lead to interesting effects, e.g. an increase relative to the commutative case in the dissipation rate of scalar modes [99]. Indeed, the holographic entanglement entropy in this context has already been studied in, for example, [100, 101], where non-trivial behavior was found in the limit where the Moyal scale is much larger than the thermal scale. The geometry was obtained in a string theory context by turning on the NS-NS B fields on Dp branes. The non-vanishing B

[3]In this paper we will consider only complexity = action, and discussion of the complexity = volume and complexity = spacetime volume conjectures are left for future work.

field then induces Dirichlet boundary condition for open strings, and non-zero commutator of the end point coordinates [93]. After decoupling the closed strings, the Dp brane worldvolume becomes a noncommutative space. It was shown that in such setup, although space is coarse-grained by the Moyal scale, which might indicate a reduction in the number of degrees of freedom, it turns out that all thermodynamical quantities are unchanged [94, 96]. This can be understood by looking at the thermal boundary state in the large N limit, which consists of only planar diagrams without external legs. Such diagrams are insensitive to the non-commutativity of the spacetime [102]. It thus provides a perfect arena for testing quantum complexity, whose main characteristic is that it is more than thermodynamics. If the holographic complexity can see the difference caused by non-commutativity, it is a sign that we are on the right track.

4.1 Holographic Complexity of 4d $\mathcal{N} = 4$ NCSYM

4.1.1 The holographic dual to noncommutative SYM

We consider the noncommutative field theory widely studied in the context of string theory. It was shown that the non-vanishing NS-NS B field will induce noncommutative space on the D brane that decouples from the closed string excitations [93]. The way to turn on the B field is to perform a T duality, in D3 brane for instance, along x_3 direction, assuming the x_2, x_3 are compatified on a torus. The torus becomes tilted after the T duality, which indicates a D2 brane smearing along x_3 direction. Then one performs another

T duality along x_3, to get the following solution ([94, 95]):

$$\begin{aligned} ds^2 &= \alpha' \Bigg[\left(\frac{r}{R}\right)^2 \left(-f(r)dt^2 + dx_1^2 + h(r)(dx_2^2 + dx_3^2)\right) \\ &\quad + \left(\frac{R}{r}\right)^2 \left(\frac{dr^2}{f(r)} + r^2 d\Omega_5^2\right) \Bigg], \\ f(r) &= 1 - \left(\frac{r_H}{r}\right)^4, \quad h(r) = \frac{1}{1 + a^4 r^4}, \end{aligned} \tag{4.4}$$

with non-trivial fields

$$\begin{aligned} e^{2\Phi} &= \hat{g}_s^2 h(r), \\ B_{23} &= B_\infty (1 - h(r)), \quad B_\infty = -\frac{\alpha'}{a^2 R^2}, \\ C_{01} &= -\frac{\alpha' a^2 r^4}{\hat{g}_s R^2}, \quad F_{0123r} = \frac{4\alpha'^2 r^3}{\hat{g}_s R^4} h(r). \end{aligned} \tag{4.5}$$

The $\{t, x_1, x_2, x_3\}$ are the D3 brane coordinates, while $\{x_2, x_3\}$ are non-commuting with Moyal algebra

$$[x_2, x_3] = i a^2. \tag{4.6}$$

The radius coordinate r has units of inverse length[4], and a is the Moyal scale with units of length. r_H denotes the location of the event horizon, and $\hat{g}_s$ denotes the closed string coupling, which is related to the S^5 radius as $R^4 = \hat{g}_s N$.

Note that the geometry becomes degenerate at $r \to \infty$; thus we have to put the boundary theory on some cutoff surface $r_b < \infty$. It was shown that

[4]In the literature, the coordinate denoted here by 'r' is typically denoted 'u' in order to emphasize that it does not have dimensions of length. We have however chosen to denote it by 'r' to avoid confusion with the Eddington-Finkelstein like null coordinate.

this natural cutoff plays an important role in the divergent structure of entanglement entropy [100]. However, as will be explained later, our computation is cutoff independent; therefore we don't need to worry about it.

As explained in [94], all the thermodynamic quantities of this solution are the same as in the commutative case. In particular, the temperature and entropy is independent of a, given by

$$E = \frac{3r_H^4\Omega_5 V_3}{(2\pi)^7\hat{g}_s^2}, \quad T = \frac{r_H}{\pi R^2}, \quad S = \frac{4\pi R^2 r_H^3\Omega_5 V_3}{(2\pi)^7\hat{g}_s^2} \tag{4.7}$$

It is then interesting to ask whether the complexity is affected by the non-commutativity because complexity is fine-grained information that knows more than thermodynamics.

We adopt the Complexity equals Action (CA) approach to compute the holographic complexity of the boundary state. It involves evaluating the action in a bulk subregion, called the Wheeler-deWitt (WDW) patch. Recent work on evaluating gravitational action [103] provided a toolkit that deals with null boundary contributions in the context of Einstein gravity. Hence we are interested in the Einstein frame action of type IIB supergravity:

$$ds_E^2 = \exp(-\Phi/2)ds^2, \tag{4.8}$$

$$\begin{aligned} 2\kappa^2 S_E = &\int d^{10}x\sqrt{-g_E}\left[\mathcal{R} - \frac{1}{2}|d\Phi|^2 - \frac{1}{2}e^{-\Phi}|dB|^2 - \frac{1}{2}e^{\Phi}|F_3|^2 - \frac{1}{4}|\tilde{F}_5|^2\right] \\ &- \frac{1}{2}\int C_4 \wedge dB \wedge F_3, \end{aligned} \tag{4.9}$$

where the notation $|F_p|^2 = \frac{1}{p!}F_{\mu_1\ldots\mu_p}F^{\mu_1\ldots\mu_p}$ is understood. One should keep in mind that the 5-form $\tilde{F}_5$ is self dual while evaluating this action. This

requirement actually always makes the term $|\tilde{F}_5|^2 = 0$[5].

4.1.2 Wheeler-DeWitt Patch Action

Regarding representing the boundary state, the WDW patch differs from the entanglement wedge at two points: first, it specifies a specific time slice on the boundary, instead of a covariant causal diamond; second, it probes behind the horizon, which is supposed to contain information beyond thermodynamics. It was conjectured in [80, 81] that the action evaluated in the WDW patch is dual to the complexity of the boundary state, which is referred to as CA duality/proposal. In our noncommutative geometry setup, we will be interested in the WDW patch for the two-sided black hole, which intersects the left boundary at time t_L, and the right boundary at time t_R. According to CA duality, the action evaluated on such a patch will compute the relative complexity of the quantum state of the boundary CFT living on the (t_L, t_R) slice as

$$\mathcal{C}(t_L, t_R) = kS_{WDW}, \tag{4.10}$$

with the coefficient set to $k = (\pi\hbar)^{-1}$ by the assumption that AdS-Schwartzchild black hole saturates the Lloyd bound. The complexity computed this way is

[5]We point it out that due to the famous subtlety about type IIB action, that the self-duality condition should be imposed by hand, the treatment we use for the action is only plausible. There are other ways to impose self-duality, for example the PST formulation, but the action computation and the holography there will be subtle.

cutoff dependent, but its time derivative

$$\dot{\mathcal{C}}(t_L, t_R) := \frac{d}{dt_L}\mathcal{C}(t_L, t_R), \tag{4.11}$$

in which we are interested, is cutoff independent. Without loss of generality, we make a choice to differentiate with respect to the left time instead of the right time, as the geometry should be symmetric between left and right.

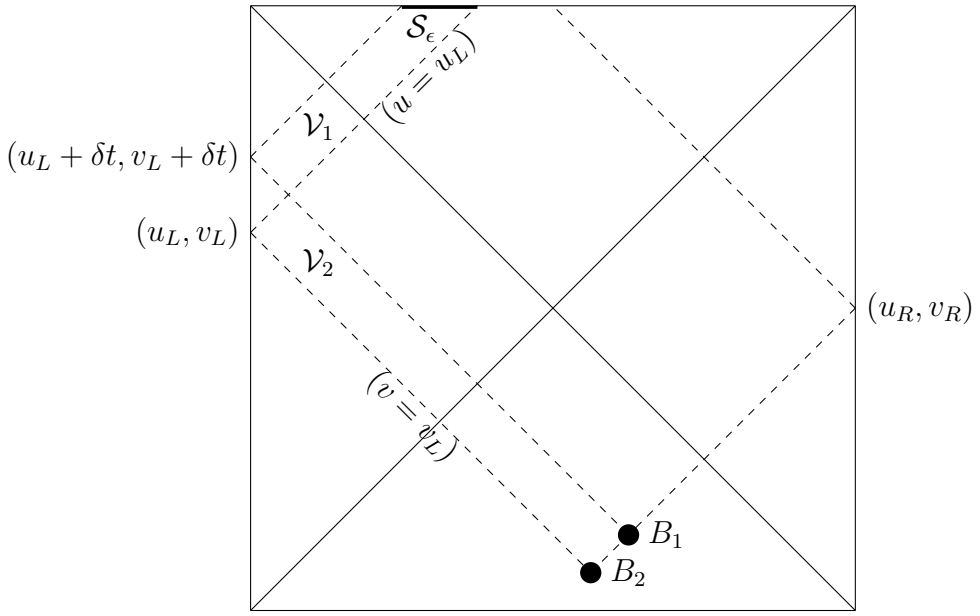

Figure 4.1: Two WDW patches separated by δt. Although the boundary of each patch is really at some large but finite r_b, the choice of r_b drops out in the differences we consider and we do not indicate it explicitly in this graphic.

It will prove convenient to utilize radial advanced/retarded null coordinates:

$$dr^* = \frac{R^2 dr}{r^2 f(r)}, \quad u = t + r^*, \quad v = t - r^*. \tag{4.12}$$

Notice that unlike r, r^* has units of length. Suppressing all but the bulk and timelike direction, the contributions to the time rate change of the WDW patch can be visualized in the conformal diagram represented in Figure 4.1.

The calculation of the time rate of change of the action is detailed in Appendix 4.6. It is convenient to express the result in terms of the radial coordinate r_B of the pastmost joint of the WDW patch (joint B_2 in the diagram 4.1, which coincides with joint B_1 as $\delta t \to 0$.) Note that r_B increases monotonically with t_L from $r_B = 0$ to $r_B = r_H$ as $t_L \to \infty$, and so we will use it to parameterize the time dependence of the complexification rate. [6] We find the following combined result:

$$\begin{aligned}\dot{S}_{WDW} = \frac{\Omega_5 V_3}{(2\pi)^7 \hat{g}_s^2}\Bigg(&\frac{-2\log(1+a^4 r_B^4)}{a^4} + 4r_B^4 + 6r_H^4 \\ &+ 3(r_H^4 - r_B^4)\log\Big|\frac{c\bar{c}\sqrt{\hat{g}_s}R^2 r_B^2}{\alpha(1+a^4 r_B^4)^{1/4}(r_H^4 - r_B^4)}\Big|\Bigg)\end{aligned} \tag{4.13}$$

where c and $\bar{c}$ are arbitrary constants associated with the normalization of boundary null generators entering the computation of δS_{joint}. See Appendix 4.6.3, as well as [103], [84] for discussion.

Various aspects of the time dependence (or r_B dependence) of equation 4.13 are unusual in light of the conjectured CA duality. Similar features have been seen in other systems [91]. We discuss the finite time behavior in Section 4.3.

[6] We consider only $t_L > 0$, and fix t_R so that this corresponds to when the joint B has left the past singularity.

The late time complexification rate is achieved by sending $r_B \to r_H$:

$$\dot{S}\big|_{t\to\infty} \approx \frac{\Omega_5 V_3 r_H^4}{(2\pi)^7 \hat{g}_s^2}\left(10 - 2\frac{\log(1+a^4 r_H^4)}{a^4 r_H^4}\right) \tag{4.14}$$

One can immediately see that if we assume the standard relationship, $\mathcal{C} = kS$ with $k = 1/\pi$, then the system violates the Lloyd bound (4.3) at late times: the ratio $\frac{\dot{S}}{2M}$ should be less than or equal to 1, but at late times it saturates values between 4/3 to 5/3 as we vary a. The relevance of the bound to holographic complexity has been disputed [92], and violations have been found in many other systems. But for purposes of comparison we find it interesting that, even if we had not assumed the standard $k = 1/\pi$, but instead used the logic that commutative black holes should saturate the Lloyd bound, we would set $k = 3/(4\pi)$. Clearly, the associated bound would fail immediately upon considering highly noncommutative black holes. Rather than proposing some different k in the relationship $\mathcal{C} = kS$, we find it plausible that such a choice does not generalize to all systems, at least under the current conventions for computing bulk action.

Overlooking the Lloyd bound for now, the dependence of the late time complexification on the noncommutativity parameter a is rather striking.

As one can see from Figure 4.2, the complexification rate increases with the non-commutativity parameter a, or more specifically the Moyal scale. It's also intriguing that a always appears in the combination ar_H, indicating that the only reference scale in the theory that the Moyal scale is sensitive to is the thermal scale $T^{-1} \sim r_H^{-1}$. When $a \ll T^{-1}$, the complexification rate does

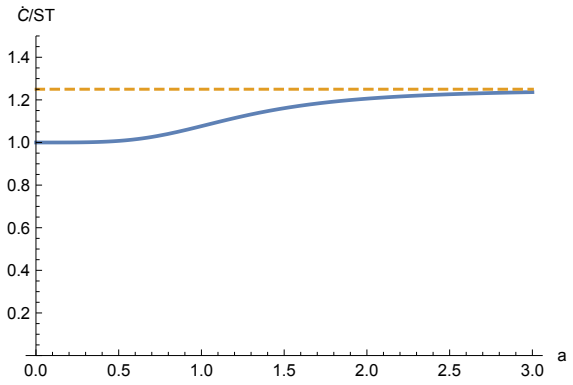

Figure 4.2: Late time action growth rate normalized by ST, versus Moyal scale a (in unit of thermal length). It is observed that the complexification rate under the CA conjecture increases significantly when the Moyal scale is comparable to the thermal scale, and saturate a new bound which is 5/4 of the commutative value when the Moyal scale is much larger than the thermal scale.

not change much. It noticeably changes when a becomes comparable to T^{-1}. When $a \gg T^{-1}$, the complexification rate stops growing and saturates a new bound. It is inspiring to see that it does not grow indefinitely because that will violate the Lloyd bound in any possible sense. On the other hand, the ratio that it increases is an interesting rational number 5/4. It may imply that this enhancement could be understood as some counting problem. With all these interesting features in mind, we want to answer two questions:

1. How might we explain the enhancement from non-commutativity?

2. Are there other examples of noncommutative theories that corroborate these results?

These will provide the content for the next few sections.

4.2 Non-Commutativity Enhancement of Complexification Rate

Why the above enhancement should be exactly 25% is as of yet unclear. We do, however, have a conceptual argument for why there should be a noncommutative enhancement at all.

Consider the following problem: We have a unitary operator U, whose complexity is known to be $\mathcal{C}(U)$, and we want to know what can be said about the complexity of $\mathcal{C}(U^N)$ for some integer N. One thing that can be immediately said is that

$$\mathcal{C}(U^N) \leq N\mathcal{C}(U) \tag{4.15}$$

Because given an optimal circuit Q implementing U, U^N can be implemented by N successive applications of Q, namely Q^N. [7] The bound above need not be saturated, however, as there might be a few gates at the beginning of Q which can cancel with some at the end of a successive copy of Q, resulting in a new circuit which (a unitary identical) to Q^N, but which is less complex. If we suppose that every time a new copy of U is added (after the first one

[7] There is a subtlety here in that Q only need implement a unitary that is within some small number ϵ of U, but if this is the case, there is no guarantee that Q^N will be within ϵ of U^N. It is also possible that for particular choices of gate set, some power of Q, say Q^M, may itself be a gate. This would result in "saw tooth" growth in complexity and periodically discontinuous time derivatives. It may be hoped that such issues are rendered obsolete in an appropriate continuum limit (as in the "geometry of complexity" program [104, 105]), and we ignore these subtleties for the present discussion.

of course), we get a cancellation of χ gates, and we suppose that χ doesn't depend on N (or at least asymptotes to a constant as N becomes large), then we have

$$\mathcal{C}(U^N) \approx N\mathcal{C}(U) - (N-1)\chi \tag{4.16}$$

It's easy to show that this formula holds for any $U \to U^n$ with the same χ.

If we are then interested in the (time evolution of the complexity of a family of operators) generated by some hamiltonian H

$$U(t) = e^{iHt}, \tag{4.17}$$

then we may use the above to write

$$\mathcal{C}(t) \equiv \mathcal{C}(U(t)) = \mathcal{C}[U(\delta t)^{t/\delta t}] \approx \frac{t}{\delta t}\left[\mathcal{C}(\delta t) - \chi\right] + \chi. \tag{4.18}$$

This will be true for any t and δt. Therefore we can compute the complexification rate

$$\frac{d}{dt}\mathcal{C}(t) \approx \frac{1}{\delta t}\left[\mathcal{C}(\delta t) - \chi\right]. \tag{4.19}$$

Now, what happens if we turn on non-commutativity in our theory? Let us suppose that our Hamiltonian $H = H_a$ varies continuously with the Moyal scale a, and suppose that our gates vary continuously as well so that the gates in the noncommutative theory can be identified with gates in the commutative theory. Suppose furthermore that for sufficiently small δt, $U_a(\delta t) = e^{iH_a\delta t}$ can be optimally approximated by the same circuit Q, but with each of the original gates g replaced with its noncommutative analog g_a (Call this circuit Q_a). Then it is still true that U_a^N can be implemented by Q_a^N. But now, because

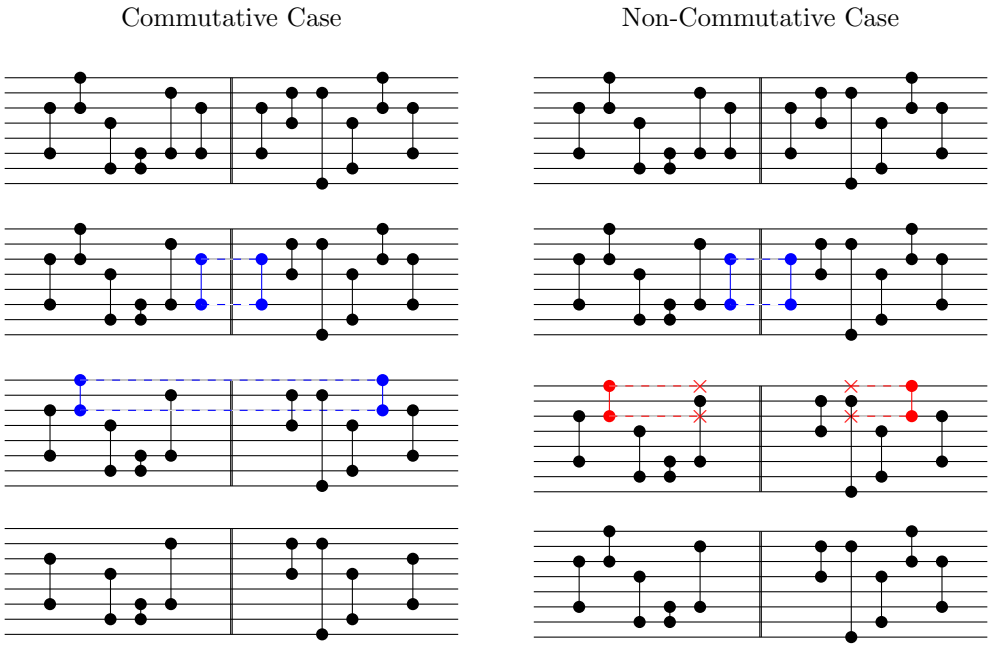

Figure 4.3: This circuit represents the end of one copy of a circuit Q_U implementing a hypothetical unitary U and the beginning of a second copy of Q_U. In this plot horizontal lines are qubits, and the dots connected by vertical lines are gates acting on the pair of qubits they connect. For this illustration, we will consider gates to be their own inverse. Gates from two copies may cancel (illustrated here with dashed blue lines connecting the gates), reducing the complexity of the circuit and providing a more efficient way to compute U^N. This cancellation relies, however, on the ability of gates to commute past each other, so that gates which could cancel can meet. We argue that in the non-commutative case, fewer gates commute and so there are fewer cancelations of this type. In this illustration, we see on the third line that a gate which can commute to cancel in the commutative case is prevented from doing so in the non-commutative case due to mild non-locality. Cartoon inspired by one used in a talk by Adam Brown.

of the non-commutativity, it is likely that fewer of the gates at the beginning and end of Q will commute with each other (see figure 4.3). And so we can still write

$$\mathcal{C}_a(t) \approx \frac{t}{\delta t}\left[\mathcal{C}_a(\delta t) - \chi_a\right] + \chi_a \approx \frac{t}{\delta t}\left[\mathcal{C}(\delta t) - \chi_a\right] + \chi_a, \tag{4.20}$$

but because fewer gates cancel, χ_a will be smaller than the original χ. These mean that the complexifaction rate

$$\dot{\mathcal{C}}_a(t) \equiv \frac{d}{dt}\mathcal{C}_a(t) \approx \frac{1}{\delta t}\left[\mathcal{C}(\delta t) - \chi_a\right] \tag{4.21}$$

gets an enhancement due to the suppression of χ_a. Finally we get an enhancement ratio of complexification rate as

$$\dot{\mathcal{C}}_a(t) \approx \frac{\mathcal{C}(\delta t) - \chi_a}{\mathcal{C}(\delta t) - \chi}\dot{\mathcal{C}}(t). \tag{4.22}$$

The same effect could be understood as arising from an increased nonlocality due to the noncommutativity. The dependence of complexity growth on the locality of gates is explored in [81], where an extension of the Lloyd bound is studied by looking at the "k-locality" of the Hamiltonian and the gate set. A "k-local" operator is one that acts on at most k degrees of freedom: a k-local Hamiltonian consists of interactions coupling at most k degrees of freedom, and similarly a k-local gate set consists of at most k-local operators. [8] For convenience we let the Hamiltonian be "k-local" while the gate set is

[8] To avoid dependence on the choice of basis, we would like to define k as the maximum rank of the coupling terms, or the maximum rank of the generators of the gates.

"j-local." Usually, the Lloyd bound should be satisfied if $j = k$, because one can choose the coupling terms as gates so that the time evolution could be easily implemented by the gates. However if one chooses a different j for the gate set, a bound of the following general form is to be expected

$$\dot{\mathcal{C}} \leq \frac{g(k)}{g(j)} \frac{2M}{\pi}, \tag{4.23}$$

where $g(k)$ is a monotonically increasing function. The interesting connection to our interpretation of non-commutativity is that the Moyal area introduced in non-commutative space can be thought of as an effective k for the Hamiltonian, meaning that non-local interactions couple wider range of degrees of freedom than local interactions. On the other hand, we are not changing j because our holographic prescription is not changed. Then we have an extra factor $g(k)/g(j) > 1$ in the bound, hence an enhanced bound. A similar factor greater than 1 is hence obtained in eq(4.22).

4.3 Finite Time behavior

Up to now, we have only discussed the asymptotic behavior of the complexification rate at late times. It is plausible that the early time complexification rate is not as important as the late time limit because there is a thermal scale time resolution for this quantity. One might think of this resolution as the time scale for a new gate to act on the state. In the paper [91] people carefully studied the finite time behavior of the complexification rate and found several interesting features. We will briefly outline the finite time

behavior for noncommutative SYM, reproduce those features, and find new features introduced by the non-commutativity.

We will rewrite equation (4.13) using the dimensionless parameters

$$b = ar_H, \quad \rho = r_B/r_H, \quad \gamma = \frac{c\bar{c}\sqrt{\hat{g}_s}R^2}{\alpha' r_H^2}, \tag{4.24}$$

so that we get

$$\frac{\delta S}{\delta t} = \frac{\Omega_5 V_3 r_H^4}{(2\pi)^7 \hat{g}_s^2}\left(\frac{-2\log(1+b^4\rho^4)}{b^4} + 4\rho^4 + 6 + 3(1-\rho^4)\log\left|\frac{\gamma\rho^2}{(1+b^4\rho^4)^{1/4}(1-\rho^4)}\right|\right). \tag{4.25}$$

Note that since $T = r_H/\pi$, we have $b = \pi a T$.

We will now normalize this by the late time commutative result at the same temperature to define

$$\dot{C}_{\rm n}(\rho) = \frac{-\log(1+b^4\rho^4)}{4b^4} + \frac{1}{2}\rho^4 + \frac{3}{4} + \frac{3}{8}(1-\rho^4)\log\left|\frac{\gamma\rho^2}{(1+b^4\rho^4)^{1/4}(1-\rho^4)}\right| \tag{4.26}$$

Substituting left time in thermal units for ρ, can plot $\dot{C}_n$ vs time at fixed b and γ, yeilding (in the case where we take $b \to 0$ and $\gamma = 80$) the plot in figure 4.4.

It is clear from this plot that there is a local maximum at early time (around $t = 0.1\beta$, β being the inverse temperature), and then at late times, it approaches the smaller asymptotic value from above. There is also a logarithmic divergence as t goes to zero which comes from the log term in equation (4.26). Both of these features are observed in [91], where they are discussed in

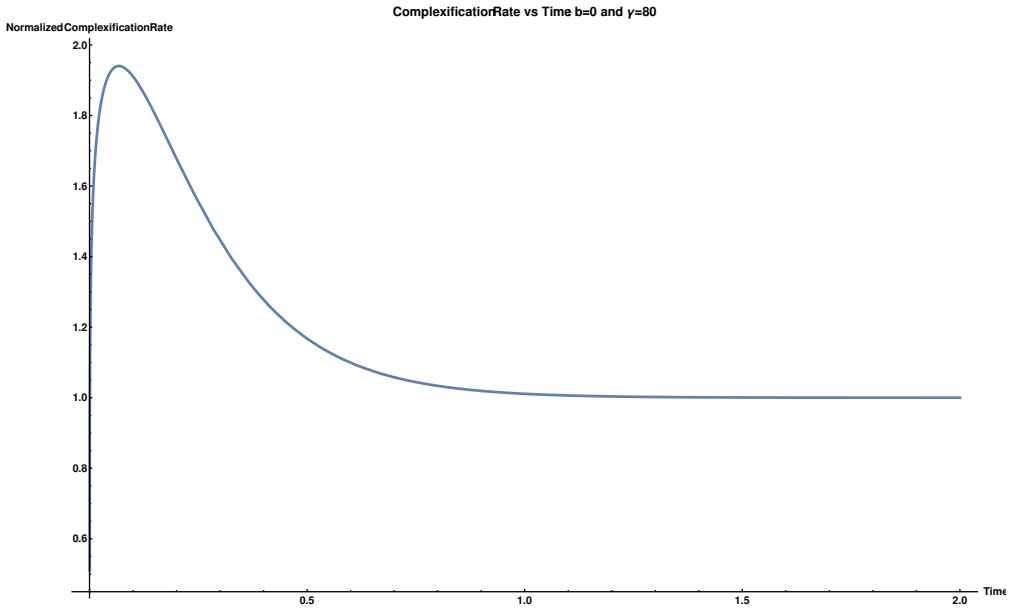

Figure 4.4: Normalized complexification rate versus time in thermal units for $\gamma = 80$ and $b = 0$.

great detail. The logarithmic divergence is not important in the sense that if you take the average complexification rate over a roughly thermal time scale, this divergence will be gone. A small period of decreasing complexity remains, but such behavior is not altogether prohibited. At early times the complexity is highly sensitive to the choice of the reference state, and only at late times is a constant growth rate expected for generic (time-independent) Hamiltonians. Regardless, the issues of the local maximum and the asymptotic approach to the "bound" from above are not resolved in any explanations here. One could average over an artificially long period of time to smooth out the local maximum, but doing so would never eliminate the approach from above, irrespective of the physicality of such a procedure.

Our primary interest here, however, is to discuss how these behaviors change with the noncommutative parameter b. To that end, we will consider what happens when we replot this curve fixing γ but varying b. The result is displayed in figure 4.5.

From figure 4.5 we see that as the non-commutativity is turned up, the local maximum decreases, and the asymptotic value increases. It is obvious that the change happens at $b \sim \pi$, which is when the Moyal scale a is comparable to the thermal scale $T^{-1} = \pi/r_H$. For $b \gg \pi$, it seems that the asymptotic value is approached from below. Strictly speaking, it is not true, because the local maximum always exists, but has a diminishing relative height and is pushed to very late time. We can find the local maximum and plot its ratio to the asymptotic value versus b as in figure 4.6. The fact that

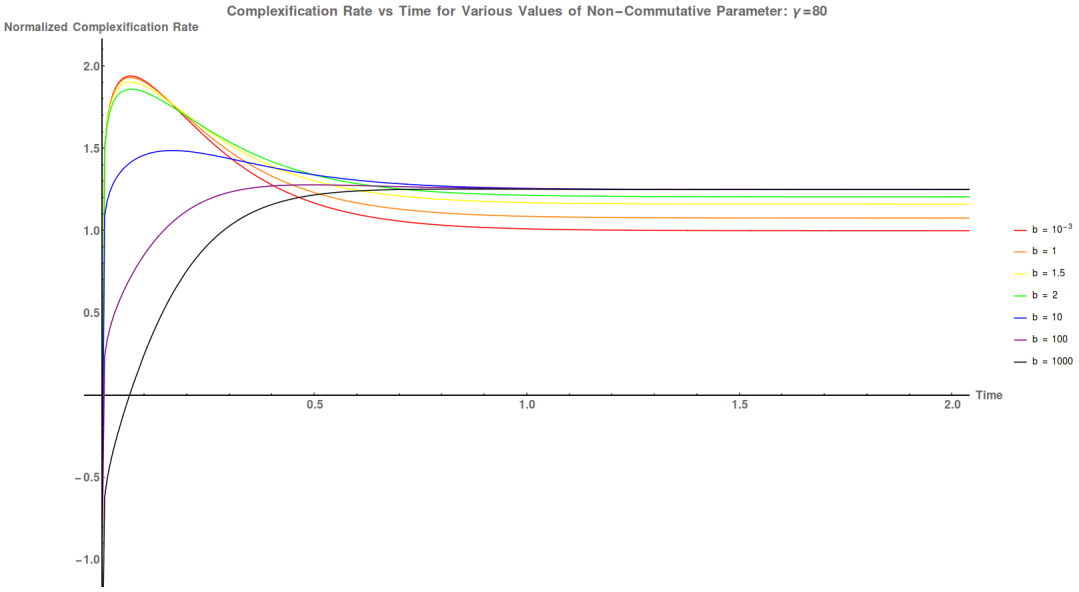

Figure 4.5: normalized complexification rate versus time in thermal units. γ is held fixed at 80 while $b = ar_H$ is varied.

the local maximum decays physically rather than by tuning some artificial choice is a sign that the noncommutative complexification rate at late time is a more qualified bound for a generic quantum system. We will discuss it in more details in the conclusion.

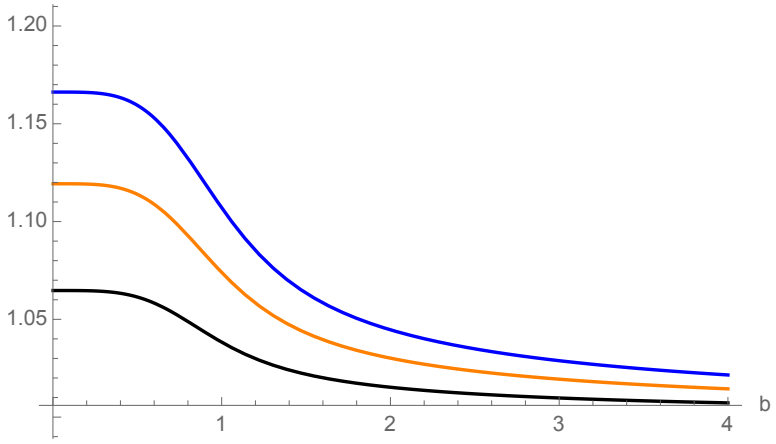

Figure 4.6: The vertical axis is the ratio between the local maximum and the asymptotic late time value of the complexification rate. The black, orange and blue curves correspond to $\gamma = 1, 2, 3$.

It is observed that the complexification rate mainly depends on temperature through the combination b, except an extra logarithmic contribution from γ. Therefore we expect that the variation with respect to temperature is similar to figure 4.5. This can be implemented by varying b while fixing the combination γb^2, i.e., fixing a. When this is done with $\gamma b^2 = 1$ one gets figure 4.7, which is indeed similar to figure 4.5. This check shows that the only scale that the non-commutativity a is sensitive to is the thermal scale.

Finally, one may also be interested in the effect of γ, which at fixed AdS

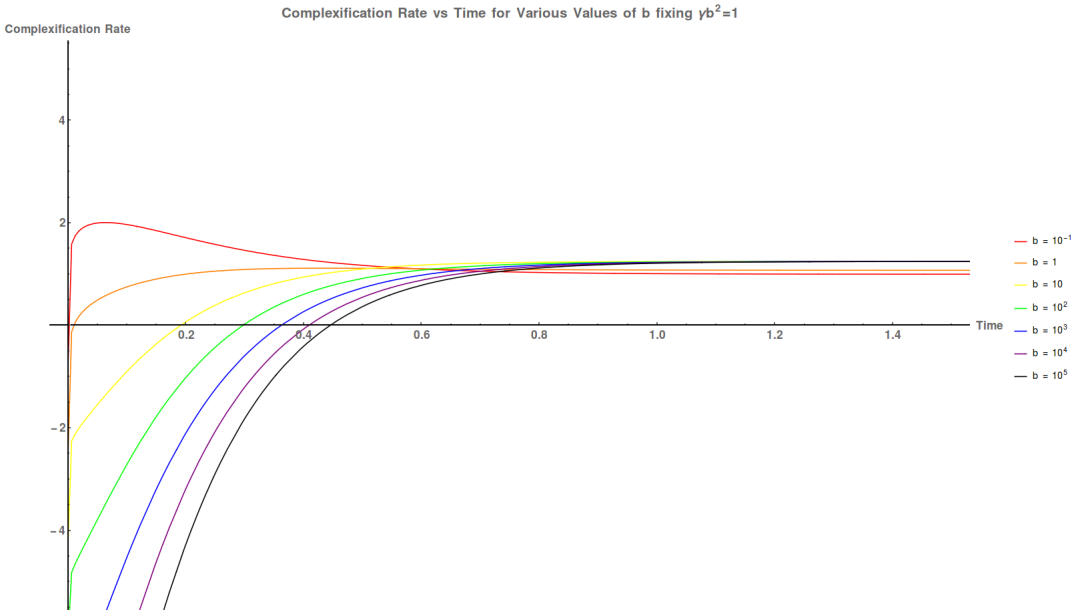

Figure 4.7: normalized complexification rate versus time in thermal units. γb^2 is held fixed at 1 while $b = ar_H$ is varied.

radius and temperature encodes information about the normalization of the generators of the null boundaries of the WDW patch. It has been suggested that this normalization, which is ambiguous in the action, should correspond to an ambiguity in the definition of complexity on the boundary such as the choice of reference state [84]. In our case, we observe that the dependence on γ does not depend on the non-commutativity at all, which seems to support this idea for a broader class of theories.

4.4 Other noncommutative systems

As a test of the above argument, and to better understand the dependence of the enhancement on various factors, we would like to consider more examples of noncommutative field theories. It's easy to extend the D3 brane solution we discussed in Section 4.1 to other Dp branes, in which we are also able to put more noncommutative pairs of directions. For $p = 4, 5, 6$, we can turn on more than one B field component, making multiple pairs of directions non-commuting. Let us denote the number of non-vanishing B components as m so that B will be a rank-$2m$ matrix. In this section, we will investigate the dependence of late time complexification rate on the dimension of space p and the rank of the B field.

4.4.1 Supergravity solutions and decoupling limit

The general string frame metric for non-extremal Dp branes with m non-commuting pairs of directions are given as

$$\begin{aligned}\frac{ds^2}{\alpha'} = &\left(\frac{r}{R}\right)^{\frac{7-p}{2}}\left(-f(r)dx_0^2 + \sum_{i=1}^{p-2m} dx_i^2 + \sum_{i=1}^{m} h_i(r)(dy_{i,1}^2 + dy_{i,2}^2)\right) \\ &+ \left(\frac{R}{r}\right)^{\frac{7-p}{2}}\left(\frac{dr^2}{f(r)} + r^2 d\Omega_{8-p}^2)\right)\end{aligned} \tag{4.27}$$

where

$$f(r) = 1 - \frac{r_H^{7-p}}{r^{7-p}}, \tag{4.28}$$

$$h_i(r) = \frac{1}{1 + (a_i r)^{7-p}}. \tag{4.29}$$

In NS-NS sector we have

$$\begin{aligned}e^{2\Phi} &= \hat{g}_s^2 \left(\frac{R}{r}\right)^{\frac{(7-p)(3-p)}{2}} \prod_{i=1}^{m} h_i(r), \\ B^{(i)} &= -\frac{\alpha'}{(a_i R)^{\frac{7-p}{2}}}[1 - h_i(r)]dy_{i,1} \wedge dy_{i,2}.\end{aligned} \tag{4.30}$$

We also have many R-R fields turned on via the T-duality. One would expect them by looking at the Chern-Simons term in D brane action

$$S_{CS}^{Dp} = \mu_p \int \left(C \wedge \exp(B + kF)\right)_{p+1}. \tag{4.31}$$

Only rank-$(p+1)$ R-R potential C_{p+1} is turned on without any background field, whereas in the presence of B field, terms like $C_{p+1-2n} \wedge B^{(i_1)} \wedge \cdots \wedge B^{(i_n)}$ can also be sourced, where $n = 0, 1, \cdots, m$. In other words, when $m = 1$, we have C_{p-1} turned on; when $m = 2$, we have C_{p-3} turned on, and so on.

The general formulae for all these R-R fields are

$$\begin{aligned}
C_{p+1} &= -\frac{(\alpha')^{\frac{p+1}{2}}}{\hat{g}_s}\left(\frac{r}{R}\right)^{7-p}\prod_i h_i(r),\\
C^{(j)}_{p-1} &= \frac{(\alpha')^{\frac{p-1}{2}}}{\hat{g}_s}\left(\frac{r}{R}\right)^{7-p}(a_jR)^{\frac{7-p}{2}}\prod_{i\neq j} h_i(r),\\
C^{(j,k)}_{p-3} &= -\frac{(\alpha')^{\frac{p-3}{2}}}{\hat{g}_s}\left(\frac{r}{R}\right)^{7-p}(a_ja_kR^2)^{\frac{7-p}{2}}\prod_{i\neq j,k} h_i(r),\\
C^{(j,k,l)}_{p-5} &= \frac{(\alpha')^{\frac{p-3}{2}}}{\hat{g}_s}\left(\frac{r}{R}\right)^{7-p}(a_ja_ka_lR^3)^{\frac{7-p}{2}}\prod_{i\neq j,k,l} h_i(r).
\end{aligned} \tag{4.32}$$

We are omitting the basis here, but it's clear that these components are along all the directions on Dp brane except for the directions of the B fields indicated by their superscript. We also omitted their (inverse) hodge dual forms which may contribute to the action.

While these are all good solutions for supergravity in the bulk, one has to be careful with its world volume dual theory. The decoupling limit of the world volume theories for $2 \leq p \leq 6$ in the presence of B field is studied in [106], with the conclusion that there is no decoupling limit for D6 branes even for $m > 0$. For $p \leq 5$, decoupling limits do exist, and it's reasonable to talk about the complexity on the world volume theory. One may be worried that for D4 brane we have to up lift to 11 dimensions to compute the M theory action, but the effective string coupling at high energy is

$$e^{\Phi} \sim r^{\frac{(7-p)(p-3-2m)}{4}}, \tag{4.33}$$

which is suppressed by the non-commutativity when $m \geq 1$, indicating that at sufficiently high energy, we don't have to go to M theory.

As such, we will be using type IIB action for odd p and type IIA action for even p. The type IIA action is

$$S^{\text{IIA}}_{\text{string}} = \frac{1}{2\kappa^2}\int dx^{10}\sqrt{-g}\left[e^{2\Phi}(\mathcal{R}+4|d\Phi|^2-\frac{1}{2}|H|^2)-\frac{1}{2}|F_2|^2-\frac{1}{2}|\tilde{F}_4|^2\right] - \frac{1}{4\kappa^2}\int B\wedge F_4\wedge F_4, \tag{4.34}$$

with the usual conventions:

$$F_2 = dC_1, \qquad F_4 = dC_3, \qquad \tilde{F}_4 = F_4 - C_1\wedge H. \tag{4.35}$$

4.4.2 Complexification Rates

We report the action growth rates with the following p-dependent prefactor,

$$c_p \equiv \frac{\Omega_{8-p} r_H^{7-p}}{(2\pi)^7 \hat{g}_s^2}, \tag{4.36}$$

We also divide out the transverse volume V_p to give a "density of action." The complexification rate will be related to the action growth rate by eq(4.10), where the coefficient k is not specified yet. We will discuss the strategy of choosing k at the end of the section. Both the joint and boundary contributions to the late time complexification rate take a particularly simple form:

$$\begin{aligned}\dot{S}_{\text{joint}} &= (7-p)c_p \\ \dot{S}_{\text{boundary}} &= \frac{1}{8}(65-14p+p^2)c_p\end{aligned} \tag{4.37}$$

The bulk contributions exhibit more interesting dependencies on the size and number of noncommutativity parameters. These are here reported for each p.

D2 Brane

This is the simplest case, where we have fewest R-R fields and don't need to put the self-duality constraint. We have

$$F_2 = dC_{p-1}, \tag{4.38}$$

$$\tilde{F}_4 = dC_{p+1} - C_{p-1} \wedge H. \tag{4.39}$$

Plugging them in the type IIA action, we obtain the complexity growth rate. Including all contributions, the late time limit becomes

$$\dot{S}_{p=2,m=1} = 12c_p. \tag{4.40}$$

Surprisingly, we find that the late time complexification rate does not even depend on the non-commutativity parameter a. We may argue that it is the case where the bound is already saturated so that non-commutativity could not enhance it anymore.

D4 Brane

This is the minimal dimension that we can include two pairs of non-commutative directions, hence $m = 2$. The R-R field contents are

$$F_2 = dC^{(1,2)}_{p-3}, \tag{4.41}$$

$$\tilde{F}_4 = \sum_i \left[dC^{(i)}_{p-1} - C^{(1,2)}_{p-3} \wedge H^{(i+1)} \right] + *^{-1} \left[dC_{p+1} - \sum_i \left(C^{(i)}_{p-1} \wedge H^{(i)} \right) \right]. \tag{4.42}$$

Note that mod m is understood in the supercript of the forms.

The complexity growth rate including all contributions has late time limit

$$\dot{S}_{4,2} = \left(5 + \frac{3a_1^3 a_2^3 r_H^6}{(1 + a_1^3 r_H^3)(1 + a_2^3 r_H^3)} \right) c_p. \tag{4.43}$$

The $p = 4,\ m = 0, 1$ cases can be obtained by taking one or both of the a parameters to zero:

$$\dot{S}_{4,0} = \dot{S}_{4,1} = 5c_4 \tag{4.44}$$

It's striking that turning on a single pair of noncommutative directions does not affect the late time complexification rate at all, but turning on the second pair does increase the rate. It means that we cannot use the argument as for $p = 2$ to explain the zero enhancement here because obviously the bound was not saturated yet.

D5 Brane

It's another case where we need to take into account the self-duality issue. Again we can have $m = 2$, and the R-R field contents are

$$F_3 = dC_{p-3}^{(1,2)} + *^{-1}\left[dC_{p+1} - \sum_i \left(C_{p-1}^{(i)} \wedge H^{(i)}\right)\right], \tag{4.45}$$

$$\tilde{F}_5 = \sum_i \left[dC_{p-1}^{(i)} - \frac{1}{2}C_{p-3}^{(1,2)} \wedge H^{(i+1)} + \frac{1}{2}dC_{p-3}^{(1,2)} \wedge B^{(i+1)}\right] + \text{self dual}. \tag{4.46}$$

The complexity growth rate including all contributions has late time limit

$$\dot{S}_{5,2} = \left(\frac{11}{2} + \frac{a_1^2 a_2^2 r_H^4 - 2}{2(1+a_1^2 r_H^2)(1+a_2^2 r_H^2)} + \frac{a_2^2 \log(1+a_1^2 r_H^2)}{2a_1^2(a_1^2 - a_2^2)} + \frac{a_1^2 \log(1+a_2^2 r_H^2)}{2a_2^2(a_2^2 - a_1^2)}\right) c_5. \tag{4.47}$$

We can also examine the $m = 1$ case by taking $a_2 = 0$ and $a_1 = a$:

$$\begin{aligned} \dot{S}_{5,1} &= \left(5 - \frac{1}{1+a^2 r_H^2}\right) c_p, \\ \dot{S}_{5,0} &= 4c_p \end{aligned} \tag{4.48}$$

In contrast with $p = 4$, turning on the first pair of noncommutative directions already changes the complexity, and turning on the second enhances more.

D6 Brane

Finally we may investigate a case where we can turn on 3 pairs of noncommutative directions, hence D6 brane. For $m = 3$, the R-R field contents

are

$$F_2 = dC_{p-5}^{(1,2,3)} + *^{-1}\left[dC_{p+1} - \sum_i \left(C_{p-1}^{(i)} \wedge H^{(i)}\right)\right], \tag{4.49}$$

$$F_4 = \sum_i \left[dC_{p-3}^{(i+1,i+2)} - C_{p-5}^{(1,2,3)} \wedge H^{(i)}\right] + *^{-1}\left[dC_{p-1}^{(i)} - \sum_{j\neq i} C_{p-3}^{(i,j)} \wedge H^{(j)}\right]. \tag{4.50}$$

The complexity growth rate including all contributions has late time limit

$$\dot{S}_{6,3} = \left(4 + \frac{a_1 a_2 \log(1 + a_3 r_H)}{(a_2 - a_3)a_3(a_3 - a_1)r_H} + \text{cyclic permutation}\right) c_6 \tag{4.51}$$

The three a-dependent terms have the property that no matter how many a's you turn off, their sum is a constant as -1. Thus again, it is a situation where only turning on maximum number of non-commutativity can we increase the non-commutativity, similar to the $p = 4$ case.

$$\dot{S}_{6,0} = \dot{S}_{6,1} = \dot{S}_{6,2} = 3c_6 \tag{4.52}$$

However, this complexity growth rate seems to have no physical meaning, because there is not a world volume theory that is decoupled from gravity. The holographic principle is subtle in this case. We present the result here because the bulk computation can be done in a similar manner without noting the difference. Whether the quantity so computed has any physical meaning is an open question.

p	$m=0$	$m=1$	$m=2$	$m=3$	πB_L
2	12	12	-	-	7
3	8	10	-	-	6
4	5	5	8	-	5
5	4	5	6	-	4
6	3	3	3	4	3

Table 4.1: This table lists all the action growth rate at late time for general p and m. They are in unit of the constant c_p defined in eq(4.36). The last column is showing the Lloyd bound B_L also in unit of c_p.

4.4.3 Summary of Results

From the above computation, we find that when we turn on non-commutativity on Dp branes, the complexity growth rate either stays the same, or increases. The fact that it does not decrease is encouraging for our argument given in section 4.2. However, the values of the enhancement ratio are not understood.

In the table 4.1, we list all the density of late time action growth rate in unit of c_p, in the limit that all m non-commutativity parameters a_i, $i = 1, .., m$, goes to infinity.

There are no obvious laws that govern these rates in general, but we do observe some interesting features. For both D3 and D5 branes, we have enhancement from each pair of non-commuting directions. In particular, the ratio for the enhancement from the first pair are the same in both cases, and the enhanced amount from the first and second pair are also the same in D5 brane. These two cases seem to provide reasonable behaviors one may naively expect. On the other hand, the type IIA supergravity with even-ps does not

always have complexification rate enhancement from non-commutativity. The reason for it may depend on the details of the boundary theory.

In the table 4.1, we also list the Lloyd bound computed from the ADM mass of the geometry (see Appendix 4.7). One may set the coefficient k in eq(4.10) to let any of the complexification rate to saturate the Lloyd bound. For instance, if we want to set the commutative $\mathcal{N} = 4$ SYM ($p = 3$, $m = 0$) to saturate the bound, we can take $\pi k_{p=3} = 3/4$. However, the consequence is that we can always turn on the non-commutativity and violate this bound. In order that the Lloyd bound is not violated, we need to guarantee that the maximum complexification rate for each p is bounded by B_L, thus

$$k_2 \leq \frac{7}{12\pi}, \quad k_3 \leq \frac{3}{4\pi}, \quad k_4 \leq \frac{5}{8\pi}, \quad k_5 \leq \frac{2}{3\pi}, \quad k_6 \leq \frac{3}{4\pi}. \tag{4.53}$$

If one follows the argument at the end of section 4.2, and get an enhanced bound for non-commutative field theory, the bound on k_p will be weaker. On the other hand, the Lloyd bound is defined under the assumption that all gates take a generic state to an orthogonal state, which is usually not true. It is argued that we simply should not take this bound seriously [92]. This objection will make it hard to determine what k should be, but for our purpose, k does not affect our main results.

4.5 Conclusion

In this paper, we have considered the effects of non-commutativity on the holographic complexity of SYM according to the complexity = action

conjecture. We have done this in the hope that this would produce further evidence about the validity of this conjecture, and of the concept of holographic complexity more generally. Our main result is that the late time complexification rate increases with the non-commutativity in a class of theories.

We computed the holographic complexity for 4D $\mathcal{N} = 4$ non-commutative super Yang-Mills, by evaluating the WDW action in the bulk geometry described by type IIB supergravity with D3 branes. We saw a 5/4 enhancement for late time complexification rate in the non-commutative result over the commutative result. This was striking because it is well known that the thermodynamics of this theory are independent of the non-commutative parameter a. The observed changes to complexity support the idea that complexity is more than thermodynamics, and indicates that the CA prescription is reproducing this feature of complexity. Comparing to the Lloyd bound derived from the total energy, we discovered that using the coefficient of proportionality $k = 1/\pi$ as in [80] will make the commutative late time complexification rate violate the bound. One could in principle avoid this by arguing that k should not be universal for all kinds of theories, but the commutative black hole still can not saturate the bound because there should be space for enhancement from the non-commutativity.

We presented a quantum argument to explain this enhancement and to argue that we should have expected it. We assume that the time evolution operator is approximated by sequential copies of the same quantum circuit, and the optimization of the total circuit when you combine them will be less

efficient in non-commutative theories. We also argue that this expectation matches the k-locality model prediction if we relate the size of Moyal scale to the size of locality k. Then we investigate the finite time behavior of this complexification rate and see that the problematic finite time maximum gets suppressed by non-commutativity.

Finally, we generalized the solution for D3 branes to general Dp branes to get a broader class of noncommutative gauge theories. We presented similar calculations as for $p = 3$ and obtained the late time complexification rates for $2 \leq p \leq 6$ and all allowed ranks of the B field. The results for $p = 5$ are similar to those for $p = 3$ but can have another enhancement of the same magnitude from a second B field component. This is consistent with our heuristic argument. The results for the even p cases are less well understood. We found that there is no enhancement for $p = 2$ and that for $p = 4$ one must introduce a second B field component to get an enhancement. This result would seem to be in mild tension with the argument of section 4.2. The correct explanation for this behavior is left for future work. Despite not seeing an enhancement in some cases, it is at least encouraging that no decrease was observed, which would have been a much clearer contradiction to the arguments of section 4.2.

Regarding the statement that non-commutativity enhances the complexification rate in general, there are several interesting aspects one can investigate. First, this result is in tension with the often expressed idea that the commutative AdS-Schwarzschild black hole is the fastest possible computer

[80]. If non-commutativity can somehow increase the computational speed even further, it would be very interesting to see if it also increases the scrambling process of the black hole. Second, it also would be interesting to compute the complexity of a weakly coupled field theory on a non-commutative manifold in order to test the conclusion of our heuristic argument in a non-holographic context. Such a computation would, in light of this work, provide for a more robust check on the complexity = action conjecture. The work of [83, 84] might prove useful to such an endeavor. Another interesting extension of this work would be to repeat the computations for the complexity = volume, and the complexity = spacetime volume conjectures, which will be both a test for our results and a test for the holographic complexity prescriptions. Finally, it was pointed out to us by Eoin Ó Colgáin that the geometry corresponding to the $D3$-brane case that we have considered here has been discovered to belong to a larger class of deformations of AdS_5, studied in e.g. [107–109]. It would perhaps be interesting to extend the results of this paper to the more general case.

4.6 Appendix I: Calculation of $\dot{S}_{WDW}$

To minimize clutter in expressions, in this appendix we set $2\kappa^2 = (2\pi)^7\alpha^4 = 1$ and reinstate κ dependence only at the end. Following the systematic treatment of [103], the action on a bulk subregion is divided into contributions as follows:

$$\begin{aligned} S_{\mathcal{V}} = &\int_{\mathcal{V}} \big(\mathcal{R} + \mathcal{L}_m\big)\sqrt{-g}dV \\ &+ 2\Sigma_{T_i}\int_{\partial\mathcal{V}_{T_i}} K d\Sigma + 2\Sigma_{S_i}\text{sign}(S_i)\int_{\partial\mathcal{V}_{S_i}} K d\Sigma - 2\Sigma_{N_i}\text{sign}(N_i)\int_{\partial\mathcal{V}_{N_i}} \kappa d\sigma d\lambda \\ &+ 2\Sigma_{j_i}\text{sign}(j_i)\int_{B_{j_i}} \eta_{j_i} d\sigma + 2\Sigma_{m_i}\text{sign}(m_i)\int_{B_{m_i}} a_{m_i} d\sigma \end{aligned} \tag{4.54}$$

The first line we call the bulk contribution. The second line contains boundary contributions along timelike ($\mathcal{T}$), spacelike ($\mathcal{S}$), and null boundaries ($\mathcal{N}$), respectively. The final line contains joint contributions, divided into those which result from intersections of timelike and/or spacelike boundaries, and those which include one or more null boundaries. Sign conventions and notation for integrand quantities will be explained as needed in what follows.

While the action on a WDW patch is obviously of interest for its conjectured relation to Quantum Complexity, its time derivative is simpler to compute and interesting for diagnostic purposes. Due to the spacetime symmetries, this quantity reduces to the difference of two volume contributions ($\mathcal{V}_1$ and $\mathcal{V}_2$ in figure 4.1), one boundary surface contribution ($\mathcal{S}_\epsilon$ in figure 4.1), and two joint contributions (B_1 and B_2 in figure 4.1).

$$
\begin{aligned}
\delta S_{\text{WDW}} &= \delta S_{\text{bulk}} + \delta S_{\text{boundary}} + \delta S_{\text{joints}} \\
\delta S_{\text{bulk}} &= S_{\mathcal{V}_1} - S_{\mathcal{V}_2} \\
\delta S_{\text{boundary}} &= -2 \int_{\mathcal{S}_\epsilon} K d\Sigma \\
\delta S_{\text{joints}} &= 2 \int_{B_1} a_1 d\sigma - 2 \int_{B_2} a_2 d\sigma
\end{aligned}
\tag{4.55}
$$

4.6.1 Bulk Contribution

The bulk integral contributions are of the form:

$$
S_{\text{bulk}} = \int_{\mathcal{V}} \sqrt{-g_E} \big(\mathcal{R} + \mathcal{L}_m \big) d\mathcal{V}, \tag{4.56}
$$

where Einstein frame metric is used. For the action eq(4.9) and field content eq(4.5) we have

$$
\mathcal{R} = \frac{-2\sqrt{\hat{g}_s} \big(2a^4 r_H^4 + a^8 r^4 (r^4 + r_H^4) \big)}{\alpha' R^2 (1 + a^4 r^4)^{9/4}}, \tag{4.57}
$$

$$
\mathcal{L}_m = \frac{2\sqrt{\hat{g}_s} \big(4a^4 r_H^4 + a^8 r^4 (3r^4 + r_H^4) \big)}{\alpha' R^2 (1 + a^4 r^4)^{9/4}}. \tag{4.58}
$$

We let the integral over x_1, x_2, and x_3 give V_3 and the five-sphere Ω_5. Also abbreviate $C = \dfrac{\alpha'^4 \Omega_5 V_3}{\hat{g}_s^2}$. Further let $\rho(u, v)$ and $\bar{\rho}(u, v)$ denote the radial value r as implicit functions of advanced/retarded coordinates u and v from the appropriate quadrant (here the left and bottom quadrants, respectively). The form of these functions is not important here.

The bulk contribution for $\mathcal{V}_1$ can be written in (u, r) coordinates with radial limits expressed implicitly.

$$S_{\mathcal{V}_1} = C\int_{u_L}^{u_L+\delta t} du \int_{r=\epsilon}^{r=\rho_L(u-v_L)} dr \frac{4r^3(a^8r^8+a^4r_H^4)}{(1+a^4r^4)^2}, \tag{4.59}$$

Here $r=\epsilon$ is a surface close to the singularity which will be sent to zero. A similar expression can be written for $\mathcal{V}_2$ in (v,r) coordinates, and after the radial integration we have:

$$\begin{aligned}\frac{1}{C}(S_{\mathcal{V}_1}-S_{\mathcal{V}_2}) = &\int_{u_L}^{u_L+\delta t} du\big(G(\rho_L(u-(v_L+\delta t)))-G(\epsilon)\big)\\ &-\int_{v_L}^{v_L+\delta t} dv\big(G(\rho_L(u_L-v)))-G(\bar{\rho}(u_R,v))\big)\end{aligned} \tag{4.60}$$

Changing variables $u \to u_L+v_L-v+\delta t$ leads to a cancellation of terms such that for small δt we are left with

$$\begin{aligned}S_{\mathcal{V}_1}-S_{\mathcal{V}_2} &\approx C\bigg(G\big(\bar{\rho}(u_R,v_L)=r_B\big)-G\big(\epsilon\big)\bigg)\delta t,\\ G(r) &= \frac{a^4(2r^4+a^4L^8-r_H^4)-2(1+a^4r^4)\log(1+a^4r^4)}{(a^4+a^8r^4)}.\end{aligned} \tag{4.61}$$

This cancellation is expected from the boost symmetry of the left wedge of the spacetime, and also indicates the cutoff independence of our calculation. We denote the radial value at the bottom corner of the WDW patch $\bar{\rho}(u_R,v_L)\equiv r_B$. As $\epsilon\to 0$ we find a bulk contribution of

$$\dot{S}_{\text{bulk}} = \lim_{\delta t\to 0}\frac{S_{\mathcal{V}_1}-S_{\mathcal{V}_2}}{\delta t} = \frac{\alpha^4\Omega_5 V_3}{\hat{g}_s^2}\bigg(\frac{a^4r_B^4}{1+a^4r_B^4}(r_H^4-r_B^4)+2r_B^4-\frac{2\log(1+a^4r_B^4)}{a^4}\bigg) \tag{4.62}$$

Note that r_B is related to t_L in the manner that as $t_L\to\infty$, $r_B\to r_H$. Therefore, the late time limit can be obtained by taking $r_B\to r_H$ limit.

4.6.2 Boundary Contributions

We adopt the convention that the null boundary geodesics are affinely parameterized: $k^\mu \nabla_\mu k^\nu = \kappa k^\nu$ with $\kappa = 0$, which simplifies the action computation considerably because all but one boundary surface ($\mathcal{S}_\epsilon$) make no contribution. The boundary $\mathcal{S}_\epsilon$ is the spacelike surface $r = \epsilon \to 0$. The contribution is of the form

$$\delta S_{\text{boundary}} = -2 \int_{\mathcal{S}_\epsilon} K d\Sigma \tag{4.63}$$

where $d\Sigma$ is the induced volume element on the boundary hypersurface and K is the extrinsic curvature: $K = g^{\mu\nu} \nabla_\mu s_\nu$ with the unit normal s^ν chosen to be future directed, away from the WDW patch. This convention for choosing the direction of the surface normal is responsible for the minus sign on this term [103].

For our metric eq(4.8) we have

$$K = \left(\frac{\hat{g}_s}{\alpha^2}\right)^{1/4} \frac{4rh(r)f'(r) + f(r)\left(32h(r) - rh'(r)\right)}{8Rh(r)^{7/8}\sqrt{-f(r)}}, \tag{4.64}$$

which as $\epsilon \to 0$ leads to

$$\dot{S}_{\text{boundary}} = 4r_H^4 \frac{\alpha^4 \Omega_5 V_3}{\hat{g}_s^2} \tag{4.65}$$

4.6.3 Joint Contributions

There are two joints (B and B') which contribute to the complexification rate. Each of these is comprised of the intersection of two null surfaces,

so their contributions are of the form

$$S_J = 2\Sigma_{m_i}\text{sign}(m_i)\int_{B_{m_i}} a_{m_i} d\sigma \tag{4.66}$$

$$a_{m_i} = \log\left|-\frac{1}{2}k_L \cdot k_R\right|$$

where dS is the volume element on the joint. Here k_L and k_R are future-pointing null generators along the left-moving and right-moving boundaries, respectively. Both of the joints in question lie at the past of the corresponding null segments, which together form the past boundary of a WDW patch. Together these facts determine that the sign of each joint's contribution to the WDW patch action is positive [103], and so taking a difference of two patches leads to the signs given in equation 4.55.

In addition to the affine parameterization of boundary generators, a convention must be chosen to fix their normalization. It may be possible to associate the freedom allowed by this choice with corresponding conventions which must be established in the definition of quantum complexity (e.g., choice of reference state and gate set). Indeed, progress has been made in this direction [84]. For our purposes, establishing a normalization convention is necessary to make meaningful comparisons between different WDW patch actions (such as that implicit in our "time derivative") as parameters of the theory are adjusted.

We normalize according to $k_L \cdot t_L = -c$ and $k_R \cdot t_R = -\bar{c}$, where $\hat{t}_R$ and

$\hat{t}_L$ are normalized generators of time-translation on each boundary. With this in mind we choose

$$\begin{aligned}(k_L)_\mu &= -c(\delta^t_\mu - \sqrt{\frac{-g_{rr}}{g_{tt}}}\delta^r_\mu) \\ (k_R)_\mu &= \bar{c}(\delta^t_\mu + \sqrt{\frac{-g_{rr}}{g_{tt}}}\delta^r_\mu).\end{aligned} \tag{4.67}$$

For small δt, the joints B_2 and B_1 are at fixed radii $r = r_B$ and $r = r_B + \frac{1}{2}\sqrt{\frac{-g_{tt}}{g_{rr}}}\delta t$, respectively. The quantities a_m in equation 4.66 are easily evaluated at each joint and the combined contribution is found to be:

$$\begin{aligned}S_{B_1} - S_{B_2} &= 2\frac{\alpha^4 V_3 \Omega_5}{\hat{g}_s^2}\left(r^3 \log\big[-\bar{c}c\frac{R^2(\hat{g}_s^2 h(r))^{1/4}}{\alpha r^2 f(r)}\big]\Big|^{r=r_{B_1}}_{r=r_{B_2}}\right) \\ &\approx \delta t\frac{\alpha^4 V_3 \Omega_5}{\hat{g}_s^2}\left(\frac{2r_H^4 + r_B^4(2 + a^4(3r_B^4 + r_H^4))}{1 + a^4 r_B^4}\right. \\ &\qquad \left. + 3(r_H^4 - r_B^4)\log\left|\frac{c\bar{c}\sqrt{\hat{g}_s}R^2 r_B^2}{\alpha(1 + a^4 r_B^4)^{1/4}(r_H^4 - r_B^4)}\right|\right)\end{aligned} \tag{4.68}$$

4.6.4 Combined Contributions

We can combine contributions 4.62, 4.65, and 4.68 to arrive at the full time rate change of the WDW patch action (reinstating explicit κ dependence and immediately using $2\kappa^2 = (2\pi)^7\alpha^4$):

$$\begin{aligned}\dot{S}_{WDW} = \frac{\Omega_5 V_3}{(2\pi)^7 \hat{g}_s^2}\Bigg(&\frac{-2\log(1 + a^4 r_B^4)}{a^4} + 4r_B^4 + 6r_H^4 \\ &+ 3(r_H^4 - r_B^4)\log\Big|\frac{c\bar{c}\sqrt{\hat{g}_s}R^2 r_B^2}{\alpha(1 + a^4 r_B^4)^{1/4}(r_H^4 - r_B^4)}\Big|\Bigg)\end{aligned} \tag{4.69}$$

4.7 Appendix II: Thermodynamics and the Lloyd Bound

It is interesting that the thermodynamic quantities for these systems exhibit no dependence on the noncommutativity parameter a (see [94] for discussion). We find that for general p[9]

$$\begin{aligned} E &= \frac{(9-p)r_H^{(7-p)}}{2(2\pi)^7\hat{g}_s^2}V_p\Omega_{(8-p)} \\ T &= \frac{(7-p)r_H^{(5-p)/2}}{4\pi R^{(7-p)/2}} \\ S &= \frac{4\pi R^{(7-p)/2}r_H^{(9-p)/2}}{(2\pi)^7\hat{g}_s^2}V_p\Omega_{(8-p)} \end{aligned} \tag{4.70}$$

with E being the ADM mass. The first law $dE = TdS$ is easily confirmed.

In the original CA duality conjecture [80, 81] the proportionality constant in Complexity $= k \times$ Action was fixed by an expectation that black holes are the fastest computers in nature, and that at late times they would saturate a bound from Lloyd [89, 90]. Matching $\dot{C} = \frac{2M}{\pi}$ at late times for Schwarzschild AdS black holes sets the constant at $k = \frac{1}{\pi}$. The relevance of the Lloyd bound to these considerations is questionable [92], but in the interest of comparison we note that the systems studied in this work would require different constants to meet the same criterion: for the commutative black holes to saturate the bound at late times, $k = \lim_{t\to\infty} \frac{2M}{\pi \dot{S}}$ would be given by

	$p=2$	$p=3$	$p=4$	$p=5$	$p=6$
k	$\frac{7}{12\pi}$	$\frac{3}{4\pi}$	$\frac{1}{\pi}$	$\frac{1}{\pi}$	$\frac{1}{\pi}$

[9]Note that for $p = 5$ equations 4.70 would indicate zero specific heat. We take this as further evidence that results for $p \geq 5$ should be viewed skeptically.

Furthermore, if the proportionality k were fixed with reference to commutative black holes, the bound would still be violated by highly noncommutative black holes. Rather than proposing novel bounds or searching over all systems for a minimum necessary $k = \lim_{t\to\infty} \frac{2M}{\pi \dot{S}}$ (giving the weakest bound on $\dot{S}$) to be the true proportionality in $\mathcal{C} = kS$, we suspect that the precise proportionality cannot be universally generalized between systems, at least under the established conventions for computing the WDW action.

Chapter 5

Holographic Subregion Complexity of Singular Surface

In the context of gauge/gravity duality we have learned that quantum entanglement in a field theory encodes information about the geometry of the dual spacetime. The holographic principle equates the entanglement entropy of a field theory to a geometrical object, the holographic entanglement entropy, in the dual spacetime. Therefore, entanglement plays a crucial role in the program of understanding how to reconstruct the dual spacetime from boundary (field theory) data. However, recently we have understood that entanglement entropy cannot be the only ingredient involved in spacetime reconstruction. After a black hole is formed, the interior grows for an exponentially large time but the holographic entanglement entropy fails to reproduce this growth [12, 110]. New developments point to quantum complexity as the missing ingredient [13, 111]. One way to think about complexity in quantum mechanical systems is as the minimum number of "simple" operations needed to go from a reference state to a target state. Quantum complexity is an active area of research in quantum information but little is known about complexity in quantum field theories. Two prescriptions for its dual, holographic complexity, have been put forward. These two proposals go by the names of complexity-volume

(CV) [14] and complexity-action(CA) [80, 81]. In the gravity side it is natural to also define a complexity not of the whole state but of a region of space, *i.e.* subregion complexity [112, 113]. The subregion complexity-volume proposal, subregion-CV, identifies the subregion complexity with the spatial volume bounded by the Ryu-Takayanagi and the boundary region. On the other hand, the subregion complexity-action proposal, subregion-CA, associates the complexity of a boundary region with the action evaluated on the intersection of the Wheeler-DeWitt (WDW) patch and the entanglement wedge of the given region [16]. Unfortunately, the meaning of subregion complexity in quantum information or field theory is not yet clear nor is it understood which of the holographic definitions is the correct one.

In the past, understanding the divergence structure of entanglement entropy in singular boundary regions was quite fruitful. A singular region is characterized by an opening angle $0 < \theta < 2\pi$. Cut-off independent coefficients, $a(\theta)$, arising for such regions were studied in a variety of quantum field theories [114–116] (free scalars, free fermions, interacting scalars) and in holographic models [117–120] as well. It was found that these coefficients represent an effective measure of the degrees of freedom of the underlying CFT. Furthermore, it was shown that the ratio $a(\theta \to \pi)/C_T$, where C_T is the central charge associated with the stress tensor $T_{\mu\nu}$, is universal for any $3D$ CFTs.

Inspired by these lessons, in this paper we study subregion complexity-action of a boundary region with a geometric singularity or kink. Our goal is to take a first step towards understanding if geometrical singularities in the

boundary region also encode cutoff independent and universal contributions to subregion complexity. To calculate subregion complexity-action we have to evaluate the action in the spacetime region determined by the intersection of the entanglement wedge and the Wheeler DeWitt patch. The calculation in the case of singular subregions is quite non-trivial. We discuss the appropriate way to define the infrared cutoff and develop a systematic approach to calculate all the divergences. The divergence structure is much richer than in the subregion complexity-volume case [121]. We find that the leading divergence is proportional to the volume of the boundary region and identify new contributions coming from the singularity to the cut-off independent coefficients of log and $\log^2$ terms. As in the case of subregion complexity-action for a smooth subregion, there are subleading divergences that depend on the normalization of null normals. We comment on this issue and on different choices of normalizations.

The contribution of our work is two-fold: 1) the systematic approach we develop to study the divergence structure of a region with a kink can easily be extended to higher dimensions and more general geometric singularities and 2) our detailed results can serve as a benchmark for proposals of subregion complexity in field theory.

This paper is organized as follows. In Section 5.1 we review the relevant ideas of entanglement entropy in singular regions and their significance. In Section 5.2 we review the definitions of subregion-CV and subregion-CA and recall the results for subregion-CV in a region with a kink obtained in [121].

Sections 5.3 and 5.4 constitute the main parts of this paper. In Section 5.3 we define the problem and point out the subtleties, then present the steps of calculations. In Section 5.4 we present the final result and discuss its various properties. Section 5.5 contains the conclusions and future directions. We also have two appendices: in Appendix 5.6, we present the details of extracting UV divergence structures, and the derivation of the final result, then we show the induced geometry on joint surfaces in Appendix 5.7.

5.1 Entanglement entropy in singular subregions

Spatial subregions in the boundary theory that contain geometric singularities are known to have interesting contributions to the entanglement entropy. In quantum field theory, the entanglement entropy has an area law behavior. But the coefficients of the leading order area law contribution depend on the UV regularization of the theory. On the other hand, there are subleading contributions that are independent of the UV regularization and thus, contain unambiguous information about the boundary theory [122]. These contributions were later shown to be universal for a large class of CFTs [114]. Therefore, when the boundary has sharp features or singularities, there will be extra contributions to the entanglement entropy that are universal and local on the boundary [118, 119]. In this section we will review some results related to entanglement entropy in singular regions.

The metric of $d+1$ dimensional AdS space in Poincare patch is,

$$ds^2 = \frac{L^2}{z^2}\left[-\,\mathrm{d}t^2 + \mathrm{d}z^2 + \mathrm{d}\rho^2 + \rho^2(\mathrm{d}\theta^2 + \sin^2\theta\,\mathrm{d}\Omega_n^2)\right]. \tag{5.1}$$

where $n = d-3$. A cone is an example of a singular region on the boundary. In general, cones in different dimensions can be parametrized as,

$$c_n = \{t = 0,\ |\theta| \leq \Omega,\ 0 \leq \rho < \rho_{\mathrm{IR}}\}. \tag{5.2}$$

where ρ_{IR} is an IR cutoff that has to be taken to infinity at the end of the calculation. The cone c_n has a scaling symmetry along the radial direction. Due to this symmetry, the Hubeny-Rangamani-Takayanagi (HRT) surface [123] has the form

$$z_{RT} = \rho\, h(\theta). \tag{5.3}$$

The function $h(\theta)$ has a maximum at $\theta = 0$ that we wil denote h_0, $h(0) = h_{max} \equiv h_0$, and vanishes at the boundary, $h(\Omega) = 0$. The entanglement entropy of c_n is given by the area

$$S_n = L^{n+2}\Omega_n \int \frac{\mathrm{d}\rho}{\rho} \int \mathrm{d}\theta\ \sin^n\theta \frac{\sqrt{1+h^2+h'^2}}{h^{n+2}}. \tag{5.4}$$

The extremality condition of the area determines the shape function $h(\theta)$. And since $h(\theta)$ specifies the HRT surface (5.3), this function will play an important role in the complexity calculations of the following sections.

In this paper we focus in $d = 3$, *i.e.* $n = 0$. Thus, we have a c_0 cone which we will refer to as a kink, k. In this case the integrand is independent

of θ and the area functional has an integration constant

$$K = \frac{1+h^2}{h^2\sqrt{1+h^2+h'^2}} = \frac{\sqrt{1+h_0^2}}{h_0^2}. \tag{5.5}$$

The opening angle, Ω can the be written as a function of h_0,

$$\Omega = \int_0^{h_0} \frac{\mathrm{d}h}{h'(\theta)} = \int_0^{h_0} \frac{Kh^2}{\sqrt{(1+h^2)(1+h^2-K^2h^4)}}\,\mathrm{d}h \equiv \int_0^{h_0} \omega(h)\,\mathrm{d}h. \tag{5.6}$$

The our purposes it is interesting to note the asymptotic behavior at small or large angles,

$$\begin{aligned} \Omega(h_0 \to 0) &\sim \gamma h_0 + \mathcal{O}(h_0^3), \\ \Omega(h_0 \to \infty) &\sim \frac{\pi}{2}(1-h_0^{-1}) + \mathcal{O}(h_0^{-2}), \end{aligned} \tag{5.7}$$

where

$$\gamma = \frac{\sqrt{\pi}\Gamma(3/4)}{\Gamma(1/4)} \approx 0.599. \tag{5.8}$$

The large angle limit is $\Omega = \pi/2$, indicating a flat opening angle, *i.e.* no kink. We will call this the "smooth limit". In this limit the contributions coming from the singular point should vanish.

Note that we can also look at opening angle 2Ω larger than π. Such kink indicates a concave corner. For the simple kink shape, the HRT surfaces are the same for $\Omega = \Omega_0$ and $\Omega = \pi - \Omega_0$, but the notion of "in" and "out" of this HRT surface is reversed.

In [120] the authors found that cone regions contribute to universal terms in the entanglement entropy. These contributions introduce new log or

$\log^2$ terms that are cutoff independent,

$$S_n^{\text{univ}}(V) = \begin{cases} (-1)^{\frac{d-1}{2}} a_n^{(d)}(\Omega) \log(R/\delta) & d \text{ odd}, \\ (-1)^{\frac{d-1}{2}} a_n^{(d)}(\Omega) \log^2(R/\delta) & d \text{ even}. \end{cases} \tag{5.9}$$

The functions $a_n^{(d)}(\Omega)$ are functions of the opening angle Ω. Since we are dealing with a pure state, $a_n^{(d)}(\Omega) = a_n^{(d)}(\pi - \Omega)$. An additional restriction on $a_n^d(\Omega)$ comes from the fact that when $\Omega \to \pi/2$ we are in the smooth limit, no singularity, and therefore $a_n^{(d)}(\Omega = \pi/2) = 0$. These constraints imply that in the large anlge limit $a_n^d(\Omega)$ is of the form

$$a_n^{(d)}(\Omega \to \pi/2) = 4\sigma_n^{(d)} \left(\frac{\pi}{2} - \Omega\right)^2. \tag{5.10}$$

Thus, the conical singularity introduces a set of coefficients σ_n^d that encode regulator-independent information about the CFT. Remarkably, this same behavior for $\sigma_n^{(d)}$ was found for field theory calculations of entanglement in regions with sharp corners [116]. Furthermmore, holographically, it can be shown that $\sigma_n^{(d)}$ is purely determined by the boundary stress tensor charge C_T. As mentioned in the Introduction, the motivation of the present work is to understand if similar cutoff independent and possibly universal contributions are present in the case of subregion complexity-action.

5.2 Subregion Complexity

Currently there are two proposals for for holographic subregion complexity, subregion-CV and subregion-CA. Both of these proposals recover the original holographic state complexity in the limit when the region is the whole

boundary. It is also required that they only include information from reasonably portion of the spacetime, i.e., the entanglement wedge.

In the CV approach, one takes the maximal spatial volume bounded by the boundary region and its HRT surface. Clearly, if we take the subregion to be the whole boundary we recover the original CV-complexity. Subregion-CV complexity was investigated in [112] for smooth subregions and in [121] for singular regions. In particular, for a 3 dimensional kink the subregion-CV complexity is [121],

$$\mathcal{C}_k = \frac{L^2}{8\pi G}\left[\frac{\Omega}{2}\frac{R^2}{\delta^2} - \alpha(h_0)\log\frac{R}{\delta}\right]. \tag{5.11}$$

Interestingly, besides the regular volume contribution, a new term with log divergence appears as the kink contribution. The coefficient

$$\alpha(h_0) = \int_0^{\Omega}\frac{\mathrm{d}\theta}{h^2} = \int_0^{h_0}\frac{\omega(h)}{h^2}\,\mathrm{d}h \tag{5.12}$$

has the limiting behavior

$$\begin{aligned}&\lim_{h_0\to 0}\alpha(h_0) = \frac{\gamma'}{h_0}, \quad \gamma' = \int_0^1 \frac{2}{\sqrt{1-x^4}}\,\mathrm{d}x \approx 2.622,\\ &\lim_{h_0\to\infty}\alpha(h_0) = \frac{\pi}{h_0}.\end{aligned} \tag{5.13}$$

In [16] the authors proposed that the subregion-CA complexity is given by the action evaluated on the intersection of the entanglement wedge of the subregion and the WdW patch of the boundary time slice. Fig 5.1 schematically shows half of the relevant bulk region, where the boundary (pink sheet) spatial region (red line) has an HRT surface (blue curve), that develops a

light sheet (pink surface) as the boundary of the entanglement wedge. The interval itself also develops a bulk light sheet (green surface) as the boundary of the WdW patch. The two light sheets intersect at the green curve, which delimits the closed region below wherein we evaluate the action. Of course, a symmetric counterpart is present in the past direction, which is not drawn for clarity.

5.3 Complexity-action of a region with 3d kink

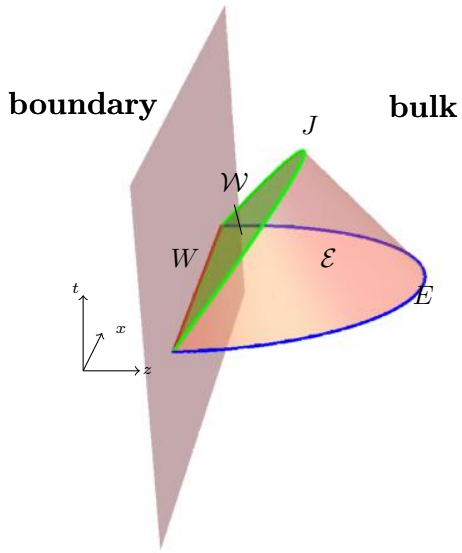

Figure 5.1: Intersection of the entanglement wedge and WDW patch is shown. For clearity, only the $t > 0$ part of the region $\mathcal{V}_+$ is explicitly shown, which should be understood as upper half of $\mathcal{V}$ while the lower half $\mathcal{V}_-$ is symmetric. As understood in the $\delta = 0$ limit, the red line represents both the boundary region $\mathcal{A}$ and the surface W on the cutoff surface. The blue curve represents the HRT surface E. The green and pink surfaces represent the null hypersurfaces $\mathcal{W}^+$ and $\mathcal{E}^+$, and their intersection at the green curve is the surface J^+.

5.3.1 Setup

To compute the holographic complexity of a 3d kink region $\mathcal{A}$ in CA approach, one has to first define the bulk region $\mathcal{V}$ on which we compute the action. According to the description in the last section, this region is delimited by a boundary that consists of 4 hypersurfaces:

$$\mathcal{W}^{\pm}: \ z = \delta \pm t, \ (x, y) \in A; \tag{5.14}$$

$$\mathcal{E}^{\pm}: \ X^{\mu}_{\pm}(\lambda) = X^{\mu}_{0} + f(\lambda) V^{\mu}_{\pm} \tag{5.15}$$

where $\mathcal{W}^{\pm}$ are the null boundaries of the WdW patch, and $\mathcal{E}^{\pm}$ are the null boundaries of the entanglement wedge. The HRT entangling surface is $E = \mathcal{E}^{+} \cap \mathcal{E}^{-}$. We express the location of E in terms of Cartesian coordinates in Poincare patch:

$$X^{t}_{0} = 0, \quad X^{z}_{0} = \rho h(\theta), \quad X^{x}_{0} = \rho \cos\theta, \quad X^{y}_{0} = \rho \sin\theta. \tag{5.16}$$

The $\mathcal{E}^{\pm}$ are generated by null normal vectors $V^{\mu}_{\pm}$ of E:

$$\begin{aligned} V^{<}_{\pm} &= \pm\sqrt{1 + h^2 + h'^2}\hat{\mathbf{t}} - \hat{\mathbf{z}} + (h\cos\theta - h'\sin\theta)\hat{\mathbf{x}} + (h\sin\theta + h'\cos\theta)\hat{\mathbf{y}} \\ V^{>}_{\pm} &= \pm\sqrt{1 + h^2 + h'^2}\hat{\mathbf{t}} + \hat{\mathbf{z}} - (h\cos\theta - h'\sin\theta)\hat{\mathbf{x}} - (h\sin\theta + h'\cos\theta)\hat{\mathbf{y}} \end{aligned} \tag{5.17}$$

The superscripts represent the orientation of E, since the kink with Ω and $\pi - \Omega$ share the same HRT surface, but differ by its orientation. For convex kinks with $\Omega < \pi/2$, one takes $V^{<}$; for concave kinks with $\Omega > \pi/2$, one takes $V^{>}$. Due to the conformal flatness in Poincare patch, the light rays are

straight lines, with linear coefficients $f(\lambda)$. This reparameterization function shall be determined later when we choose λ to be the affine parameter.

We further define $W = \mathcal{W}^+ \cap \mathcal{W}^-$ and $J^\pm = \mathcal{E}^\pm \cap \mathcal{W}^\pm$. W is on the cutoff surface δ which becomes $\mathcal{A}$ in the $\delta \to 0$ limit. These geometrical objects can be visually seen in Fig. 5.1

5.3.2 Subtle Issues in the Action Computation

Before we compute the action in $\mathcal{V}$, there are a few issues that worth careful studies. First, in the definition of $\mathcal{V}$, the null hypersurface $\mathcal{E}$ may not be smooth over the part we are interested in. The non-smoothness may be introduced by so-called caustics. Second, as the subregion we consider is not closed, we need a IR cutoff in order to implement the computation. There is however subtlety about defining this IR cutoff. Finally, the computation of action in a bulk region with boundary is not a completely well-studied problem, and we will show the defects of the current available technique for this computation.

5.3.2.1 Caustics

According to the focussing theorem, lightsheets are going to end on caustics in finite amount of affine time. If the lightsheet ends before it intersects with $\mathcal{W}^\pm$, the part of caustics should also be included as hypersurface that delimit the region. Caustics can be obtained by solving for the divergence

of expansion rate Θ of the lightsheet congruence

$$\Theta_{\pm} = \frac{1}{\sqrt{g_{\pm}}} \frac{\partial \sqrt{g_{\pm}}}{\partial \lambda} \tag{5.18}$$

where $g_{\pm,\alpha\beta}(\lambda)$ is the induced metric on equal λ slice of the light sheet (see Appendix 5.7), and λ should be the affine parameter of the geodesic $X^{\mu}_{\pm}(\lambda)$. We can solve the geodesic equation $k^{\mu}\nabla_{\mu}k^{\nu} = 0$ for $k^{\mu} \equiv \partial X^{\mu}_{\pm}/\partial\lambda$, which yields

$$f^{<}(\lambda) = \frac{\lambda\rho^2 h(\theta)^2}{L^2 + \lambda\rho h(\theta)}, \qquad f^{>}(\lambda) = \frac{\lambda\rho^2 h(\theta)^2}{L^2 - \lambda\rho h(\theta)}. \tag{5.19}$$

One can then solve for the expansion

$$\Theta_{\pm} = -\frac{2\lambda\rho^2 h^2}{L^4 - \lambda^2\rho^2 h^2}, \tag{5.20}$$

which diverges at

$$\lambda = \lambda_c \equiv \frac{L^2}{\rho h}. \tag{5.21}$$

This result does not depend on convexity of the kink (same for both superscripts $<$ and $>$).

To see if the caustic occurs before reaching the intersection $J^{\pm}$, we can solve for the λ values on $J^{\pm}$ by combining (5.14) and (5.15), thus $X^{z}_{\pm}(\lambda_*) = \delta \pm X^{t}_{\pm}(\lambda_*)$, as:

$$\lambda^{<}_{*} = \frac{\lambda_c(\rho h - \delta)}{\rho h\sqrt{1 + h^2 + h'^2} + \delta}, \qquad \lambda^{<}_{*} = \frac{\lambda_c(\rho h - \delta)}{\rho h\sqrt{1 + h^2 + h'^2} - \delta}. \tag{5.22}$$

Hence in our case, $\lambda_* < \lambda_c$ for all ρ and θ, and for both convex and concave kinks, which means that the caustics is totally outside of the region $\mathcal{V}$, so that we don't need to worry about it.

5.3.2.2 IR cutoff

Another tricky issue is the IR cutoff of the region. One would naively use the same cutoff R for radius coordinate on both $\mathcal{A}$ and E, but they are actually not consistent because the hypersurfaces $\mathcal{E}^{\pm}$ and $\mathcal{W}^{\pm}$ will not match exactly to enclose the region. To unambiguously define the IR cutoff, we can only set constant cutoff R for either of $\mathcal{A}$ and E, and find the cutoff on the other by following the null rays on the hypersurfaces, as shown by the dashed arrows in Fig.5.2. As we have already parameterized $\mathcal{E}^{\pm}$ in terms of coordinates (ρ, θ) on E, it should be easier to work with a constant IR cutoff at $\rho = R$ where ρ is defined to be projected radial coordinate on E.

We want to use ρ, θ to parameterize the whole region $\mathcal{V}$, so that the parameter range bounded by constant cutoff R sets the true range of $\mathcal{V}$. As the parameterization has been done along $\mathcal{E}$ up to the surface J as $X^{\mu}(\lambda)$, $0 < \lambda < \lambda_*$, we would like to continue along $\mathcal{W}$ towards the boundary surface W. We follow the null rays that generate $\mathcal{W}$, denoted by

$$U_{\pm} = \mp\hat{\mathbf{t}} - \hat{\mathbf{z}}, \tag{5.23}$$

with integral curve

$$\mathcal{W}^{\pm} : \tilde{X}^{\mu}_{\pm}(\eta) = X^{\mu}_{\pm}(\lambda_*) + \eta U^{\mu}_{\pm}. \tag{5.24}$$

The starting point $X^{\mu}_{\pm}(\lambda_*)$ is at the joint surface $J^{\pm}$, while the ending at W is solved through $\tilde{X}^{z}_{\pm}(\eta_*) = \delta$ as,

$$\eta^{<}_* = \frac{1+h^2}{H_+}(\rho h - \delta), \qquad \eta^{>}_* = \frac{1+h^2}{H_-}(\rho h - \delta), \tag{5.25}$$

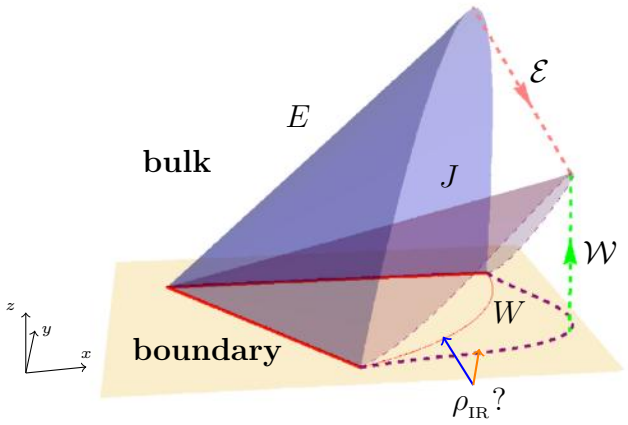

Figure 5.2: This is also showing the region $\mathcal{V}$, but with time direction suppressed by projection so that both spatial directions can be shown explicitly. The yellow plane is the boundary space, with the red curve denoting the surface of the kink. The blue surface is the HRT surface E and the purple one is J. The null hypersurfaces $\mathcal{E}$ and $\mathcal{W}$ are the volume between E and J and the volume between the boundary and J, while the red and green dashed arrows are typical null rays on them. It is clear that if we choose $\rho = R$ constant IR cutoff on E as shown here, the red null ray matches a corresponding green null ray only when the IR cutoff on the boundary takes the purple dashed curve instead of the naive orange circle.

where

$$H_\pm \equiv 1 + h^2 \pm Kh^2 \tag{5.26}$$

is a shorthand notation used throughout the paper. Now the surface W is parameterized as $\tilde{X}^\mu(\eta_*, \rho, \theta)$ where $\rho < R$ sets the cutoff boundary, as shown in Fig. 5.2 by the purple dashed curve.

In Fig. 5.3, we show exact shape of W for different kink openning angles. The blue shades are the true range of W while the yellow shades are

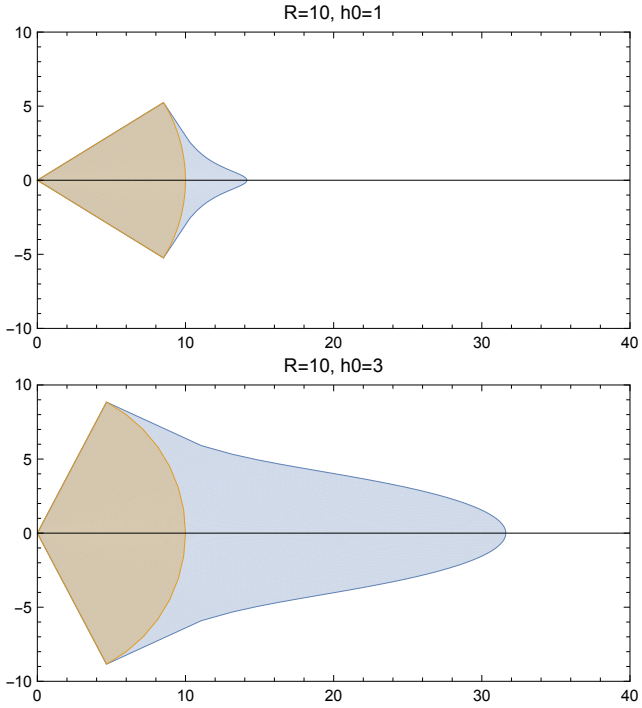

Figure 5.3: We plot the shape of surface W for different openning angles, labeled by corresponding values of h_0. The cutoff R is taken to be 10. The yellow shade represent the projection of E which has the shape of a sector with radius $R = 10$, and the blue shade is the true range of W with the same IR cutoff.

the projection of E on the boundary that has constant radial cutoff. We can see that when the openning angle is small, the extra piece is small and the volume is dominated by the sector shape of the projection; for large openning angle, the shape becomes much larger than the projection. In the limit of flat angle kink, W will have the shape of a half strip. For any openning angles, the two regions share the same boundary surface as the two straight sides.

Now that we parameterized all the boundary hypersurfaces by (ρ, θ),

we can naturally extend the parameterization to the whole region $\mathcal{V}$ together with $\zeta = f(\lambda)$ and η:

$$\mathcal{V}^\mu_\pm(\zeta, \eta, \rho, \theta) = X^\mu_0(\rho, \theta) + \zeta V^\mu_\pm(\rho, \theta) + \eta U^\mu_\pm \tag{5.27}$$

with range of parameters

$$\begin{aligned} &0 < \rho < R, \quad 0 < h < h_0, \quad \rho h > \delta, \\ &0 < \zeta < \zeta_* = f(\lambda_*), \quad 0 < \eta < \eta_*, \quad \frac{\eta}{\eta_*} < \frac{\zeta}{\zeta_*}. \end{aligned} \tag{5.28}$$

The last condition is to restrict the parameterization $\mathcal{V}_\pm$ to $\pm t > 0$ region, and hence $\mathcal{V} = \mathcal{V}_+ \sqcup \mathcal{V}_-$. Due to time reflection symmetry, the action should be twice the action in either of $\mathcal{V}_\pm$.

For readers' convenience, we also write the bulk reparameterization explicitly in the form of coordinate transformation (for convex kink):

$$\begin{aligned} t &= \pm\zeta\sqrt{1 + h^2 + h'^2} \mp \eta, \\ z &= \rho h - \zeta - \eta, \\ x &= \rho\cos\theta + \zeta(h\cos\theta - h'\sin\theta), \\ y &= \rho\sin\theta + \zeta(h\sin\theta + h'\cos\theta). \end{aligned} \tag{5.29}$$

5.3.2.3 Higher Codimension Manifolds on the Boundary

We can write down the most general form of gravitational action as

$$I_{\text{grav}} = \frac{1}{8\pi G}\sum_{d=0}^{D}\sum_{i}^{n_d}\int_{\Sigma_i^{(d)}}\sqrt{\sigma_i^{(d)}}\phi_i^{(d)}, \tag{5.30}$$

where $\Sigma_i^{(d)}$ are dimension d manifolds with metric $\sigma_i^{(d)}$ that are relevant for the spacetime region in which we compute action. In particular, $\Sigma_i^{(D)}$ are the bulk

regions with D the total dimension of spacetime. For this bulk integration, the integrand is, say, the Einstein-Hilbert term, hence $\phi^{(D)} = \frac{1}{2}R + \Lambda$. When $d < D$, $\Sigma_i^{(d)}$ are manifolds on the boundaries of $\Sigma_i^{(D)}$. For example, a cube is a region $\Sigma^{(D=3)}$ with boundary manifolds $\Sigma^{(2)}_{1,\cdots,6}$ as the surfaces, $\Sigma^{(1)}_{1,\cdots,12}$ as the edges and $\Sigma^{(0)}_{1,\cdots,8}$ as the vertices. For $\Sigma^{(D-1)}$, as long as it is non-null, we have the usual York-Gibbons-Hawking (YGH) term $\phi^{(D-1)} = K$, *i.e.* the trace of the extrinsic curvature.

Note that for Lorentzian spacetime there can be null manifolds on the boundary, which has degenerate metric. Contributions from null $\Sigma_i^{(D-1)}$ has been studied [124], which shows that the volume form should be modified and the integrand should be the surface gravity:

$$\frac{1}{8\pi G}\int_{\text{null }\Sigma_i^{(D-1)}} \sqrt{\sigma_i^{(D-2)}}\kappa \ \mathrm{d}\lambda\, \mathrm{d}x^{D-2}, \tag{5.31}$$

where λ is the null parameter and κ is the surface gravity associated with null vector field $\partial/\partial\lambda$. Inspired by the CA conjecture, further studies have been done for contributions from higher codimension manifolds. The codimension 2 non-null manifolds, called joints, were studied in [103] which provides the integrand as

$$\phi^{(D-2)}_{\Sigma_i^{(D-1)}\cap\Sigma_j^{(D-1)}} = \pm\log\frac{k_i\cdot k_j}{2}, \tag{5.32}$$

where the joint is specified as intersection of two codimension 1 manifolds $\Sigma_{i,j}^{(D-1)}$. We only present here the case when both $\Sigma_{i,j}^{(D-1)}$ are null, as it is the only relevant case for our computation. $k_{i,j} = \partial/\partial\lambda_{i,j}$ are null generators of

the codimension 1 manifolds, and the sign depends on the orientation of the intersection.

In this paper, we only compute the action up to the joint contributions as

$$I_{\text{total}} = I_{\text{bulk}} + I_{\text{YGH}} + I_{\text{null}} + I_{\text{joint}}, \tag{5.33}$$

omitting the higher codimention singular features, which need further analysis and remain unknown. Although it was mentioned in [125] that a high codimension conical singularity can be regulated to a geometry with only lower dimensional singular surface, and through the regulation it was shown that the conical singularity does not contribute to the action, the regulation method cannot be generalized to deal with general singular features, like polyhedral singularity, *i.e.* the intersection of several hypersurfaces. The polyhedral singularity naturally appear in any subregion CA computation, the common one being the codimension 3 manifold ∂W sitting at the intersection of all of the four $\mathcal{E}^{\pm}$ and $\mathcal{W}^{\pm}$ hypersurfaces. For our case when there is additional singular feature on the surface of the boundary subregion, it introduces even higher codimension singularity on ∂W. These are all polyhedral singularity that cannot be reduced through regulation, therefore we can only list them here for future studies on corner contributions to gravitational action.

5.3.3 Bulk contributions

Let's first deal with the bulk action, which is simply the Einstein-Hilbert term in our AdS vacuum case,

$$I_{\text{bulk}} = \frac{1}{16\pi G}\int_{\mathcal{V}}\sqrt{-g}\ (R-2\Lambda) = -\frac{3}{8\pi G L^2}\int_{\mathcal{V}}\sqrt{-g} \tag{5.34}$$

It would be convenient to write the metric in the new set of coordinates $\xi^a = \{\zeta, \eta, \rho, \theta\}$, so that it's given by

$$g^{\xi}_{ab} = \frac{\partial \mathcal{V}^\mu}{\partial \xi^a}\frac{\partial \mathcal{V}^\nu}{\partial \xi^b} g^0_{\mu\nu} \tag{5.35}$$

where g^0 is the original Cartesian coordinates of AdS_4. Its determinant turns out to have the simple form

$$\sqrt{-g^{\xi}_{<}} = \frac{(1+h^2)H_+(\rho h - 2\zeta)}{K^2 h^5(\rho h - \zeta - \eta)^4}L^4, \tag{5.36}$$

$$\sqrt{-g^{\xi}_{>}} = \frac{(1+h^2)H_-(\rho h + 2\zeta)}{K^2 h^5(\rho h + \zeta - \eta)^4}L^4. \tag{5.37}$$

We first integrate along ζ and η directions. According to eq(5.28), we get

$$\begin{aligned} I_{\text{bulk}} &\equiv -\frac{3}{8\pi G L^2}\int_{A_\delta}\mathrm{d}\theta\,\mathrm{d}\rho\ 2\int_0^{\zeta_*}\mathrm{d}\zeta\int_0^{\frac{\eta_*}{\zeta_*}\zeta}\mathrm{d}\eta\ \sqrt{-g^{\xi}_{<_>}} \\ &= \int_{A_\delta}\mathrm{d}\theta\,\mathrm{d}\rho\ \left(-\frac{L^2}{8\pi G}\right)\times \\ &\qquad \frac{(1+h^2)^2(\rho h-\delta)^2\left[h(1+h^2)H_\mp\rho^2 + 2(H_\pm^2 - 2K^2h^4)\rho\delta \pm Kh(3H_+ + 2Kh^2)\delta^2\right]}{Kh^5 H_\pm \rho\delta^2(\rho + \rho h^2 \pm Kh\delta)}. \end{aligned} \tag{5.38}$$

The range of (ρ, θ) is denoted by A_δ indicating that the parameter range in the bulk should be cutoff by $z = \delta$, and hence is slightly smaller than eq(5.2). The integration can be written explicitly in two forms as

$$\begin{aligned}\int_{A_\delta} \mathrm{d}\theta\, \mathrm{d}\rho &= \int_{\delta/R}^{h_0} 2\omega(h)\, \mathrm{d}h \int_{\delta/h}^{R} \mathrm{d}\rho \\ &= \int_{\delta/h_0}^{R} \mathrm{d}\rho \int_{\delta/\rho}^{h_0} 2\omega(h)\, \mathrm{d}h.\end{aligned} \tag{5.39}$$

We use the first form because the ρ integration is usually much easier and might be carried out analytically. Using the technique developed in the Appendix 5.6, we can evaluate the integration in A_δ to get the divergence structure (5.74).

5.3.4 Boundary contributions

The spacetime region we are interested in only has null codimension 1 boundary hypersurface, thus the YGH term is irrelevant. For the null hypersurfaces $\mathcal{E}^\pm$ and $\mathcal{W}^\pm$, we can choose the affine parameters and make it vanishes. The only term left would be the I_{joint}, which consists of three terms:

$$I_{\text{joint}} = I_W + 2I_J + I_E \tag{5.40}$$

where $I_J \equiv I_{J^+} = I_{J^-}$ due to symmetry. In terms of affine parameters, the null generators of the 4 hypersurfaces are

$$\begin{aligned} k_{W\pm,\mu} &= \alpha g^0_{\mu\nu} U^\nu; \\ k^{\lessgtr}_{E\pm,\mu} &= -\beta g^0_{\mu\nu} (V^{\lessgtr}_\pm)^\nu(\lambda), \end{aligned} \tag{5.41}$$

where α, β are positive normalization factors, and the signs are chosen so that these are outward pointing one forms. The integrands of these joint terms are

respectively

$$
\begin{aligned}
a_W &= -\log\left[\frac{1}{2}k_{W+,\mu}g^{0,\mu\nu}k_{W-,\nu})\right] = -\log\frac{\alpha^2\delta^2}{L^2} \\
a_J^{\lessgtr} &= \log\left[\frac{1}{2}k_{W\pm,\mu}g^{0,\mu\nu}k_{E\pm,\nu}^{\lessgtr}\right] = \log\frac{\alpha\beta(\rho+\rho h^2 \pm Kh\delta)^2}{2KH_\pm L^2} \\
a_E &= -\log\left[\frac{1}{2}k_{E+,\mu}g^{0,\mu\nu}k_{E-,\nu}\right] = -\log\frac{\beta^2\rho^2(1+h^2)^2}{K^2h^2L^2}
\end{aligned}
\tag{5.42}
$$

The joint contribution can then be expressed as

$$
I_{\text{joint}} = \frac{1}{8\pi G}\int_{A_\delta}\mathrm{d}\rho\,\mathrm{d}h\sum_{\jmath\in\{W,J^+,J^-,E\}}a_\jmath\sqrt{\det g_\jmath},
\tag{5.43}
$$

where $g_\jmath$ is given in Appendix 5.7, and the integration is carried out in Appendix 5.6.

5.4 Final Result and Discussions

Adding the contributions from bulk and boundary, the total action is obtained in (5.84), which I copied here:

$$
\begin{aligned}
I_{\text{total}}^{(\text{div})} &= \bar{v}_0\frac{V_A}{\delta^2} + \bar{b}_0(h_0)\frac{V_{\partial A}}{\delta} + k_1^0(h_0)\log\frac{R}{\delta} + k_2^0(h_0)\log^2\frac{R}{\delta} \\
&\quad + \log\frac{L}{\alpha\delta}\left[\bar{v}_0^\alpha\frac{V_A}{\delta^2} + \bar{b}_0^\alpha(h_0)\frac{V_{\partial A}}{\delta} + k_1^\alpha(h_0) + k_2^\alpha(h_0)\log\frac{R}{\delta}\right] \\
&\quad + \log\frac{L}{\beta\delta}\left[k_1^\beta(h_0) + k_2^\beta(h_0)\log\frac{R}{\delta}\right],
\end{aligned}
\tag{5.44}
$$

where the coefficient functions are defined in (5.85). We can see explicitly the volume law term that is proportional to the volume V_A, and the area law term that is proportional to the area $V_{\partial A} = 2R$, both defined in (5.86). In addition, there are divergences of order $\log\delta$ and order $\log^2\delta$.

5.4.1 Geometric Origin and Cutoff Dependence

In light of the discussions in [16], the divergence structure of the holographic complexity of subregion $\mathcal{A}$ can be expressed in terms of volume integration in $\mathcal{A}$ and surface integration on $\partial\mathcal{A}$

$$\mathcal{C}_{\mathcal{A}} = \int_{\mathcal{A}} v(\mathcal{R}, K; \xi) + \int_{\partial\mathcal{A}} b(\mathcal{R}, \tilde{K}; \mathbf{s}, \mathbf{t}; \xi), \tag{5.45}$$

In the above equation, we have $\mathcal{R}$ denoting the spacetime curvature, K denoting the exterior curvature of the time slice, $\tilde{K}$ denoting the exterior curvature of $\partial\mathcal{A}$, and $\mathbf{s}$, $\mathbf{t}$ denoting the spacelike and timelike normal vectors of the $\partial\mathcal{A}$. We added dependence of ξ denoting the collection of CFT parameters, which are dimensionless and should determine the coefficients of various combinations of curvatures in the integrands.

This expression is only for subregions with smooth surface, similar to gravitational action only with YGH term. In general, there could be higher codimension defects on the surface, like the cube example we mentioned in Sec. 5.3.2.3, and these defects could contribute independently to the complexity. Thus the most general form would be an expression similar to (5.30). In this paper, we only deal with a kink shape in two spatial dimensions, where the only singularity on the surface is the point-like kink tip. Thus the only extra term we expect is a local contribution that does not involve any integrations. For higher dimensional subregions with singular surface, integration might be needed for contributions from non-point-like creases.

The main point of this notation is that these integrands are local functions in $\mathcal{A}$ or on $\partial\mathcal{A}$. In our kink case, all curvatures involved in the volume and area integrations vanish: $\mathcal{R} = 0$ because we are in Poincare patch, $K = 0$ as we are on a trivial flat time slice, and $\tilde{K} = 0$ for the straight sides of the kink. Hence, we expect the integrands to be constants, and the integrations simply give the volume and surface area of $\mathcal{A}$. These are the volume law terms and area law terms shown above.

The locality of the integrands also imply that the coefficients of the volume and area terms are independent of the kink angle Ω or h_0. As expected, the volume law coefficients $\bar{v}_0 = -1/2$ and $\bar{v}_0^\alpha = 1$ are constants. However, we find that our area law coefficients depend on the openning angle, as seen from (5.85):

$$\bar{b}_0(h_0) = \frac{3 - 2\log 2}{2} + \Delta(h_0), \qquad \bar{b}_0^\alpha(h_0) = -1 - \Delta(h_0). \tag{5.46}$$

As a comparison, we can look at a smooth surface case, like a spherical region in Poincare patch [16]. For example, a disk region in CFT_3 has "CA" complexity

$$\begin{aligned}\mathcal{C}_A(\text{disk}) = \frac{L^2}{4\pi^2 G}\Bigg[&\left(-\frac{1}{2}\frac{\pi R^2}{\delta^2} + \frac{3 - 2\log 2}{2}\frac{2\pi R}{\delta} - 4\pi \log\frac{R}{\delta}\right) \\ &+ \log\frac{L}{\alpha\delta}\left(\frac{\pi R^2}{\delta} - \frac{2\pi R}{\delta} - \pi\right)\Bigg].\end{aligned} \tag{5.47}$$

The volume law coefficients are exactly the same, while the area law coefficients differ by a h_0 dependent shift $\Delta(h_0)$. This function has been plotted in Fig. 5.4,

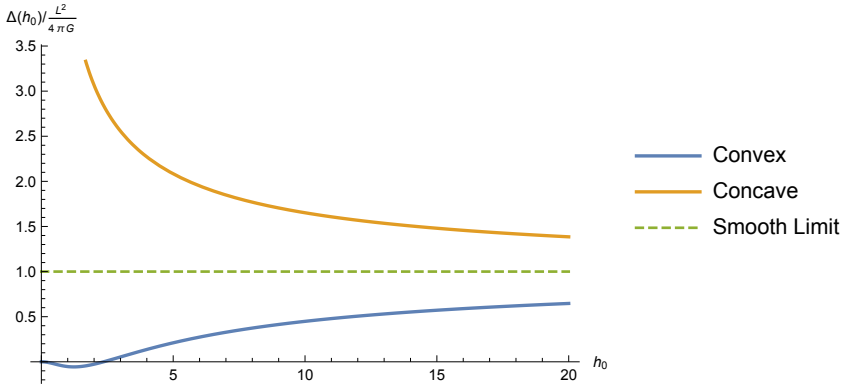

Figure 5.4: The $\Delta(h_0)$ shift function both for convex and concave kinks are presented. The function is zero for zero convex angle, and remains negative for a while as the angle increases. Afterwards, it increases monotonically towards infinity. When the openning angle crosses the flat angle, hence the smooth limit case, the function has value 1 (in unit of $L^2/4\pi G$).

from which it is clear that it vanishes for zero openning angle, and approaches 1 (in unit of $\frac{L^2}{4\pi G}$) in the $h_0 \to \infty$ smooth limit. It has a small dip into the negative values when the openning angle was very small, and then increase monotonically towards infinity as the openning angle continue increasing to the $\Omega \to \pi$ limit, which corresponds to moving to right infinity along the "convex" branch and coming back along the "concave" branch to $h_0 \to 0$. This weird area law contribution has the origin as the subleading term in the volume of W, as shown in (5.86). One can easily show that for ordinary constant IR cutoff on the boundary, no subleading term at this order would appear. Afterall, coefficients at this order are still cutoff dependent, so this extra contribution may not have important physical meaning.

It is also interesting to observe the sign difference between the volume

and area terms. If we assume that the terms with $\log \frac{L}{\alpha\delta}$ dominates (more details discussed in Sec. 5.4.3) over the terms without extra $\log \delta$, we end up with positive volume law term and negative area law term. The positive volume law is easy to understand as complexity naturally grow with the size of subregion. If we relate the area law terms with entanglement with outside of subregion, the negativity can also be understood as *loss* of detailed information of the entanglement when the outside is traced out. This loss of information also occurs for thermal state, when the complexity growth that is dual to the wormhole growth is completely hidden for the one-sided thermal state.

5.4.2 Cutoff Independent Terms

Next we investigate the cutoff independent coefficients, which naturally groups into the ones for log terms, denoted by k_1, and for $\log^2$ terms, denoted by k_2, which have superscripts $0, \alpha, \beta$ labelling the exact form of the logs.

We start by looking at the k_1 functions. These functions are shown in Fig. 5.5, where convex and concave cases are plotted separately. Note that besides the individual contributions, we also present the sum of them as the black curves. The sum represents the total coefficient of $\log \delta$ divergence if no extra δ dependence is introduced (for instance from the constants α, β, which will be discussed later).

One observation is that for convex openning angles, the sum is mostly contributed by $k_1^0(h_0)$ for large angles, while $k_1^{\alpha,\beta}(h_0)$ are nealy zero. $k_1^{\alpha,\beta}$ are much more important in small angle region. On the other hand, for concave

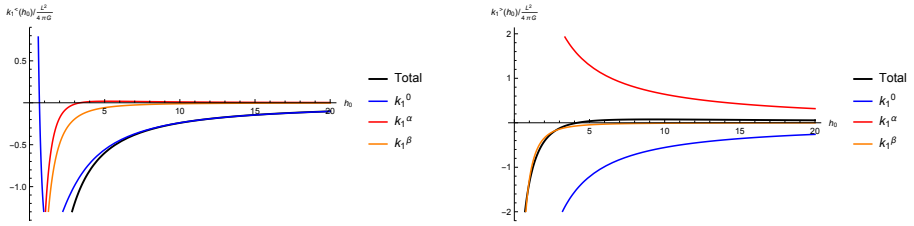

Figure 5.5: The coefficients for log divergence in the action is shown. The left panel is for convex kink and the right panel is for concave kink. Different contributions are labelled by different colors, while the sum is given by the black thick curves.

kinks, k_1^β remains small, while k_1^α and k_1^0 are roughly opposite of each other. In terms of additivity, the sum is mostly close to k_1^β as far as the plot shows.

Finally we look at the $\log^2$ terms $k_2(h_0)$. The first observation is the identity

$$k_2^\alpha + k_2^\beta = -2k_2^0. \tag{5.48}$$

This indicates a combination of the $\log^2$ level divergence structure

$$-2\log\frac{L}{\delta}\log\frac{R}{\delta} + \log^2\frac{R}{\delta} = -\log^2\frac{L}{\delta} + \log^2\frac{L}{R}, \tag{5.49}$$

where the second term is finite. It means that the way of writing it in three parts is only an artifact from the computational technique, while the true source of $\log^2$ term is only log term in the brackets at the second and third lines in (5.44). The contents in these two brackets have a more direct geometrical meaning. As shown in (5.42) and (5.43), $\log(L/\alpha\delta)$ and $\log(L/\beta\delta)$ are constant pieces in a_j which can be taken out of the integral, and the remains just give

the volumes of the joint surfaces. It turns out that we always have

$$I_{\text{total}} \supset \frac{1}{4\pi G}\left[\log\frac{L}{\alpha\delta}(V_W - V_J) + \log\frac{L}{\beta\delta}(V_E - V_J)\right]. \tag{5.50}$$

This indicates a relation with the generalized Bousso bound [126]. Note that from (5.20), the expansion rates on $\mathcal{E}$ vanishes on E, which makes all four null normal hypersurfaces bounded by E qualified as "light-sheets". In particular, $\mathcal{E}$ for both convex and concave kinks are light-sheets. On the other hand, the expansion rate on W of congruence towards the bulk is always negative, so $\mathcal{W}$ is also light-sheet.

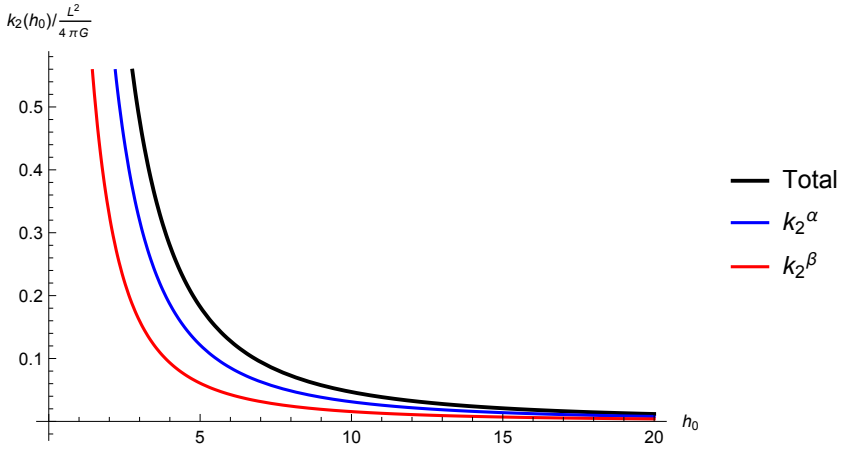

Figure 5.6: According to the relation (5.48), it is sufficient to only present the k_2^{α} and k_2^{β} functions. The sum of them is also presented as black curve. Note that the true total $\log^2$ coefficient should be half the sum.

The generalize Bousso bound states that the area differences of two sections on the light-sheets bound the entropy of matter on the part of light-sheets between the two sections. It is very powerful and was proven with weak

assumptions recently [127, 128]. In particular,

$$S(\mathcal{W}) \leq \frac{1}{4G}(V_W - V_J), \qquad S(\mathcal{E}) \leq \frac{1}{4G}(V_E - V_J). \tag{5.51}$$

The sum of the two then bounds the entropy inside the region $\mathcal{V}$, because $\mathcal{W} \cap \mathcal{E}$ is a Cauchy surface for $\mathcal{V}$[1].

It would be nice if the relation with Bousso bound could be valid for complexity of all shapes of subregions. Actually, the vanishing of expansion rates on the HRT surface is guaranteed by the extremailty condition of its area, thus $\mathcal{E}$ is always a light-sheet. However, there might be a problem that the light-sheet ends before it reaches the joint J, which does not happen in our case because the caustic occurs after the intersection at J, as discussed in Sec. 5.3.2.1. This though is not guaranteed in general cases. Therefore this relation with Bousso bound may be just an accident, or it is valid for a class of shapes with "good" property that caustic does not occur within the region $\mathcal{V}$.

Coming back to the $\log^2$ coefficients. The above arguments tend to imply that these $\log^2$ terms come from the log piece in the generalized Bousso bound. We have the coefficients plotted in Fig. 5.6. We further notice that

[1] A relation between entanglement entropy and the Bousso bound was first noticed in [129], where the Bousso bound considered was for the entropy on the whole $\mathcal{E}$, which is saturated due to the minimality of the Ryu-Takayanagi surface. Here $S(\mathcal{E})$ is saturated for the same reason, but $S(\mathcal{W})$ is far from saturation, and that's why it is very large due to the UV divergence of V_W. But both Bousso bound may fail because of caustic issues. In the case of kink, as is shown, there are caustics on $\mathcal{E}$, so the entanglement entropy is not a good bound for bulk entropy. But as the caustic is outside of $\mathcal{V}$, the bound we find here, though far from saturation, is a valid entropy bound for the region $\mathcal{V}$.

these coefficients do not depend on which of the convex and concave kinks is being computed, which means that it is purely determined by the entangling surface $\partial\mathcal{A}$ alone. This strongly suggests that this contribution originats from the entanglement entropy on the boundary.

As a summary, let us list the asymptotic behaviors of all the coefficient functions at various limits in Table. 5.1. The γ appearing in them is the one defined in (5.8). It is clear from the middle colume of the table that all of these

	$2\Omega \to 0$	$2\Omega \to \pi^{\pm}$	$2\Omega \to 2\pi$
k_1^0	$\dfrac{-1.22 - 3.59\log h_0}{h_0}$	$\dfrac{-\pi \pm \pi/2}{h_0}$	$-\dfrac{\pi}{h_0^2} + \dfrac{-2.70 - 3.59\log h_0}{h_0}$
k_1^α	$\dfrac{-1.68 + 2.40\log h_0}{h_0}$	$\dfrac{+\pi \mp \pi}{h_0}$	$\dfrac{\pi}{h_0^2} + \dfrac{2.42 + 2.40\log h_0}{h_0}$
k_1^β	$\dfrac{-2.51 + 1.20\log h_0}{h_0}$	0	$\dfrac{-1.03 + 1.20\log h_0}{h_0}$
k_2^α	$\dfrac{2\gamma + 2}{h_0}$	$\dfrac{\pi}{h_0^2}$	$\dfrac{2\gamma + 2}{h_0}$
k_2^β	$\dfrac{4\gamma - 2}{h_0}$	$\dfrac{\pi}{2h_0^2}$	$\dfrac{4\gamma - 2}{h_0}$

Table 5.1: Asymptotic Behaviors of various coefficient functions at small angle and smooth limits.

contributions seem to be from the kink feature of the subregion, because they all vanish at the smooth limit. To further verify this, one needs to compute a finite region with such kinks to see if these contributions appear as they are here. It will be a very interesting future work.

5.4.3 Determine α and β from Limiting Behavior

It was argued in [16] that the ambigous parameters α, β should be chosen as

$$\alpha = L/\ell_\alpha, \qquad \beta = L/\ell_\beta, \tag{5.52}$$

where $\ell_{\alpha,\beta}$ are some scales in the setup. The reason is that as a boundary quantity, the holographic complexity should denpend on L explicitly only through the combination L^2/G, thus L/α and L/β cannot have explicit L dependence. The natural ways to choose the scales $\ell_{\alpha,\beta}$ are left as only δ or R.

It was also pointed out that by setting $\ell_\alpha = R$, the typical size of the subregion, the complexity would be superextensive in the sense that it grows faster than the volume. We argue that the superextensivity is expected from long-range entanglement in the boundary theory. Naive extensivity holds if we only consider complexity of the UV structure of the state, but there can in general be long-range entanglement, whose complexity "density" accumulates logarithmically with the size, similar to the depth of MERA network for CFT states[2]. Therefore, we suggest that $\ell_\alpha = R$ is better interpretted than the choice $\ell_\alpha = e^\sigma \delta$ made in the paper [16].

We have further evidence that we should take $\ell_\alpha = R$. Note that by taking this value, we can combine k_1^0 and k_1^α by simple addition. From the

[2]One may still get extensivity by simply counting the number of gates in the MERA network as complexity. But we claim that gates in MERA at different scale level could in principle have different weights for complexity counting. To operate at larger scale will of course cost more "simple" operations based on a sense of locality for quantum gates.

Table. 5.1, it is easy to find that the $|\pi/2-\Omega|$ dependence at the smooth limit drops off. In terms of $\epsilon = \pi/2 - \Omega$ and using (5.7)[3], we can rewrite

$$\lim_{h_0\to\infty} k_1^0(h_0) = \frac{L^2}{4\pi G}(-2|\epsilon| - \epsilon), \qquad \lim_{h_0\to\infty} k_1^\alpha(h_0) = \frac{L^2}{4\pi G}(2|\epsilon| + 2\epsilon). \quad (5.53)$$

Hence simply adding them eliminates the $|\epsilon|$ dependence at least at leading order. It makes the complexity a differentiable function of angle Ω at the smooth limit. While the importance of this differentiability remains unclear, the "accidental" cancellation still suggests the privilege of taking $\ell_\alpha = R$.

As a side comment, we also like to point out that the cancellation of $|\epsilon|$ contributions leads to the following behavior

$$\mathcal{C}_A(\Omega) + \mathcal{C}_A(\pi - \Omega) \sim \epsilon^2. \quad (5.54)$$

Although in "CA" we don't have any identity like $\mathcal{C}_V(\mathcal{A}) + \mathcal{C}_V(\bar{\mathcal{A}}) = \mathcal{C}_V(\sigma)$[4] where σ is the whole space region, we still expect some physical meaning of

$$\mathcal{C}_E(\mathcal{A}:\mathcal{B}) \equiv \mathcal{C}_A(\mathcal{A}) + \mathcal{C}_A(\mathcal{B}) - \mathcal{C}_A(\mathcal{A}\cup\mathcal{B}) \quad (5.55)$$

which potentially describe the complexity of the entanglement between the two regions $\mathcal{A}$ and $\mathcal{B}$. It is then natural to assume that $\mathcal{C}_E \sim S_{\rm EE}(\mathcal{A})$ the

[3]Note that in (5.7), Ω is defined to be convex. For general Ω, we have $\Omega = \pi/2 \pm \frac{\pi}{2h_0}$ where $+$ sign is chosen for concave angle and $-$ for convex angle. Thus the term with $\pm$ sign is actually $\sim \epsilon$, while the term without $\pm$ is $\sim |\pi/2 - \Omega|$.

[4]This identity is proposed in [16] and only holds in time-symmetric bulk geometry when the HRT surface lies on the maximal time slice in the bulk. In more general cases, $\mathcal{C}_V(\mathcal{A}) + \mathcal{C}_V(\bar{\mathcal{A}}) < \mathcal{C}_V(\sigma)$ due to the maximality of bulk time slice volume on the right side.

entanglement entropy when $\mathcal{B} = \bar{\mathcal{A}}$[5]. We have already seen the area law contributions that may come from the entanglement entropy. Note that there is an extra log contribution in (5.9) to entanglement entropy of kink, which goes like ϵ^2 at the smooth limit according to (5.10). Thus the behavior in (5.54) can possibly be explained as the kink contribution to the entanglement entropy.

There is another "accident" in the Table. 5.1. If we simply add all the k_1 functions, at small angle behavior we have

$$\begin{aligned} \lim_{\Omega\to 0}(k_1^0(h_0)+k_1^\alpha(h_0)+k_1^\beta(h_0)) &= \frac{-5.4}{h_0}\frac{L^2}{4\pi G}, \\ \lim_{\Omega\to \pi}(k_1^0(h_0)+k_1^\alpha(h_0)+k_1^\beta(h_0)) &= \frac{-1.3}{h_0}\frac{L^2}{4\pi G}. \end{aligned} \tag{5.56}$$

Note that all the $\log(h_0)/h_0$ behavior exactly cancels[6]. It is also unclear whether this cancellation is important or not, but this "accident" suggests a simple addition of all the three terms, and hence the choice of $\ell_\beta = R$.

In sum, the complexity for the choice $\ell_\alpha = \ell_\beta = R$ is then

$$I^{(\text{div})}_{\text{total}} = \left(\bar{v}_0 + \bar{v}_0^\alpha \log\frac{R}{\delta}\right)\frac{V_A}{\delta^2} + \left(\bar{b}_0(h_0) + \bar{b}_0^\alpha \log\frac{R}{\delta}\right)\frac{V_{\partial A}}{\delta} + k_1(h_0)\log\frac{R}{\delta} + k_2(h_0)\log^2\frac{R}{\delta}. \tag{5.57}$$

where $k_1 = k_1^0 + k_1^\alpha + k_1^\beta$, $k_2 = k_2^0 + k_2^\alpha + k_2^\beta$. We can identify the constants

[5]For the general case $\mathcal{B} \neq \bar{\mathcal{A}}$, one may expect that $\mathcal{C}_E \sim I(\mathcal{A}:\mathcal{B})$ the mutual information, or other measure of entanglement between bipartite state like the entanglement of purification [130].

[6]The cancellation is examined analytically, thus it is not a numerical artifact.

appearing in the aymptotic behavior of $k_1(h_0)$ as "corner charges":

$$\begin{aligned}\lim_{\Omega\to 0} k_1(h_0) &= \frac{-5.4}{h_0}\frac{L^2}{4\pi G} = \frac{-9.04}{\Omega}\frac{L^2}{4\pi G} \equiv \frac{\kappa_{\mathcal{C}}}{\Omega},\\ \lim_{\Omega\to \pi} k_1(h_0) &= \frac{-1.3}{h_0}\frac{L^2}{4\pi G} = \frac{-2.19}{\Omega}\frac{L^2}{4\pi G} \equiv \frac{\kappa'_{\mathcal{C}}}{\Omega}.\end{aligned} \tag{5.58}$$

similar to the studies of entanglement entropy [119]. Note that there are two κ charges due to the lack of symmetry between $\mathcal{A}$ and $\bar{\mathcal{A}}$ in complexity. The corner charge for smooth limit is given by (5.53) as

$$\lim_{\Omega\to \pi/2} k_1(h_0) = \frac{L^2}{4\pi G}\epsilon \equiv \sigma_{\mathcal{C}}\epsilon, \tag{5.59}$$

where we chose the linear coefficient with respect to the deviation ϵ while in the entanglement entropy case it was the quadratic coefficient. There are no obvious relations between the corner charges for complexity due to lack of analyticity in the computation, and the universality for them to describe the underlying CFT is also unknown before more examples are investigated.

Finally, it was suggested in [87] that α should be interpretted as choice of reference state in the definition of field theory complexity. In light of this, we suggest that

$$\ell_\alpha = \ell_\beta = e^{\tilde{\sigma}\pi} R, \tag{5.60}$$

where the parameter $\tilde{\sigma}$ characterizes the change of the normalizations due to change of the reference states. This scale factor does not affect the analysis above. The only change is that, according to (5.51), besides the results we have in (5.57) we have additional term as

$$I_{\text{total}}(\tilde{\sigma}) = I_{\text{total}}(0) + \tilde{\sigma} S_B, \tag{5.61}$$

where S_B is the generalized Bousso bound on entropy within the causal diamond $\mathcal{V}$. This indicates that the complexity depends on reference state as linearly in $\tilde{\sigma}$ in unit of the Bousso entropy bound.

5.5 Conclusions

Inspired by the holographic entanglement entropy studies for boundary subregions with singular surface [118–120], and similar computations of complexity-volume for the same subregions [121], we studied the computation of complexity-action for the simplest subregion with singular surface, *i.e.* the 3D kink. After careful exploration of techniques used in the computation, we obtained the subregion complexity of 3D kink, which consists of volume law term, area law term, and cutoff independent divergent terms of order $\log \delta$ and $\log^2 \delta$.

Besides the computational techniques, there are also a few discussions of the property of the result that worths taking away. First, there are a few hints discovered for the contribution from entropy to the complexity. What is more, these hints are all absent in the approach of CV.

1. The appearance of area law terms and its negative sign. As explained in Sec. 5.4.1, the negative area law contribution can be attributed to the loss of information of entanglement. Although the general CV subregion complexity can have area law contribution, and it should be negative due to the inequality $\mathcal{C}_V(\mathcal{A}) + \mathcal{C}_V(\bar{\mathcal{A}}) \leq \mathcal{C}_V(\mathcal{A} \cup \bar{\mathcal{A}})$ (explained in footnote 4),

the fact that it may vanish in some case seems inconsistent with this interpretation.

2. The vanishment of $|\epsilon|$ dependence in the smooth limit. It both renders the differentiability of complexity across the flat angle, which is a plausible requirement, and also makes sure that $\mathcal{C}_V(\mathcal{A}) + \mathcal{C}_V(\bar{\mathcal{A}})$ behaves as ϵ^2, similar to the entanglement entropy. On the other hand, $k_2(h_0)$ is symmetric for convex and concave kinks, which reveals the fact that it only originates from the entangling surface. The log or $\log^2$ divergences may account for the kink contribution to the entanglement entropy, which is also at log level.

Second, there is also explicit relation between subregion complexity and the Bousso entropy bound, though the bound considered here seems far from saturated. One interesting relation is that the Bousso bound for $\mathcal{V}$ seems to set the rate of change of complexity with respect to the reference state labelled by $\tilde{\sigma}$ defined in (5.61).

Next, we made a comment on the superextensivity of subregion complexity, due to the extra leading log in the volume and area law terms. We claim that as the size of subregion grows, more and more long range entanglements, like more layers in MERA network, should be counted whose complexity density may be similar to the short range entanglement layers. The number of layers would be log of the size of the subregion, thus the overall leading contribution should go like $V \log V$ instead of V for simple extensivity. The

same argument goes for area law terms.

A striking side effect of the kink computation is that it gives hints about the determination of the normalization parameters α, β. Among the only choices R, δ in this setup, $\ell_{\alpha,\beta} \sim R$ are both favored according to the accidental cancellation of certain terms in the log coefficients when they are summed. The conclusion is (5.61), where extra freedom of scaling is allowed to account for the change of reference states.

5.6 Appendix I: Details of Action Computation

We adopt the following procedure to do ρ and θ integrations over the range defined by A_δ. Using eq(5.39), we obtain

$$F = \int_{A_\delta} \mathrm{d}\theta \, \mathrm{d}\rho \; f_0(\rho, h(\theta), \delta) = \int_{\delta/R}^{h_0} 2\omega(h) \, \mathrm{d}h \int_{\delta/h}^{R} \mathrm{d}\rho \; f_0(\rho, h, \delta). \tag{5.62}$$

The ρ integration is usually carried out analytically, so we can define

$$f_1(h, \delta) = 2\omega(h) \int_{\delta/h}^{R} \mathrm{d}\rho \; f_0(\rho, h, \delta). \tag{5.63}$$

Then we series expand $f_1(h, \delta)$ in powers of h, and extract the part that is divergent at $h = 0$

$$f_1(h, \delta) = f_{\mathrm{div}}(h, \delta) + f_2(h, \delta). \tag{5.64}$$

As f_{div} is in power series of h, its integration can be carried out explicitly

$$F_h(\delta) = \int_{\delta/R}^{h_0} f_{\mathrm{div}}(h, \delta), \tag{5.65}$$

while we do integration of $f_2(h, \delta)$ for each divergent powers of δ numerically. Namely, for the expansion

$$f_2(h, \delta) = \frac{f_2^{(2)}(h)}{\delta^2} + \frac{f_2^{(1)}(h)}{\delta^1} + f_2^{(0)}(h) \log \delta + \mathcal{O}(\delta^0), \tag{5.66}$$

we get

$$F^{(i)} = \int_0^{h_0} \mathrm{d}h \; f_2^{(i)}(h) - \sum_{j>i} \left[\int_0^{\delta/R} \mathrm{d}h \; f_2^{(j)}(h) \right] \Bigg|_{\mathcal{O}(\delta^{j-i})} \tag{5.67}$$

for ith order divergence. Note that although the regularity at $h = 0$ guarantees that there's no new divergence from integration at $h = 0$, it can still produce weakend divergence from the second term above. For instantce $\int_0^{\delta/R} \mathrm{d}h\ f_2^{(2)}(h)$ may contribute to $F^{(1)}$ if $f_2^{(2)}(0) \neq 0$. In sum, the UV divergent part of the integral F is

$$F_{\text{div}} = F_h(\delta) + \sum_i F^{(i)} \delta^{-i} \tag{5.68}$$

There is a subtlety in this procedure. Although $f_2(h, \delta)$ is regular at $h = 0$ by design, after expansion in δ, it may not be regular order by order. We are lucky that in our case the coefficients $f_2^{(i)}(h)$ are all integrable at $h = 0$.

Now we apply this procedure to the real calculations. In what follows, the functions $\omega(h)$, $H_\pm(h)$ and the integration constant K appear frequently in our calculations. They are defined in equations (5.6) , (5.26) and (5.5) respectively. For sake of completness we list them again here:

$$K = \frac{1 + h^2}{h^2 \sqrt{1 + h^2 + h'^2}} = \frac{\sqrt{1 + h_0^2}}{h_0^2} \tag{5.69}$$

$$\omega(h) = \frac{Kh^2}{\sqrt{(1 + h^2)(1 + h^2 - K^2 h^4)}} \tag{5.70}$$

$$H_\pm(h) \equiv 1 + h^2 \pm Kh^2 \tag{5.71}$$

5.6.1 Bulk contributions

First look at the bulk contribution eq(5.38):

$$\begin{aligned} f_0(\rho, h, \delta) = &-\frac{L^2}{8\pi G} \frac{(1 + h^2)^2 (\rho h - \delta)^2}{Kh^5 H_\pm \rho \delta^2 (\rho + \rho h^2 \pm Kh\delta)} \\ &\times \left[h(1 + h^2) H_\mp \rho^2 + 2(H_\pm^2 - 2K^2 h^4) \rho\delta \pm Kh(3H_+ + 2Kh^2)\delta^2 \right]. \end{aligned} \tag{5.72}$$

where the $\pm$ are for convex and concave kinks respectively. The ρ integration can be done analytically to get $f_1(h,\delta)$, which decomposes as

$$\begin{aligned}
f_1(h,\delta) &= f_{\text{div}}(h,\delta) + f_2(h,\delta), \\
f_{\text{div}}(h,\delta) &= \frac{L^2}{4\pi G}\left[\frac{2\delta}{Rh^3} + \frac{1}{h^2}\left(3\log\frac{Rh}{\delta} - \frac{3}{2} - \frac{K\delta^2}{2R^2}\right) + \frac{2K\delta}{Rh}\right], \\
f_2(h,\delta) &= \frac{L^2}{4\pi G}\left[\mathcal{B}_2(h)\frac{R^2}{\delta^2} + \mathcal{B}_1(h)\frac{R}{\delta} + \mathcal{B}_0(h)\log\left[\frac{R}{\delta}\right] + \mathcal{O}(\delta^0)\right].
\end{aligned} \tag{5.73}$$

Note that the non-zero limit of $\mathcal{B}_2$ at $h=0$ will contribute to the δ^{-1} divergence after integrated against the UV cutoff region, as indicated by the second term in eq(5.67). Overall, the UV divergences are:

$$\begin{aligned}
I^{(\text{div})}_{\text{bulk}} &= \int_{\delta/R}^{h_0} f_{\text{div}}(h,\delta) - \frac{L^2}{4\pi G}\int_0^{\delta/R} \mathrm{d}h\ \mathcal{B}_2(0)\frac{R^2}{\delta^2} \\
&\quad + \frac{L^2}{4\pi G}\int_0^{h_0} \mathrm{d}h\ \left[\mathcal{B}_2(h)\frac{R^2}{\delta^2} + \mathcal{B}_1(h)\frac{R}{\delta} + \mathcal{B}_0(h)\log\left[\frac{R}{\delta}\right]\right] + \mathcal{O}(\delta^0) \\
&= \frac{L^2}{4\pi G}\Bigg[\left(\int_0^{h_0}\mathrm{d}h\ \mathcal{B}_2(h)\right)\frac{R^2}{\delta^2} + \left(3 + \int_0^{h_0}\mathrm{d}h\ \mathcal{B}_1(h)\right)\frac{R}{\delta} \\
&\quad + \left(-\frac{3}{h_0} + \int_0^{h_0}\mathrm{d}h\ \mathcal{B}_0(h)\right)\log\left[\frac{R}{\delta}\right]\Bigg].
\end{aligned} \tag{5.74}$$

where the integrands for the numerical integrations are

$$\begin{aligned}
\mathcal{B}_2(h) &= -\frac{(1+h^2)H_{\mp}}{2Kh^2H_{\pm}}\omega(h), \\
\mathcal{B}_1(h) &= \mp\frac{4(1+h^2)}{hH_{\pm}}\omega(h), \\
\mathcal{B}_0(h) &= -\frac{3}{h^2}\left(1 - \frac{1+h^2}{Kh^2}\omega(h)\right) \pm \frac{3(1+h^2)^2 - K^2h^4}{h^2(1+h^2)H_{\pm}}\omega(h).
\end{aligned} \tag{5.75}$$

5.6.2 Joint contributions

Next look at the joint contribution eq(5.43). After the ρ integration, we have

$$\begin{aligned} f_1^W(h,\delta) &\equiv \frac{2\omega(h)}{8\pi G}\int_{\delta/h}^{R} \mathrm{d}\rho\ a_W\sqrt{\det g_W} \\ &= \frac{L^2}{4\pi G}\left[-\frac{1}{h^2}+\mathcal{J}_{20}(h)\frac{R^2}{\delta^2}+\mathcal{J}_{10}(h)\frac{R}{\delta}+\tilde{\mathcal{J}}_0^W(h)\right]\log\frac{L}{\alpha\delta}, \qquad (5.76) \\ f_1^J(h,\delta) &\equiv \frac{2\omega(h)}{8\pi G}\int_{\delta/h}^{R} \mathrm{d}\rho\ a_{J_\pm}\sqrt{\det g_{J_\pm}} \\ &= \frac{L^2}{8\pi G}\left[\frac{1}{2h^2}\left(\log^2\frac{R^2}{K\delta^2}-\log^2 Kh^2\right)+\mathcal{J}_{00}^J(h)\log^2\frac{R}{\delta}+\mathcal{J}_0^J\log\frac{R}{\delta}\right. \\ &\quad \left.+\left(-\frac{2}{h^2}\log\frac{Rh}{\delta}+\tilde{\mathcal{J}}_{00}^J(h)\log\frac{R}{\delta}+\tilde{\mathcal{J}}_0^J(h)\right)\log\frac{2L^2}{\alpha\beta\delta^2}\right], \qquad (5.77) \\ f_1^E(h,\delta) &\equiv \frac{2\omega(h)}{8\pi G}\int_{\delta/h}^{R} \mathrm{d}\rho\ a_E\sqrt{\det g_E} \\ &= \frac{L^2}{4\pi G}\left[\frac{1}{h^2}\left(\log^2 Kh^2-\log^2\frac{R}{Kh\delta}\right)+\mathcal{J}_{00}^E(h)\log^2\frac{R}{\delta}+\mathcal{J}_0^E\log\frac{R}{\delta}\right. \\ &\quad \left.+\left(\frac{2}{h^2}\log\frac{Rh}{\delta}+\tilde{\mathcal{J}}_{00}^E(h)\log\frac{R}{\delta}+\tilde{\mathcal{J}}_0^E(h)\right)\log\frac{L}{\beta\delta}\right]. \qquad (5.78) \end{aligned}$$

The result is thus

$$I_{\text{joint}}^{(\text{div})} = \int_{\delta/R}^{h_0}\mathrm{d}h\ (f_1^W+2f_1^J+f_1^E), \qquad (5.79)$$

where the $h = \delta/R$ contributions give

$$F_h^W - \int_0^{\delta/R} \mathrm{d}h\ \mathcal{J}_{20}(h)\frac{R^2}{\delta^2} = \frac{L^2}{4\pi G}\left(\frac{1}{h_0} - \frac{2R}{\delta}\right)\log\frac{L}{\alpha\delta}, \tag{5.80}$$

$$F_h^J = \frac{L^2}{8\pi G}\Bigg[\left(4\log\frac{R}{\delta} - 2\log K - 4\right)\frac{R}{\delta} + \frac{2\log K}{h_0}\log\frac{R}{\delta} - \frac{2}{h_0}\log^2\frac{R}{\delta} + \left(-\frac{2R}{\delta} + \frac{2}{h_0}\log\frac{R}{\delta} + \frac{2}{h_0}(1+\log h_0)\right)\log\frac{2L^2}{\alpha\beta\delta^2}\Bigg], \tag{5.81}$$

$$F_h^E = \frac{L^2}{4\pi G}\Bigg[\left(-4\log\frac{R}{\delta} + 2\log K + 6\right)\frac{R}{\delta} - \frac{2}{h_0}(1+\log Kh_0)\log\frac{R}{\delta} + \frac{1}{h_0}\log^2\frac{R}{\delta} + \left(\frac{2R}{\delta} - \frac{2}{h_0}\log\frac{R}{\delta} - \frac{2}{h_0}(1+\log h_0)\right)\log\frac{L}{\beta\delta}\Bigg]. \tag{5.82}$$

Note that the second lines in eq(5.81) and eq(5.82) are exactly opposite, indicating no dependence on β. Roughly speaking, these contributions are from ∂A. It is interesting to see that although the β dependence does not vanish in general, it might only come from the interior of the boundary region A. We

list the integrands of the numerical integrations as follows

$$
\begin{aligned}
\mathcal{J}_{20}(h) &= \frac{(1+h^2)H_{\mp}}{Kh^2H_{\pm}}\omega(h),\\
\mathcal{J}_{10}(h) &= \pm\frac{4(1+h^2)}{hH_{\pm}}\omega(h),\\
\tilde{\mathcal{J}}_0^W(h) &= \frac{1}{h^2}\left(1-\frac{1+h^2}{Kh^2}\omega(h)\mp\frac{2(1+h^2)}{H_{\pm}}\omega(h)\right),\\
\mathcal{J}_0^J(h) &= \frac{2}{h^2}\left(\log K+\frac{H_+H_-}{Kh^2(1+h^2)}\log\frac{(1+h^2)^2}{KH_{\pm}}\omega(h)\right),\\
\mathcal{J}_{00}^J(h) &= -\frac{2}{h^2}\left(1-\frac{H_+H_-}{Kh^2(1+h^2)}\omega(h)\right),\\
\tilde{\mathcal{J}}_0^J(h) &= \frac{2}{h^2}\left(\log h+\left(\frac{H_+H_-}{Kh^2(1+h^2)}\log\frac{H_{\pm}}{h(1+h^2)}-\frac{Kh^2}{1+h^2}\mp 1\right)\omega(h)\right),\\
\tilde{\mathcal{J}}_{00}^J(h) &= \frac{2}{h^2}\left(1-\frac{H_+H_-}{Kh^2(1+h^2)}\omega(h)\right),\\
\mathcal{J}_0^E(h) &= -\frac{2}{h^2}\left(\log(Kh)+\frac{1+h^2}{Kh^2}\log\frac{1+h^2}{Kh}\omega(h)\right),\\
\mathcal{J}_{00}^E(h) &= \frac{1}{h^2}\left(1-\frac{1+h^2}{Kh^2}\omega(h)\right),\\
\tilde{\mathcal{J}}_0^E(h) &= \frac{2}{h^2}\left(-\log h+\frac{1+h^2}{Kh^2}\log(h)\omega(h)\right),\\
\tilde{\mathcal{J}}_{00}^E(h) &= -\frac{2}{h^2}\left(1-\frac{1+h^2}{Kh^2}\omega(h)\right).
\end{aligned}
\tag{5.83}
$$

The naming rules are 1) $\mathcal{J}$ stands for joint contributions instead of bulk ones denoted by $\mathcal{B}$; 2) the subscripts denote the order of divergence, *i.e.* 2 for δ^{-2}, 1 for δ^{-1}, and each 0 for one $\log\delta$; 3) the superscripts show which joint surface source this term; 4) the tildes indicate that one of the log is of the form $\log(L/\delta)$ instead of $\log(R/\delta)$, which may or may not be important for future study.

5.6.3 Total Results

Now we can wrap up all the contributions and summarize as the following

$$\begin{aligned} I^{(\mathrm{div})}_{\mathrm{total}} &= \bar{v}_0 \frac{V_A}{\delta^2} + \bar{b}_0(h_0)\frac{V_{\partial A}}{\delta} + k^0_1(h_0)\log\frac{R}{\delta} + k^0_2(h_0)\log^2\frac{R}{\delta} \\ &\quad + \log\frac{L}{\alpha\delta}\left[\bar{v}^\alpha_0\frac{V_A}{\delta^2} + \bar{b}^\alpha_0(h_0)\frac{V_{\partial A}}{\delta} + k^\alpha_1(h_0) + k^\alpha_2(h_0)\log\frac{R}{\delta}\right] \\ &\quad + \log\frac{L}{\beta\delta}\left[k^\beta_1(h_0) + k^\beta_2(h_0)\log\frac{R}{\delta}\right], \end{aligned} \tag{5.84}$$

where the coefficients are

$$\begin{aligned} &\bar{v}_0 = \frac{L^2}{4\pi G}\left(-\frac{1}{2}\right), \qquad \bar{b}_0(h_0) = \frac{L^2}{4\pi G}\left[\frac{3-2\log 2}{2} + \Delta(h_0)\right], \\ &k^0_1(h_0) = \frac{L^2}{4\pi G}\Bigg[-\frac{1}{h_0}(5 - 2\log 2 + 2\log h_0) \\ &\quad + \int_0^{h_0} \mathrm{d}h\ \left(\mathcal{B}_0(h) + \mathcal{J}^E_0(h) + \mathcal{J}^J_0(h) + \log 2\ \tilde{\mathcal{J}}^J_{00}(h)\right)\Bigg], \\ &k^0_2(h_0) = \frac{L^2}{4\pi G}\left[-\frac{1}{h_0} + \int_0^{h_0}\mathrm{d}h\ \left(\mathcal{J}^E_{00}(h) + \mathcal{J}^J_{00}(h)\right)\right], \\ &\bar{v}^\alpha_0 = \frac{L^2}{4\pi G}, \qquad \bar{b}^\alpha_0(h_0) = \frac{L^2}{4\pi G}\left[-1 - \Delta(h_0)\right], \\ &k^\alpha_1(h_0) = \frac{L^2}{4\pi G}\left[\frac{1}{h_0}(3 + 2\log h_0) + \int_0^{h_0}\mathrm{d}h\ \left(\tilde{\mathcal{J}}^W_0(h) + \tilde{\mathcal{J}}^J_0(h)\right)\right], \\ &k^\alpha_2(h_0) = \frac{L^2}{4\pi G}\left[\frac{2}{h_0} + \int_0^{h_0}\mathrm{d}h\ \tilde{\mathcal{J}}^J_{00}(h)\right], \\ &k^\beta_1(h_0) = \frac{L^2}{4\pi G}\int_0^{h_0}\mathrm{d}h\ \left(\tilde{\mathcal{J}}^E_0(h) + \tilde{\mathcal{J}}^J_0(h)\right), \\ &k^\beta_2(h_0) = \frac{L^2}{4\pi G}\int_0^{h_0}\mathrm{d}h\ \left(\tilde{\mathcal{J}}^E_{00}(h) + \tilde{\mathcal{J}}^J_{00}(h)\right). \end{aligned} \tag{5.85}$$

The volume V_A is defined to be the leading order in the volume of W which should be equal to the volume of $\mathcal{A}$ with appropriate IR cutoff, with induced

metric on joint W at the cutoff surface (c.f. Appendix 5.7), which can be read off in (5.76) and (5.80) as

$$\begin{aligned}
&\int_W \sqrt{\det g_W} = \frac{L^2}{\delta^2}\left(V_A - \delta\Delta(h_0)V_{\partial A} + \mathcal{O}(\delta^2)\right), \\
&V_A = R^2\int_0^{h_0} \mathrm{d}h\ \mathcal{J}_{20}(h), \qquad V_{\partial A} = 2R, \\
&\Delta(h_0) = 1 - \frac{1}{2}\int_0^{h_0} \mathrm{d}h\ \mathcal{J}_{10}(h).
\end{aligned} \tag{5.86}$$

5.7 Appendix II: Induced Geometry on the Null Hypersurfaces

In this appendix, some detailed calculations about the null hypersurface geometry will be carried out. These results are involved in several discussions like Sec(5.3.2) and the joint contribution computations.

Because we are always using $w^\alpha = (\rho, \theta)$ defined on the HRT surface as the parameters, the light sheet geometry is mostly convenient to be studied as induced geometry following the flow of $V^\mu_\pm$ and $U^\mu_\pm$. Starting from the HRT surface, from eq(5.15) we get the induced metric on $\mathcal{E}^\pm$:

$$\begin{aligned} g^\pm_{\alpha\beta}(\lambda) &= \frac{\partial X^\pm_\mu(\lambda)}{\partial w^\alpha}\frac{\partial X^\pm_\nu(\lambda)}{\partial w^\beta} g^0_{\mu\nu}, \\ \sqrt{\det g^\pm(\lambda)} &= \frac{(1+h^2)(\lambda_c^2-\lambda^2)\rho}{Kh^2L^2}. \end{aligned} \tag{5.87}$$

As λ is chosen to be affine parameter, the expansion rate of the congruence $V^\mu_\pm$ can be computed

$$\Theta_\pm = \frac{1}{\sqrt{\det g^\pm(\lambda)}}\frac{\partial}{\partial\lambda}\sqrt{\det g^\pm(\lambda)} = -\frac{2\lambda}{\lambda_c^2-\lambda^2}. \tag{5.88}$$

As expected, the monotonicity is predicted by focusing theorem, and it blows up to negative infinity at the caustic.

Next we investigate the hypersurfaces $\mathcal{W}^\pm$. With eq(5.24), we write down the induced metric

$$\begin{aligned} \tilde{g}^\pm_{\alpha\beta}(\eta) &= \frac{\partial \tilde{X}^\pm_\mu(\eta)}{\partial w^\alpha}\frac{\partial \tilde{X}^\pm_\nu(\eta)}{\partial w^\beta} g^0_{\mu\nu}, \\ \sqrt{\det \tilde{g}(\eta(\tilde{\lambda}))} &= \frac{(1+h^2)(H_\pm L^2 + \tilde{\lambda}h(\rho+\rho h^2 \pm Kh\delta))^2(\rho H_\mp \pm 2Kh\delta)}{Kh^4 H_\pm L^2(\rho+\rho h^2 \pm Kh\delta)^2}. \end{aligned} \tag{5.89}$$

Here we reparameterize with affine parameter $\tilde{\lambda}$ for future convenience

$$\eta^{\lessgtr}(\tilde{\lambda}) = \frac{\tilde{\lambda}h^2(\rho(1+h^2) \pm Kh\delta)^2}{H_\pm[H_\pm L^2 + \tilde{\lambda}h(\rho(1+h^2) \pm Kh\delta)]}. \tag{5.90}$$

and we drop the $\pm$ superscript due to time reflection symmetry. We also restore the $>$ and $<$ superscripts for concave and convex kinks respectively. We recognize the induced metric on the joint surfaces as g and $\tilde{g}$ at different ends of the affine parameter ranges, and obtain the relations:

$$\begin{aligned}
&\sqrt{\det g(0)} \equiv \sqrt{\det g_E} = \frac{(1+h^2)}{Kh^4\rho}L^2, \\
&\sqrt{\det g^{\lessgtr}(\lambda_*)} = \sqrt{\det \tilde{g}^{\lessgtr}(0)} \equiv \sqrt{\det g_J^{\lessgtr}} = \frac{(1+h^2)H_\pm(\rho H_\mp \pm 2Kh\delta)}{Kh^4(\rho(1+h^2) \pm Kh\delta)^2}L^2, \\
&\sqrt{\det \tilde{g}^{\lessgtr}(\eta_*)} \equiv \sqrt{\det g_W^{\lessgtr}} = \frac{(1+h^2)(\rho H_\mp \pm 2Kh\delta)}{Kh^2H_\pm\delta^2}L^2.
\end{aligned} \tag{5.91}$$

Bibliography

[1] Ming-Lei Xiao and Jiang-Hao Yu. Stabilizing electroweak vacuum in a vectorlike fermion model. *Phys. Rev.*, D90(1):014007, 2014. [Addendum: Phys. Rev.D90,no.1,019901(2014)].

[2] Ming-Lei Xiao and Jiang-Hao Yu. Electroweak baryogenesis in a scalar-assisted vectorlike fermion model. *Phys. Rev.*, D94(1):015011, 2016.

[3] Aditya Aravind, Minglei Xiao, and Jiang-Hao Yu. Higgs Portal to Inflation and Fermionic Dark Matter. *Phys. Rev.*, D93(12):123513, 2016. [Erratum: Phys. Rev.D96,no.6,069901(2017)].

[4] Giuseppe Degrassi, Stefano Di Vita, Joan Elias-Miro, Jose R. Espinosa, Gian F. Giudice, Gino Isidori, and Alessandro Strumia. Higgs mass and vacuum stability in the Standard Model at NNLO. *JHEP*, 08:098, 2012.

[5] Dario Buttazzo, Giuseppe Degrassi, Pier Paolo Giardino, Gian F. Giudice, Filippo Sala, Alberto Salvio, and Alessandro Strumia. Investigating the near-criticality of the Higgs boson. *JHEP*, 12:089, 2013.

[6] Oleg Lebedev. On Stability of the Electroweak Vacuum and the Higgs Portal. *Eur. Phys. J.*, C72:2058, 2012.

[7] Joan Elias-Miro, Jose R. Espinosa, Gian F. Giudice, Hyun Min Lee,

and Alessandro Strumia. Stabilization of the Electroweak Vacuum by a Scalar Threshold Effect. *JHEP*, 06:031, 2012.

[8] Jacob D. Bekenstein. Black holes and entropy. *Phys. Rev.*, D7:2333–2346, 1973.

[9] S. W. Hawking. Black Holes and Thermodynamics. *Phys. Rev.*, D13:191–197, 1976.

[10] Gerard 't Hooft. Dimensional reduction in quantum gravity. *Conf. Proc.*, C930308:284–296, 1993.

[11] Juan Martin Maldacena. The Large N limit of superconformal field theories and supergravity. *Int. J. Theor. Phys.*, 38:1113–1133, 1999. [Adv. Theor. Math. Phys.2,231(1998)].

[12] Juan Maldacena and Leonard Susskind. Cool horizons for entangled black holes. *Fortsch. Phys.*, 61:781–811, 2013.

[13] Leonard Susskind. Computational Complexity and Black Hole Horizons. *Fortsch. Phys.*, 64:44–48, 2016. [Fortsch. Phys.64,24(2016)].

[14] Douglas Stanford and Leonard Susskind. Complexity and Shock Wave Geometries. *Phys. Rev.*, D90(12):126007, 2014.

[15] Josiah Couch, Stefan Eccles, Willy Fischler, and Ming-Lei Xiao. Holographic complexity and non-commutative gauge theory. *JHEP*, 18:108, 2018.

[16] Dean Carmi, Robert C. Myers, and Pratik Rath. Comments on Holographic Complexity. *JHEP*, 03:118, 2017.

[17] J. Beringer et al. Review of Particle Physics (RPP). *Phys. Rev.*, D86:010001, 2012.

[18] Abdelhak Djouadi and Alexander Lenz. Sealing the fate of a fourth generation of fermions. *Phys. Lett.*, B715:310–314, 2012.

[19] Otto Eberhardt, Geoffrey Herbert, Heiko Lacker, Alexander Lenz, Andreas Menzel, Ulrich Nierste, and Martin Wiebusch. Impact of a Higgs boson at a mass of 126 GeV on the standard model with three and four fermion generations. *Phys. Rev. Lett.*, 109:241802, 2012.

[20] S. Dawson and E. Furlan. A Higgs Conundrum with Vector Fermions. *Phys. Rev.*, D86:015021, 2012.

[21] Handbook of vectorlike quarks: Mixing and single production. *Phys. Rev.*, D88(9):094010, 2013.

[22] Giacomo Cacciapaglia, Aldo Deandrea, Daisuke Harada, and Yasuhiro Okada. Bounds and Decays of New Heavy Vector-like Top Partners. *JHEP*, 11:159, 2010.

[23] Giacomo Cacciapaglia, Aldo Deandrea, Luca Panizzi, Naveen Gaur, Daisuke Harada, and Yasuhiro Okada. Heavy Vector-like Top Partners at the LHC and flavour constraints. *JHEP*, 03:070, 2012.

[24] Sidney R. Coleman and Erick J. Weinberg. Radiative Corrections as the Origin of Spontaneous Symmetry Breaking. *Phys. Rev.*, D7:1888–1910, 1973.

[25] A. Sirlin and R. Zucchini. Dependence of the Quartic Coupling H(m) on M(H) and the Possible Onset of New Physics in the Higgs Sector of the Standard Model. *Nucl. Phys.*, B266:389–409, 1986.

[26] Ralf Hempfling and Bernd A. Kniehl. On the relation between the fermion pole mass and MS Yukawa coupling in the standard model. *Phys. Rev.*, D51:1386–1394, 1995.

[27] Benjamin W. Lee, C. Quigg, and H. B. Thacker. Weak Interactions at Very High-Energies: The Role of the Higgs Boson Mass. *Phys. Rev.*, D16:1519, 1977.

[28] Michael S. Chanowitz and Mary K. Gaillard. The TeV Physics of Strongly Interacting W's and Z's. *Nucl. Phys.*, B261:379–431, 1985.

[29] Duane A. Dicus and Hong-Jian He. Scales of fermion mass generation and electroweak symmetry breaking. *Phys. Rev.*, D71:093009, 2005.

[30] John M. Cornwall, David N. Levin, and George Tiktopoulos. Derivation of Gauge Invariance from High-Energy Unitarity Bounds on the s Matrix. *Phys. Rev.*, D10:1145, 1974. [Erratum: Phys. Rev.D11,972(1975)].

[31] York-Peng Yao and C. P. Yuan. Modification of the Equivalence Theorem Due to Loop Corrections. *Phys. Rev.*, D38:2237, 1988.

[32] Jonathan Bagger and Carl Schmidt. Equivalence Theorem Redux. *Phys. Rev.*, D41:264, 1990.

[33] Hong-Jian He, Yu-Ping Kuang, and Xiao-yuan Li. On the precise formulation of equivalence theorem. *Phys. Rev. Lett.*, 69:2619–2622, 1992.

[34] Giovanni Marco Pruna and Tania Robens. Higgs singlet extension parameter space in the light of the LHC discovery. *Phys. Rev.*, D88(11):115012, 2013.

[35] Michael E. Peskin and Tatsu Takeuchi. Estimation of oblique electroweak corrections. *Phys. Rev.*, D46:381–409, 1992.

[36] M. Baak, M. Goebel, J. Haller, A. Hoecker, D. Kennedy, R. Kogler, K. Moenig, M. Schott, and J. Stelzer. The Electroweak Fit of the Standard Model after the Discovery of a New Boson at the LHC. *Eur. Phys. J.*, C72:2205, 2012.

[37] Riccardo Barbieri, Matteo Beccaria, Paolo Ciafaloni, Giuseppe Curci, and Andrea Vicere. Two loop heavy top effects in the Standard Model. *Nucl. Phys.*, B409:105–127, 1993.

[38] J. Fleischer, O. V. Tarasov, and F. Jegerlehner. Two loop large top mass corrections to electroweak parameters: Analytic results valid for arbitrary Higgs mass. *Phys. Rev.*, D51:3820–3837, 1995.

[39] Tomohiro Abe, R. Sekhar Chivukula, Neil D. Christensen, Ken Hsieh, Shinya Matsuzaki, Elizabeth H. Simmons, and Masaharu Tanabashi.

Z —¿ b anti-b and Chiral Currents in Higgsless Models. *Phys. Rev.*, D79:075016, 2009.

[40] Roshan Foadi, Carl R. Schmidt, and Jiang-Hao Yu. Constraints on Little Higgs with Fully-Radiative Electroweak Symmetry Breaking. *Phys. Rev.*, D85:055015, 2012.

[41] G. Passarino and M. J. G. Veltman. One Loop Corrections for e+ e- Annihilation Into mu+ mu- in the Weinberg Model. *Nucl. Phys.*, B160:151–207, 1979.

[42] Marco Ciuchini, Enrico Franco, Satoshi Mishima, and Luca Silvestrini. Electroweak Precision Observables, New Physics and the Nature of a 126 GeV Higgs Boson. *JHEP*, 08:106, 2013.

[43] Serguei Chatrchyan et al. Inclusive search for a vector-like T quark with charge $\frac{2}{3}$ in pp collisions at $\sqrt{s} = 8$ TeV. *Phys. Lett.*, B729:149–171, 2014.

[44] Serguei Chatrchyan et al. Search for a standard-model-like Higgs boson with a mass in the range 145 to 1000 GeV at the LHC. *Eur. Phys. J.*, C73:2469, 2013.

[45] P. A. R. Ade et al. Planck 2015 results. XIII. Cosmological parameters. *Astron. Astrophys.*, 594:A13, 2016.

[46] A. D. Sakharov. Violation of CP Invariance, C asymmetry, and baryon asymmetry of the universe. *Pisma Zh. Eksp. Teor. Fiz.*, 5:32–35, 1967. [Usp. Fiz. Nauk161,no.5,61(1991)].

[47] V. A. Kuzmin, V. A. Rubakov, and M. E. Shaposhnikov. On the Anomalous Electroweak Baryon Number Nonconservation in the Early Universe. *Phys. Lett.*, 155B:36, 1985.

[48] M. E. Shaposhnikov. Possible Appearance of the Baryon Asymmetry of the Universe in an Electroweak Theory. *JETP Lett.*, 44:465–468, 1986. [Pisma Zh. Eksp. Teor. Fiz.44,364(1986)].

[49] M. E. Shaposhnikov. Baryon Asymmetry of the Universe in Standard Electroweak Theory. *Nucl. Phys.*, B287:757–775, 1987.

[50] Andrew G. Cohen, D. B. Kaplan, and A. E. Nelson. Progress in electroweak baryogenesis. *Ann. Rev. Nucl. Part. Sci.*, 43:27–70, 1993.

[51] Mark Trodden. Electroweak baryogenesis. *Rev. Mod. Phys.*, 71:1463–1500, 1999.

[52] Mariano Quiros. Finite temperature field theory and phase transitions. In *Proceedings, Summer School in High-energy physics and cosmology: Trieste, Italy, June 29-July 17, 1998*, pages 187–259, 1999.

[53] Werner Bernreuther. CP violation and baryogenesis. *Lect. Notes Phys.*, 591:237–293, 2002. [,237(2002)].

[54] James M. Cline. Baryogenesis. In *Les Houches Summer School - Session 86: Particle Physics and Cosmology: The Fabric of Spacetime Les Houches, France, July 31-August 25, 2006*, 2006.

[55] David E. Morrissey and Michael J. Ramsey-Musolf. Electroweak baryogenesis. *New J. Phys.*, 14:125003, 2012.

[56] A. I. Bochkarev, S. V. Kuzmin, and M. E. Shaposhnikov. On the Model Dependence of the Cosmological Upper Bound on the Higgs Boson and Top Quark Masses. *Phys. Rev.*, D43:369–374, 1991.

[57] A. I. Bochkarev and M. E. Shaposhnikov. Electroweak Production of Baryon Asymmetry and Upper Bounds on the Higgs and Top Masses. *Mod. Phys. Lett.*, A2:417, 1987.

[58] Jarny Choi and R. R. Volkas. Real Higgs singlet and the electroweak phase transition in the Standard Model. *Phys. Lett.*, B317:385–391, 1993.

[59] James M. Cline and Pierre-Anthony Lemieux. Electroweak phase transition in two Higgs doublet models. *Phys. Rev.*, D55:3873–3881, 1997.

[60] S. W. Ham, Y. S. Jeong, and S. K. Oh. Electroweak phase transition in an extension of the standard model with a real Higgs singlet. *J. Phys.*, G31(8):857–871, 2005.

[61] Amine Ahriche. What is the criterion for a strong first order electroweak phase transition in singlet models? *Phys. Rev.*, D75:083522, 2007.

[62] Stefano Profumo, Michael J. Ramsey-Musolf, and Gabe Shaughnessy. Singlet Higgs phenomenology and the electroweak phase transition. *JHEP*, 08:010, 2007.

[63] Jose R. Espinosa, Thomas Konstandin, and Francesco Riva. Strong Electroweak Phase Transitions in the Standard Model with a Singlet. *Nucl. Phys.*, B854:592–630, 2012.

[64] Tai Li and Yu-Feng Zhou. Strongly first order phase transition in the singlet fermionic dark matter model after LUX. *JHEP*, 07:006, 2014.

[65] Kaori Fuyuto and Eibun Senaha. Improved sphaleron decoupling condition and the Higgs coupling constants in the real singlet-extended standard model. *Phys. Rev.*, D90(1):015015, 2014.

[66] Stefano Profumo, Michael J. Ramsey-Musolf, Carroll L. Wainwright, and Peter Winslow. Singlet-catalyzed electroweak phase transitions and precision Higgs boson studies. *Phys. Rev.*, D91(3):035018, 2015.

[67] C. Jarlskog. Commutator of the Quark Mass Matrices in the Standard Electroweak Model and a Measure of Maximal CP Violation. *Phys. Rev. Lett.*, 55:1039, 1985.

[68] J. Bernabeu, G. C. Branco, and M. Gronau. CP RESTRICTIONS ON QUARK MASS MATRICES. *Phys. Lett.*, 169B:243–247, 1986.

[69] F. del Aguila, J. A. Aguilar-Saavedra, and G. C. Branco. CP violation from new quarks in the chiral limit. *Nucl. Phys.*, B510:39–60, 1998.

[70] F. J. Botella, G. C. Branco, and M. Nebot. The Hunt for New Physics in the Flavour Sector with up vector-like quarks. *JHEP*, 12:040, 2012.

[71] Ashutosh Kumar Alok, Subhashish Banerjee, Dinesh Kumar, S. Uma Sankar, and David London. New-physics signals of a model with a vector-singlet up-type quark. *Phys. Rev.*, D92:013002, 2015.

[72] Greg W. Anderson and Lawrence J. Hall. The Electroweak phase transition and baryogenesis. *Phys. Rev.*, D45:2685–2698, 1992.

[73] Cedric Delaunay, Christophe Grojean, and James D. Wells. Dynamics of Non-renormalizable Electroweak Symmetry Breaking. *JHEP*, 04:029, 2008.

[74] Rajesh R. Parwani. Resummation in a hot scalar field theory. *Phys. Rev.*, D45:4695, 1992. [Erratum: Phys. Rev.D48,5965(1993)].

[75] Peter Brockway Arnold and Olivier Espinosa. The Effective potential and first order phase transitions: Beyond leading-order. *Phys. Rev.*, D47:3546, 1993. [Erratum: Phys. Rev.D50,6662(1994)].

[76] Angel Sanchez, Alejandro Ayala, and Gabriella Piccinelli. Effective potential at finite temperature in a constant hypermagnetic field: Ring diagrams in the standard model. *Phys. Rev.*, D75:043004, 2007.

[77] Jonathan Kozaczuk. Bubble Expansion and the Viability of Singlet-Driven Electroweak Baryogenesis. *JHEP*, 10:135, 2015.

[78] F. James and M. Roos. Minuit: A System for Function Minimization and Analysis of the Parameter Errors and Correlations. *Comput. Phys. Commun.*, 10:343–367, 1975.

[79] Leonard Susskind and Ying Zhao. Switchbacks and the Bridge to Nowhere. 2014.

[80] Adam R. Brown, Daniel A. Roberts, Leonard Susskind, Brian Swingle, and Ying Zhao. Holographic Complexity Equals Bulk Action? *Phys. Rev. Lett.*, 116(19):191301, 2016.

[81] Adam R. Brown, Daniel A. Roberts, Leonard Susskind, Brian Swingle, and Ying Zhao. Complexity, action, and black holes. *Phys. Rev.*, D93(8):086006, 2016.

[82] Josiah Couch, Willy Fischler, and Phuc H. Nguyen. Noether charge, black hole volume, and complexity. *JHEP*, 03:119, 2017.

[83] Koji Hashimoto, Norihiro Iizuka, and Sotaro Sugishita. Time Evolution of Complexity in Abelian Gauge Theories - And Playing Quantum Othello Game -. 2017.

[84] Robert A. Jefferson and Robert C. Myers. Circuit complexity in quantum field theory. 2017.

[85] Pawel Caputa, Nilay Kundu, Masamichi Miyaji, Tadashi Takayanagi, and Kento Watanabe. Liouville Action as Path-Integral Complexity: From Continuous Tensor Networks to AdS/CFT. 2017.

[86] Bartlomiej Czech. Einstein's Equations from Varying Complexity. 2017.

[87] Shira Chapman, Michal P. Heller, Hugo Marrochio, and Fernando Pastawski. Towards Complexity for Quantum Field Theory States. *Phys. Rev. Lett.*, 120:121602, 2018.

[88] Run-Qiu Yang. A Complexity for Quantum Field Theory States and Application in Thermofield Double States. 2017.

[89] S. Lloyd. Ultimate physical limits to computation. *Nature*, 406:1047, 2000.

[90] Norman Margolus and Lev B. Levitin. The Maximum speed of dynamical evolution. *Physica*, D120:188–195, 1998.

[91] Dean Carmi, Shira Chapman, Hugo Marrochio, Robert C. Myers, and Sotaro Sugishita. On the Time Dependence of Holographic Complexity. 2017.

[92] William Cottrell and Miguel Montero. Complexity is Simple. 2017.

[93] Nathan Seiberg and Edward Witten. String theory and noncommutative geometry. *JHEP*, 09:032, 1999.

[94] Juan Martin Maldacena and Jorge G. Russo. Large N limit of noncommutative gauge theories. *JHEP*, 09:025, 1999.

[95] Akikazu Hashimoto and N. Itzhaki. Noncommutative Yang-Mills and the AdS / CFT correspondence. *Phys. Lett.*, B465:142–147, 1999.

[96] Rong-Gen Cai and Nobuyoshi Ohta. On the thermodynamics of large N noncommutative superYang-Mills theory. *Phys. Rev.*, D61:124012, 2000.

[97] Mohsen Alishahiha, Yaron Oz, and M. M. Sheikh-Jabbari. Supergravity and large N noncommutative field theories. *JHEP*, 11:007, 1999.

[98] David S. Berman, Vanicson L. Campos, Martin Cederwall, Ulf Gran, Henric Larsson, Mikkel Nielsen, Bengt E. W. Nilsson, and Per Sundell. Holographic noncommutativity. *JHEP*, 05:002, 2001.

[99] Mohammad Edalati, Willy Fischler, Juan F. Pedraza, and Walter Tangarife Garcia. Fast Scramblers and Non-commutative Gauge Theories. *JHEP*, 07:043, 2012.

[100] Willy Fischler, Arnab Kundu, and Sandipan Kundu. Holographic Entanglement in a Noncommutative Gauge Theory. *JHEP*, 01:137, 2014.

[101] Joanna L. Karczmarek and Charles Rabideau. Holographic entanglement entropy in nonlocal theories. *JHEP*, 10:078, 2013.

[102] W. Fischler, E. Gorbatov, A. Kashani-Poor, R. McNees, S. Paban, and P. Pouliot. The Interplay between theta and T. *JHEP*, 06:032, 2000.

[103] Luis Lehner, Robert C. Myers, Eric Poisson, and Rafael D. Sorkin. Gravitational action with null boundaries. *Phys. Rev.*, D94(8):084046, 2016.

[104] Adam R. Brown and Leonard Susskind. The Second Law of Quantum Complexity. 2017.

[105] Adam R. Brown, Leonard Susskind, and Ying Zhao. Quantum Complexity and Negative Curvature. *Phys. Rev.*, D95(4):045010, 2017.

[106] Mohsen Alishahiha, Harald Ita, and Yaron Oz. Graviton scattering on D6-branes with B fields. *JHEP*, 06:002, 2000.

[107] T. Araujo, I. Bakhmatov, E. Ó Colgáin, J. Sakamoto, M. M. Sheikh-Jabbari, and K. Yoshida. Yang-Baxter σ-models, conformal twists, and noncommutative Yang-Mills theory. *Phys. Rev.*, D95(10):105006, 2017.

[108] Thiago Araujo, Ilya Bakhmatov, Eoin Ó Colgáin, Jun-ichi Sakamoto, Mohammad M. Sheikh-Jabbari, and Kentaroh Yoshida. Conformal Twists, Yang-Baxter σ-models & Holographic Noncommutativity. 2017.

[109] I. Bakhmatov, Ö. Kelekci, E. Ó Colgáin, and M. M. Sheikh-Jabbari. Classical Yang-Baxter Equation from Supergravity. 2017.

[110] Leonard Susskind. Butterflies on the Stretched Horizon. 2013.

[111] Leonard Susskind. Entanglement is not enough. *Fortsch. Phys.*, 64:49–71, 2016.

[112] Mohsen Alishahiha. Holographic Complexity. *Phys. Rev.*, D92(12):126009, 2015.

[113] Omer Ben-Ami and Dean Carmi. On Volumes of Subregions in Holography and Complexity. *JHEP*, 11:129, 2016.

[114] H. Casini and M. Huerta. Universal terms for the entanglement entropy in 2+1 dimensions. *Nucl. Phys.*, B764:183–201, 2007.

[115] H. Casini, M. Huerta, and L. Leitao. Entanglement entropy for a Dirac fermion in three dimensions: Vertex contribution. *Nucl. Phys.*, B814:594–609, 2009.

[116] Pablo Bueno, Robert C. Myers, and William Witczak-Krempa. Universal corner entanglement from twist operators. *JHEP*, 09:091, 2015.

[117] Robert C. Myers and Ajay Singh. Entanglement Entropy for Singular Surfaces. *JHEP*, 09:013, 2012.

[118] Pablo Bueno, Robert C. Myers, and William Witczak-Krempa. Universality of corner entanglement in conformal field theories. *Phys. Rev. Lett.*, 115:021602, 2015.

[119] Pablo Bueno and Robert C. Myers. Corner contributions to holographic entanglement entropy. *JHEP*, 08:068, 2015.

[120] Pablo Bueno and Robert C. Myers. Universal entanglement for higher dimensional cones. *JHEP*, 12:168, 2015.

[121] Elaheh Bakhshaei, Ali Mollabashi, and Ahmad Shirzad. Holographic Subregion Complexity for Singular Surfaces. 2017.

[122] Sergei N. Solodukhin. The Conical singularity and quantum corrections to entropy of black hole. *Phys. Rev.*, D51:609–617, 1995.

[123] Veronika E. Hubeny, Mukund Rangamani, and Tadashi Takayanagi. A Covariant holographic entanglement entropy proposal. *JHEP*, 07:062, 2007.

[124] Krishnamohan Parattu, Sumanta Chakraborty, Bibhas Ranjan Majhi, and T. Padmanabhan. A Boundary Term for the Gravitational Action with Null Boundaries. *Gen. Rel. Grav.*, 48(7):94, 2016.

[125] Shira Chapman, Hugo Marrochio, and Robert C. Myers. Complexity of Formation in Holography. *JHEP*, 01:062, 2017.

[126] Eanna E. Flanagan, Donald Marolf, and Robert M. Wald. Proof of classical versions of the Bousso entropy bound and of the generalized second law. *Phys. Rev.*, D62:084035, 2000.

[127] Raphael Bousso, Horacio Casini, Zachary Fisher, and Juan Maldacena. Proof of a Quantum Bousso Bound. *Phys. Rev.*, D90(4):044002, 2014.

[128] Raphael Bousso, Horacio Casini, Zachary Fisher, and Juan Maldacena. Entropy on a null surface for interacting quantum field theories and the Bousso bound. *Phys. Rev.*, D91(8):084030, 2015.

[129] Tomoyoshi Hirata and Tadashi Takayanagi. AdS/CFT and strong subadditivity of entanglement entropy. *JHEP*, 02:042, 2007.

[130] Tadashi Takayanagi and Koji Umemoto. Holographic Entanglement of Purification. 2017.